

# UC Santa Barbara

## UC Santa Barbara Electronic Theses and Dissertations

### Title

Ferromagnetism and Superconductivity in Rhombohedral Trilayer Graphene

### Permalink

<https://escholarship.org/uc/item/4k36g8qk>

### Author

Zhou, Haoxin

### Publication Date

2021

Peer reviewed|Thesis/dissertation



University of California  
Santa Barbara

# **Ferromagnetism and Superconductivity in Rhombohedral Trilayer Graphene**

A dissertation submitted in partial satisfaction  
of the requirements for the degree

Doctor of Philosophy  
in  
Physics

by

Haoxin Zhou

Committee in charge:

Professor Andrea Young, Chair  
Professor Mark Sherwin  
Professor Chetan Nayak

September 2021

The Dissertation of Haoxin Zhou is approved.

---

Professor Mark Sherwin

---

Professor Chetan Nayak

---

Professor Andrea Young, Committee Chair

July 2021

Ferromagnetism and Superconductivity in Rhombohedral Trilayer Graphene

Copyright © 2021

by

Haixin Zhou

To my parents

## Acknowledgements

My PhD study could have been a terrible experience, but I was lucky enough to meet the right people.

First and foremost I would like to thank my advisor Andrea Young, a talented, energetic and patient mentor, who can answer questions as broad as where physics will go in the next ten years or as detailed as which button to press first.

I would like to thank Sasha Zibrov and François Parmentier, who guided me in the early days when I did not even know graphene is made by tapes. I did a lot of experiments since then but every one of them starts with the steps you showed me with patience.

I owe a lot to Ben Xie, who I worked together on the trilayer graphene experiments. I could not imagine how any of these experiments could work without your hard work day and night, even on a Christmas Eve. I would also like to thank James Ehrets and Eric Spanton for their efforts on this project when they were in UCSB.

I am lucky to work in a lab where I can get help and learn from every one. I really enjoy sharing laughs and watching the lab growing with Marec Serlin and Charlie Tschirhart. Thank Liam Cohen for setting up the state-of-the-art dilution fridge that I relied on for a large portion of the experiments. I would like to thank Alex Ports for your detailed instructions of cleanroom tools. I learned a lot from Gregory Polshyn, Fangyuan Yang and Yu Saito on both fabrication and measurement techniques. And I still remember Joshua Island told me I should save old samples because you would never know what you will learn from them. And yes, what happened later proved you are right.

It was upset when no experiments were working, and I did not know why, but luckily I have friends I can enjoy the life with and temporarily forget what was happening in the lab. I would especially like to thank Zhurun Ji. Sharing each other's research life and traveling across this continent has been an important part of my life.

Finally, I would like to thank my parents for their unconditional support no matter what I choose to do.

# Curriculum Vitæ

## Haoxin Zhou

### Education

- 2021 Ph.D. in Physics (Expected), University of California, Santa Barbara.
- 2018 M.A. in Physics, University of California, Santa Barbara.
- 2015 B.S. in Phsics, University of Science and Technology of China

### Publications

H. Zhou, T. Xie, T. Taniguchi, K. Watanabe, A. F. Young. “Superconductivity in rhombohedral trilayer graphene.” arXiv:2106.07640 (2021)

H. Zhou, T. Xie, A. Ghazaryan, T. Holder, J. Ehrets, E. M. Spanton, T. Taniguchi, K. Watanabe, E. Berg, M. Serbyn, A. F. Young. “Half and quarter metals in rhombohedral trilayer graphene.” arXiv:2104.00653 (2021)

H. Zhou, C. Huang, N. Wei, T. Taniguchi, K. Watanabe, M. P. Zaletel, Z. Papić, A. H. MacDonald, A. F. Young. “Strong-Magnetic-Field Magnon Transport in Monolayer Graphene” arXiv:2102.01061 (2021)

A. Jenkins, S. Baumann, H. Zhou, S. A. Meynell, D. Yang, K. Watanabe, T. Taniguchi, A. Lucas, A. F. Young, A. C. Bleszynski Jayich, “Imaging the breakdown of ohmic transport in graphene.” arXiv:2002.05065 (2020)

H. Zhou, H. Polshyn, T. Taniguchi, K. Watanabe, A. F. Young. “Solids of quantum Hall skyrmions in graphene.” *Nature Physics* **16** 154-158 (2020).

J.O. Island, X. Cui, C. Lewandowski, J.Y. Khoo, E. M. Spanton, H. Zhou, D. Rhodes, J.C. Hone, T. Taniguchi, K. Watanabe, L.S. Levitov, M.P. Zaletel, A.F. Young. “Spin-orbit driven band inversion in bilayer graphene by van der Waals proximity effect.” *Nature* **571**, 85–89 (2019).

H. Polshyn, H. Zhou, E. M. Spanton, T. Taniguchi, K. Watanabe, and A. F. Young. “Quantitative transport measurements of fractional quantum Hall energy gaps in edgeless graphene devices.” *Physical Review Letters* **121**, 226801 (2018).

A. A. Zibrov, E.M. Spanton, H. Zhou, C. Kometter, T. Taniguchi, K. Watanabe, A.F. Young "Even denominator fractional quantum Hall states at an isospin transition in monolayer graphene." *Nature Physics* **14**, 930-935 (2018).

E. M. Spanton, A. A. Zibrov, H. Zhou, T. Taniguchi, K. Watanabe, M. P. Zaletel, A. F. Young. "Observation of fractional Chern insulators in a van der Waals heterostructure." *Science* **360**, 62–66 (2018).

A. A. Zibrov, C. R. Kometter, H. Zhou, E. M. Spanton, T. Taniguchi, K. Watanabe, M. P. Zaletel, and A. F. Young. "Tunable interacting composite fermion phases in a half-filled bilayer-graphene Landau level." *Nature* **549**, 360–364 (2017).



## Abstract

Ferromagnetism and Superconductivity in Rhombohedral Trilayer Graphene

by

Haoxin Zhou

This work studies the Van Hove singularity induced novel electronic phenomena in rhombohedral trilayer graphene, including magnetism and superconductivity. Rhombohedral trilayer graphene is a two dimensional crystal where three layers of carbon honeycomb lattice are stacked to form a rhombohedral lattice in its three dimensional extension. The energy band structure of rhombohedral trilayer graphene features van Hove singularities, saddle points in the energy band structure where the density of states diverges. A perpendicular electrical field can be applied to induce an interlayer potential and to open up an energy gap at the charge neutrality point. The gap opening modulates the density of states profile, making the divergence at the van Hove singularity robust against fluctuations from finite temperature and disorder effects. Like many other systems, the diverged density of states induces Fermi surface instability. On the one hand, it drives spontaneous ferromagnetic polarization of the electron system into one or more spin- and valley flavors. On the other hand, it allows the bounded states where electrons couple into pairs to have significant lower energy than the normal ground states, leading to superconductivity observable at the experimentally reached temperature. In this work, we fabricated dual graphite-gated rhombohedral trilayer graphene van der Waals heterostructures that allow cryogenic electrical transport measurement and penetration field capacitance measurements. On these samples we systematically studied the gate voltage modulated magnetic phase transitions and superconductivity. A rigid band model is built that well captures the spin- and valley- phase transitions. For super-

conductivity, we mainly focus on the phenomenology but also provide several possible explanations. In addition to gate voltages, we can also induce a moiré potential to the system by aligning the lattice of the rhombohedral trilayer graphene with the dielectric material hexagonal boron nitride. We found that while the moiré potential only affects the electronic phase diagram on a perturbative level, several novel phenomena including the breaking of lattice symmetry is induced.

# Contents

<b>Curriculum Vitae</b>	<b>vii</b>
<b>Abstract</b>	<b>ix</b>
<b>List of Figures</b>	<b>xiii</b>
<b>1 Introduction</b>	<b>1</b>
1.1 High Density of States Physics . . . . .	1
1.2 High density of states in two-dimensional electron systems . . . . .	3
1.3 Rhombohedral trilayer graphene . . . . .	5
1.4 Outline of the rest chapters . . . . .	9
<b>2 Theoretical Background</b>	<b>10</b>
2.1 Overview . . . . .	10
2.2 Continuum Model . . . . .	10
2.2.1 Monolayer Graphene . . . . .	10
2.2.2 Continuum Model of Rhombohedral Trilayer Graphene . . . . .	15
2.2.3 Carrier Density, Density of States and Van Hove Singularity . . . . .	18
2.3 Rigid-band Model of Interaction . . . . .	21
<b>3 Experimental Techniques</b>	<b>25</b>
3.1 Overview . . . . .	25
3.2 Sample Fabrication . . . . .	26
3.2.1 Preparation of the Trilayer Graphene Flakes . . . . .	26
3.2.2 Preparation of the Van der Waals Heterostructures . . . . .	32
3.2.3 Fabrication of the Dual-gated Transistor . . . . .	38
3.3 Electrical Measurement . . . . .	40
3.3.1 Transport Measurement . . . . .	42
3.3.2 Penetration Field Capacitance Measurement . . . . .	44

<b>4 Stoner Ferromagnetism</b>	<b>49</b>
4.1 Overview . . . . .	49
4.2 Inverse compressibility at zero displacement field . . . . .	50
4.3 Displacement field-tuned Magnetic Phase Transition . . . . .	53
4.4 Stoner Ferromagnetism . . . . .	58
4.5 Ferromagnetism and Fermi surface topology in the valence band . . . . .	62
4.6 Phase transition in the 1x phase at hole doping . . . . .	66
4.7 Hartree-Fock model . . . . .	70
<b>5 Superconductivity</b>	<b>76</b>
5.1 Overview . . . . .	76
5.2 Superconducting phenomenology in RTG . . . . .	77
5.3 Discussion . . . . .	88
<b>6 Effects of a Moiré Potential</b>	<b>92</b>
6.1 Overview . . . . .	92
6.2 Effects of the Moiré Potential . . . . .	93
6.3 Symmetry Breaking Insulating States . . . . .	96
6.4 Charge Density Waves at fractionally filled Moiré Bands . . . . .	98
6.5 Incompressible States under Magnetic Field . . . . .	98
<b>7 Summary and Outlook</b>	<b>101</b>
<b>A Procedure of Sample Fabrication</b>	<b>106</b>
<b>Bibliography</b>	<b>112</b>

# List of Figures

2.1	Crystal structure of monolayer graphene. . . . .	12
2.2	Band structure of monolayer graphehe. . . . .	14
2.3	Lattice structure of the rhombohedral trilayer graphene. . . . .	15
2.4	Band structure of rhombohedral trilayer graphene . . . . .	17
2.5	Density of states calculated from the six-band continuum model . . . . .	20
3.1	Procedure of device fabrication . . . . .	26
3.2	Optical micrograph of exfoliated graphene flakes . . . . .	27
3.3	Raman spectrum of graphene . . . . .	28
3.4	Mapping the stacking orders . . . . .	29
3.5	Schematics of AFM cutting based on anodic oxidation . . . . .	30
3.6	Isolating the ABC domains by AFM cutting . . . . .	32
3.7	Cross-section of the dual-graphite gated RTG heterostructure. . . . .	34
3.8	PPC film pickup side. Scale bar represents 1 cm. . . . .	34
3.9	Procedure of Van der Waals heterostructure fabrication . . . . .	35
3.10	PPC pickup slide assembly comparison . . . . .	37
3.11	Alignment between the heterostructure and the pickup slide. . . . .	38
3.12	Procedure to Measure the Raman spectrum of encapsulated RTG . . . . .	39
3.13	Transport measurement configuration . . . . .	43
3.14	Capacitance bridge circuit . . . . .	45
4.1	Inverse compressibility measured at $D = 0$ . . . . .	50
4.2	Shubnikov de Haas oscillation at $D = 0$ . . . . .	52
4.3	Band structure and density of states of rhombohedral trilayer graphene . . . . .	53
4.4	False-color plot of the inverse compressibility . . . . .	54
4.5	Inverse compressibility as a function of displacement field and carrier density . . . . .	55
4.6	Inverse compressibility calculated from the six-band continuum model . . . . .	55
4.7	Inverse compressibility at electron doping . . . . .	56
4.8	Fourier transform of SdH oscillations at electron doping . . . . .	58
4.9	Stoner magnetism . . . . .	59
4.10	Stoner magnetism with anisotropic interaction . . . . .	60

4.11	Order of symmetry breaking . . . . .	62
4.12	Inverse compressibility at hole doping . . . . .	63
4.13	SdH oscillation at hole doping. . . . .	64
4.14	Hysteretic transport . . . . .	65
4.15	In-plane magnetic field dependence of the phase boundaries . . . . .	66
4.16	$\alpha$ - and $\beta$ - phase . . . . .	67
4.17	Magnetic field dependent phase boundary . . . . .	68
4.18	Hall effect in the 1x phase at hole doping . . . . .	69
4.19	Free energy calculated from the Hartree-Fock model . . . . .	73
5.1	Resistivity vs density and displacement field . . . . .	78
5.2	Temperature dependence of the nonlinear resistivity . . . . .	79
5.3	Displacement field dependence of SC1. . . . .	80
5.4	Temperature dependence of SC1, SC2, and SC3. . . . .	81
5.5	SdH oscillation and Fermiology near SC1 . . . . .	82
5.6	$B_{\perp}$ -dependence of SC1 . . . . .	83
5.7	Magnetic focusing experiment . . . . .	84
5.8	In-plane magnetic field response of SC1 . . . . .	85
5.9	Fermiology near SC2 . . . . .	85
5.10	Nonlinear transport near SC2. . . . .	86
5.11	Temperature and magnetic field dependence near SC2. . . . .	87
5.12	Large range temperature near SC1 . . . . .	88
5.13	$B_{\parallel}$ -dependence near SC1 . . . . .	89
6.1	Formation of Moiré superlattice. . . . .	93
6.2	Effect of a moiré superlattice potential. . . . .	94
6.3	Origin of the symmetry breaking insulating states. . . . .	95
6.4	Magnetic field response of the insulating states . . . . .	97
6.5	Incompressible states at fractional fillings. . . . .	98
6.6	Magnetic field induced phase transitions at commensurate fillings. . . . .	99
7.1	Schematic of gate screening . . . . .	103

# Chapter 1

## Introduction

### 1.1 High Density of States Physics

In general, electrons in crystal is an extremely complicated system. Since even the collision of two electrons can already generate phenomena that is yet fully understood, it is almost impossible to imaging a system with  $10^{23}$  electrons mixed with similar numbers of nuclei. However, if we limit our scope to the "normal" condition on the surface of this planet. the electrons actually behave in a quite organized and predictable way.

Because of the orders of magnitude difference between the electron and iron mass. The kinetic energy of ions can be ignored when describing motions of electrons. (The Born-Oppenheimer approximation). In addition, the electron-electron interaction can usually be treated together with the lattice potential in a mean-field approach. With these approximations, the crystal is treated as independent electrons moving in a periodic potential. Bloch's theorem states that the wavefunction of the electrons has the following properties

$$\psi(\mathbf{r} + \mathbf{R}) = e^{i\mathbf{k}\cdot\mathbf{R}}\psi(\mathbf{r}). \quad (1.1)$$

Based on the Bloch's Theorem, the energy band theory is built and can explain the majority of electronic properties such as electrical conductivity, heat capacity, Hall effect etc. In this picture, the Fermi-Dirac distribution, originated from the Pauli exclusion principle, together with the energy band dispersion determines the ground states of the electrons. The Coulomb interactions between electrons still exists, but the corresponding energy scale is not large enough to alter the ground states of electrons in most cases.

The situation can be different when the energy of the electrons are not sensitive to the lattice momentum, or  $\nabla_{\mathbf{k}}E$  is small, this usually means the density of states (DOS)

$$D(E) \equiv \frac{dn}{dE} = \int dS \frac{1}{|\nabla_{\mathbf{k}}E|} \quad (1.2)$$

is large.

Such a system can host numerous electrons with nearly identical kinetic energy, the Coulomb interactions will play an important role in determining the ground state. The Stoner criterion states that when the product of the strength of electron-electron interactions and the DOS at the Fermi surface is greater than one[1],

$$UD_{\text{F}}(E) > 1 \quad (1.3)$$

The electrons will have their spins spontaneously broken, inducing ferromagnetism. This theory explains the ferromagnetism in transition metals like nickel, iron and cobalt. In these metals the partially filled narrow d-band contributes a high density of states at the Fermi surface[2].

Although electron-electron correlation is already complicated and interesting, a high density of states can induce other effects. In the Bardeen-Cooper-Schrieffer (BCS) theory



of superconductivity, the superconducting gap can be expressed as [3]

$$T_c = T_F e^{-\frac{1}{gD_F}} \quad (1.4)$$

Here  $g$ ,  $T_F$  are phenomenological parameters. The gap equation predicts that large density at the Fermi surface helps increase the critical temperature for superconductivity phase transition. When  $T_c$  is above the value the instrument can reach, the sample will become a superconductor.

In many cases, the electron pairs are spin singlet and the spontaneous spin polarization breaks the channel of superconductivity. In this case, the Stoner magnetism and BCS superconductivity compete with each other. The phase diagram will be determined by the details of the electron systems.

## 1.2 High density of states in two-dimensional electron systems

Novel phenomena such as electron magnetism has been observed in a variety of two-dimensional electronic systems[4, 5, 6, 7, 8]. Two-dimensional electronic system is a material where carrier electrons are trapped within a two-dimensional space, either two-dimensional materials like graphene[9] or by creating an inversion layer at a heterostructure[10]. A big advantage of two-dimensional electronic system is its tunability. By applying a gate voltage, the carrier density, and therefore the Fermi energy can be modulated. By fabricate two-dimensional materials into heterostructures, we can effectively create new materials with completely different band structure. These techniques allow us to engineer the electronic properties to induce high density of states physics.

Two approaches can be applied to induce high density of states at the Fermi surface.

One way is to have a narrow band dispersion relation, like the d-band in ferromagnetic metals. This can be easily achieved by applying a strong magnetic field that is perpendicular to the sample plane to induce quantum Hall effect[11]. In this case, the energy band of the system is reconstructed into Landau levels, whose energy is completely independent of momentum, when the Fermi surface is tuned so that one of the Landau level is partially filled, the density of states is infinite without considering finite temperature and disorder effects. This technique has been applied to many two dimensional systems including both heterostructures and two-dimensional materials[11, 12] and interaction driven phenomena are observed, including quantum Hall ferromagnetism[13, 14] and fractional quantum Hall effect[15, 16]. Superconductivity is not expected in quantum Hall systems as the magnetic field required to induce quantum Hall effect is usually far beyond the critical magnetic field of superconductivity. Nevertheless, the quantum Hall system is still an rich system that is far from full understood and had broad potential application such as topological computing.[17]

Apart from applying a strong magnetic field, for 2D materials, there is a new technique developed in the recent years that can generate flat dispersion relations at zero magnetic field, which is to align two two-dimensional lattices with identical or similar lattice structure to generate a Moiré pattern.[18, 19, 20] When two layers of graphene are aligned with a small angle of around  $1.1^\circ$ , the band structure of the system is reconstructed, leading to an isolated band near the charger neutrality point with nearly flat dispersion relation.[20] Experiments ([21, 22] has shown that when a gate voltage is applied to have electrons fill one half, one quarter, or three quarters of the allowed states, the electrons spontaneously break the spin- and valley- degeneracy to favor the exchange interaction. This will open additional energy gaps and drive the system into an insulating state. The mechanism is very similar to the origin of quantum Hall ferromagnetism, but since no magnetic field is needed and the time reversal symmetry is

protected, it allows superconducting phases. They are indeed observed when a light doping is applied to the correlation induced insulating states. The observation has drawn a lot of attention since the phase diagram of the graphene moiré superlattice is highly similar to high-temperature superconductors. While the observed critical temperature (around 1K) is far below the standard of "high temperature" superconductor, the gate tunability of the carrier density allows multiple phases in the same sample just by varying the gate voltage, unlike the high-temperature superconductor whose carrier density is usually determined when the material is synthesized. In addition, graphene, even when twisted, is still a cleaner and simpler electronic systems compared to cuprates, which is formed with multiple elements and disorder is unavoidable during the synthesization process. This allows systematic study of the electron pairing mechanism and may help to understand the not yet cleared mechanism of unconventional superconductivity.

While flat band dispersion guarantees high density of states, the latter occurs not necessarily with a flat band in present. In Eq. 1.1, the integrand diverge at an extremum of the dispersion relation. These extremal points are called Van Hove Singularities.[2] For three dimensional crystal, the divergence of the intergrand will be compensated by the integral and generate an unsmoothed point in the density of profile. In two dimensional system, however, when the extrema of the dispersion relation is a saddle point, the density of states profile will inherit the divergence. In this case, when the Fermi surface is tuned near the Van Hove Singularity, a large  $D_F$  is obtained. This approach to induce high DOS is the start point of this work.

### 1.3 Rhombohedral trilayer graphene

Rhombohedral trilayer graphene is a two dimensional electron system where three layers of graphene stacked to form a rhombohedral lattice. Trilayer graphene actually

have another more stable phase, bernal-stacked trilayer graphene (or ABA-stacked trilayer graphene). The difference of stacking order gives very different electronic properties. The band structure of ABA-trilayer graphene is roughly an overlap of monolayer graphene and bilayer graphene, with weak coupling between the two layers, while the ABC-stacked trilayer graphene is a chiral generalization of monolayer graphene, with its band structure significantly different from that of monolayer and bilayer graphene[23].

Way before the discovery of graphene, the rhombohedral stacking order was observed in natural graphite by a series of X-ray diffraction experiments.[24, 25, 26, 27]. After that, the energy band structure and other electronic properties of rhombohedral graphite was systematically studied theoretically.[28, 29].

Since the isolation of graphite monolayers[9], the research focus has been switched to graphite thin films and graphite surface states. Koshino et al[30] and Zhang et al[23] built a six-band continuum model that well captures the low energy band structure of the rhombohedral trilayer graphene. They found that the interlayer hopping significantly alters the band structure in the low energy regime, inducing three pockets (usually called the "trigonal warping" effect) where the conduction and valance band touches. The trigonal warping effect is crucial in determining the electronic property of rhombohedral trilayer graphene because it induces Van Hove singularities between the energy band pockets where the density of states diverges. Their work also predicted that an electric field applied perpendicular to the rhombohedral trilayer graphene will open up an energy gap, convert the system from a semimetal to a semiconductor. The opening of the energy gap also flats the band bottom and therefore enhance the van Hove singularities, making the divergence feature of DOS robust against temperature and disorder effects.

As mentioned in the previous section, a system with high density of states often host novel phenomena originated from electron-electron correlation and other effects beyond the band theory. Otani et al[31] studied the 0001 surface of rhombohedral graphite with

first principle calculation and predicted spontaneous spin polarization. Similar investigation was also performed by Pamuk et al[32], in which they studied the possible magnetic phase and charge density waves induced by exchange interaction. Zhang et al[33] and Xu et al[34] predicted that the flat band bottom of rhombohedral graphite multilayer system can host gapless surface states originated from electron-electron interactions. The surface states is also comprehensively studied with density functional theory by Xiao et al in 2011[35]. This surface states have the potential to host a competing order of magnetism and high temperature superconductivity.[36, 37, 38, 39, 40].

Despite the interest, experimental study of the system requires isolation of rhombohedral trilayer graphene, which is challenging because the rhombohedral order usually coexist with bernal stacking order in mechanical exfoliated flakes and the domains cannot be distinguished by optical microscopy. Several techniques have been developed to identify the stacking order. The first one is spatial map of Raman spectrum [41, 42, 43, 44], which is the techniques we used in this work. The advantage of Raman spectroscopy is it does not require the surface to be exposed, so the spectrum can be taken even when the trilayer graphene is encapsulated in other materials, which turns out to be convenient for sample fabrication. Besides, no mechanical manipulation is applied during the measurement which may relax the metal stable rhombohedral order. Since the Raman spectroscopy is a far-field measurement, the spatial resolution is limited by the wavelength of the laser. The near field Raman spectroscopy[45] may help to increase the spatial resolution. In fact, a similar technique, the near-field infrared microscopy turns out to have the ability to determine the stacking order of trilayer graphene[46]. Benefited from the near-field measurement, a higher resolution is obtained compared to the Raman spectroscopy. Since the measurement is performed with an atomic force microscope, in situ probe manipulation of the sample is possible. Apart from optical probes, it is reported by Asylum Research that scanning probe kelvin force microscopy can also be used

to distinguish the stacking order of trilayer graphene.[47]. This technique gives similar spatial resolution without the need of a complicated optical setup.

An alternative route to obtain rhombohedral trilayer/multilayer graphene is to directly synthesize the film with rhombohedral stacking order instead of search in mechanically exfoliated samples.[48, 49, 50, 51, 52, 53] Although the sample quality and ability to transfer is limited compared to mechanically exfoliated samples, experiments that require macroscopic sample area can only be performed on grown samples. Furthermore, this may be the only option for industrial application.

The techniques developed for sample preparation made it possible for experimental study of rhombohedral trilayer graphene. In 2011, Kumar et al[54] performed electrical transport measurement on rhombohedral trilayer graphene samples and observed quantum Hall effect. Since their samples have only one gate electrode, it is not possible to control the electrical displacement field to modulate the band gap. Soon after this observation, the gate-tunable band gap was observed in dual-gated samples by Lui et al[55] with infrared optical conductivity measurement (right after their development of the Raman screening technique) and by Zhang et al[56] with electrical transport measurement. With improved fabrication process, Zou et al[57] was able to apply a very large electrical displacement field across the sample and found that the band gap saturates, consistent with Hartree Fock calculations.

With the increased sample quality, phenomena beyond single-electron band theory started to be observed in experiment. In 2014, Lee et al[58] fabricated suspended rhombohedral trilayer graphene samples which effectively suppressed disorder effects. While not straightforward, their observation, for the first time, show signature of electron-electron correlation effect. Apart from electrical measurement, scanning tunneling microscopy[59, 59] and magneto-Raman spectroscopy[60] were also performed on rhombohedral graphene trilayer and multiplayer. Both experiments show evidence of surface states with flat dis-

persion relations. Recently, smoking gun observation electron-electron correlation was made by Lee et al[61] and Shi et al[62], where the transport measurement shows hysteretic behaviors with both magnetic field and carrier density.

Apart from intrinsic rhombohedral trilayer and multilayer graphene. A series of experiment by Chen et al[8, 63, 64] show that by encapsulating rhombohedral trilayer graphene with hexagonal boron nitride and have their lattice axis aligned, the morié potential can open up an energy gap and induce isolated flat energy band. Features similar to those in twisted graphene systems such as correlated insulating states, ferromagnetism and signature of superconductivity are observed.

## 1.4 Outline of the rest chapters

In this work, I will discuss our experimental study of rhombohedral trilayer graphene based on cryogenic electrical measurements. Chapter 2 discuss the theoretical tools we used to model and explain the experimental observation, including the continuum model and stoner type interaction terms. Chapter 3 discuss in detail the experimental techniques we applied, including sample fabrication and electrical measurements. Chapter 4 and 5 discuss our main experimental results, the spin- and valley ferromagnetism and superconductivity respectively. For ferromagnetism, simulation results from the Stoner model is discussed in detail as it reproduces the major experimental phenomena. For superconductivity, we do not have a clear explanation of the mechanism behind, and therefore we only provide several possible explanations. This work also studied rhombohedral trilayer graphene / hexagonal boron nitride superlattice system, which is discussed in Chapter 6. Our experiments are far from comprehensive, we gave a brief summary of our finds in Chapter 7 and also discuss briefly several promising future experiments.

# Chapter 2

## Theoretical Background

### 2.1 Overview

This chapter discusses the theoretical models used to study the electronic properties of rhombohedral trilayer graphene. The non-interaction band structure are calculated with a six-band continuum model, which is obtained from tight-bind approximation and expand the lattice momentum in the long-wave limit. We start from the monolayer graphene case and then generalize to rhombohedral trilayer graphene. To study magnetism, we build a rigid band model to include electron-electron interactions.

### 2.2 Continuum Model

#### 2.2.1 Monolayer Graphene

Graphene is a two-dimensional crystal of carbon[9, 65, 65, 66]. A carbon atom contains four valence electrons, occupying the  $1s$ -orbital and three  $2p$ -orbitals ( $2p^x$ ,  $2p^y$  and  $2p^z$ ). When forming graphene, like in graphite, the valence electrons undergo a  $sp^2$  - hybridization. Three of the electrons forms three  $sp^2$  orbitals. These orbitals are paired



among atoms to form stable covalence bonds, resulting in a honeycomb lattice. The other electron does not form covalence bonds, it instead occupies the unhybridized  $p_z$  orbital that is perpendicular to the honeycomb lattice plane. These  $p_z$ -orbitals of adjacent carbon atoms overlap and form a  $\Pi$ -orbital, in which electrons are itinerant and contribute electrical conduction. Only electrons in the  $\Pi$ -orbital needs to be considered to build the energy band model.

### The honeycomb lattice

The honeycomb lattice contains two inequivalent sites and therefore is not a Bravais lattice. It can be treated as a triangular lattice with A- and B- sublattice sites (Fig. 2.1). The lattice constant is  $a = 0.246\text{nm}$ [66]. The basis of Bravais lattice vectors can be represented as

$$\mathbf{a}_1 = (a, 0), \quad \mathbf{a}_2 = \left(\frac{1}{2}a, \frac{\sqrt{3}}{2}a\right), \quad (2.1)$$

and the vector that connects sublattice A and its nearest neighbor is

$$\boldsymbol{\delta}_1 = \left(\frac{1}{2}a, \frac{a}{2\sqrt{3}}\right), \quad \boldsymbol{\delta}_2 = \left(-\frac{1}{2}a, \frac{a}{2\sqrt{3}}\right), \quad \boldsymbol{\delta}_3 = \left(0, -\frac{a}{\sqrt{3}}\right) \quad (2.2)$$

### Tight-binding Approximation

Although the  $\Pi$ -electrons are itinerant in nature. The tight-binding approximation[67] turns out to be a good approach to capture the energy band properties of graphene. Define  $a_i^\dagger(a_i)$  and  $b_i^\dagger(b_i)$  as the creation(annihilation) operator of electrons on sublattice A and B of the  $i$ th unit cell respectively, and consider only nearest neighbor hopping, the

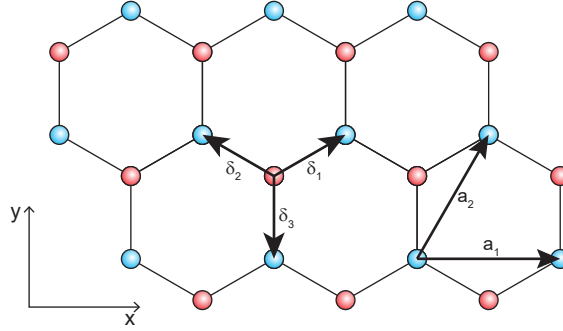


Figure 2.1: Crystal structure of monolayer graphene. Circles rendered in red and blue represent the sublattice A and B respectively.

non-interacting Hamiltonian can be written as

$$H_0 = \gamma_0 \sum_{\langle i,j \rangle} a_i^\dagger b_j + \text{h.c.} \quad (2.3)$$

where  $\gamma_0$  is the hopping integral of nearest sublattice sites and  $\langle \rangle$  means the summation only runs over terms when the  $i$ th and  $j$ th unit cells are nearest neighbors. H.c. means Hermitian conjugate.

To calculate the dispersion relation, we transform from lattice space to the momentum space by using

$$a_i^\dagger = \frac{1}{\sqrt{N}} e^{i\mathbf{k}\cdot\mathbf{r}_i} a_{\mathbf{k}}^\dagger, \quad a_i = \frac{1}{\sqrt{N}} e^{i\mathbf{k}\cdot\mathbf{r}_i} a_{\mathbf{k}} \quad (2.4)$$

where  $N$  is the total number of unit cells. Substituting 2.4 into 2.3,

$$\begin{aligned}
H_0 &= \gamma_0 \sum_{i=1,2,3} \sum_{\mathbf{k}} e^{-i\mathbf{k}\cdot\delta_i} a_{\mathbf{k}}^\dagger b_{\mathbf{k}} + \text{h.c.} \\
&= \begin{pmatrix} a_{\mathbf{k}}^\dagger & b_{\mathbf{k}}^\dagger \end{pmatrix} \begin{pmatrix} 0 & \gamma_0 g(\mathbf{k})^* \\ \gamma_0 g(\mathbf{k}) & 0 \end{pmatrix} \begin{pmatrix} a_{\mathbf{k}} \\ b_{\mathbf{k}} \end{pmatrix} \\
&\equiv \begin{pmatrix} a_{\mathbf{k}}^\dagger & b_{\mathbf{k}}^\dagger \end{pmatrix} h(\mathbf{k}) \begin{pmatrix} a_{\mathbf{k}} \\ b_{\mathbf{k}} \end{pmatrix}.
\end{aligned} \tag{2.5}$$

where

$$g(\mathbf{k}) = \sum_{i=1}^3 e^{i\mathbf{k}\cdot\delta_i} \tag{2.6}$$

The dispersion relation can be obtained by diagonalizing  $h(\mathbf{k})$ , which is

$$\begin{aligned}
E(\mathbf{k}) &= \pm \gamma_0 \sqrt{3 + 4 \cos \frac{\sqrt{3}}{2} k_x a \cos \frac{1}{2} k_y a + 2 \cos k_y a} \\
&\equiv \pm \gamma_0 \sqrt{3 + f(\mathbf{k})}
\end{aligned} \tag{2.7}$$

where

$$f(\mathbf{k}) = 4 \cos \frac{\sqrt{3}}{2} k_x a \cos \frac{1}{2} k_y a + 2 \cos k_y a \tag{2.8}$$

The dispersion is plotted in Fig. 2.2a. The energy become zero for both of the two bands when  $\mathbf{k} = \mathbf{K} = (\frac{2\pi}{\sqrt{3}a}, 1)$  or  $\mathbf{k} = \mathbf{K}' = (\frac{2\pi}{\sqrt{3}a}, -1)$ . The high symmetry points  $K$  and  $K'$  are called the "Dirac points". Their locations in the reciprocal space are shown in Fig. 2.2b.

### Continuum limit

By fitting the tight-binding model with first principle calculations, the nearest hopping integral  $\gamma_0$  is around 2.8eV[68]. When only low energy physics are considered, the

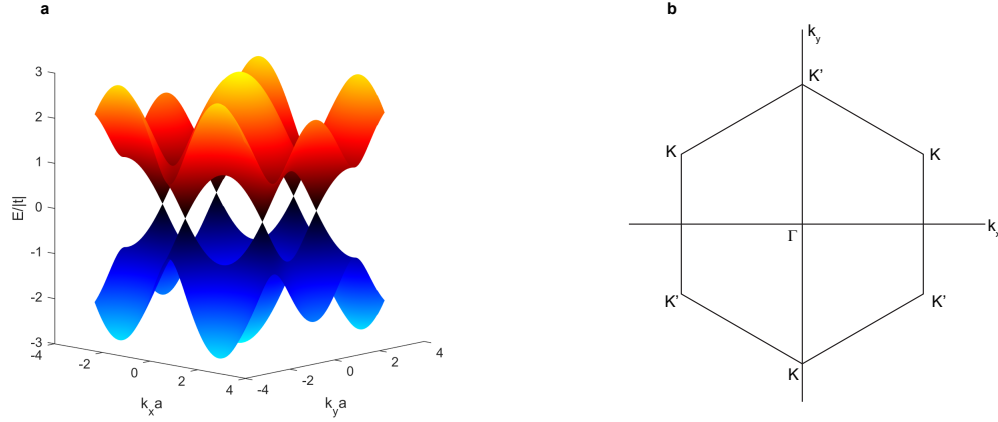


Figure 2.2: Band structure of monolayer graphene. **a**, Energy band dispersion of the monolayer graphene calculated from the tight-binding model. **b**, First Brillouin zone of monolayer graphene.

electron excitations happen only near the Dirac points. In this case, the wavevector  $k$  can be expanded around  $K$  and  $K'$  to simplify the model. Define  $\mathbf{q} = \mathbf{k} - \mathbf{K}$ . Near the  $K$  point,

$$g(\mathbf{k}) = \sum_{i=1}^3 e^{i(\mathbf{K}+\mathbf{q})\cdot\delta_i} \quad (2.9)$$

$$\approx -ie^{-iK_x a} \frac{3a}{2} (q_x + iq_y)$$

In the second line, only the linear term of  $\mathbf{q}$  is kept. After ignoring a global phase factor, the Hamiltonian

$$h(\mathbf{k}) = h(\mathbf{K} + \mathbf{q}) = v_0 \begin{pmatrix} 0 & \pi^\dagger \\ \pi & 0 \end{pmatrix} \quad (2.10)$$

where  $v_0 = \frac{\sqrt{3}a\gamma_0}{2}$  is the Fermi velocity.  $\pi = p_x - ip_y$ ,  $\pi^\dagger = p_x + ip_y$ .

Similarly, expanding  $\mathbf{k}$  near the  $K'$ -point gives

$$h(\mathbf{k}) = h(\mathbf{K}' + \mathbf{q}) = v_0 \begin{pmatrix} 0 & \pi \\ \pi^\dagger & 0 \end{pmatrix} \quad (2.11)$$

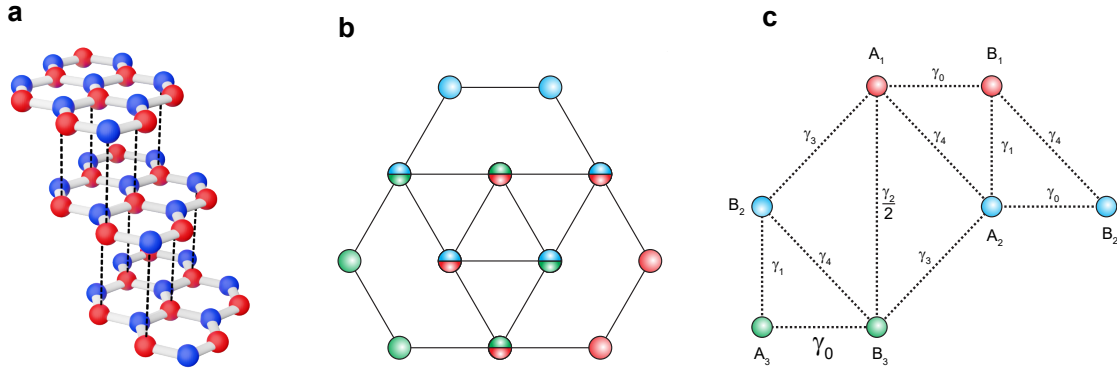


Figure 2.3: Lattice structure of the rhombohedral trilayer graphene.

In the continuum limit, the Dirac points  $K$  and  $K'$  are treated as a discrete degree of freedom with binary values. This degree of freedom is similar to the electron spin, called the "valley". Strictly speaking, valley is not an intrinsic degree of freedom, instead, it is a result of the dispersion relation. However, when the energy scale involved is much smaller than  $\gamma_0$ , such treatment is a good approximation.

### 2.2.2 Continuum Model of Rhombohedral Trilayer Graphene

The lattice structure of rhombohedral trilayer graphene is shown in Fig. 2.3a. It is a chiral generalization of monolayer and Bernal bilayer graphene[23]. The previous described tight-binding approach and small momentum expansion can be generalized to build the Hamiltonian of rhombohedral trilayer graphene. Instead of having two sublattices  $A$  and  $B$ , the rhombohedral trilayer graphene contains six sublattices in its unit cell,  $A_1$ ,  $B_1$ ,  $A_2$ ,  $B_2$ ,  $A_3$  and  $B_3$ , where  $A$  and  $B$  represent the sublattices of the individual layers, like in the monolayer case, while the Arabic numbers 1, 2, 3 represent the layers. The hopping between different sublattice sites (see Fig. 2.3c) needs to be considered to give a precise description of the band structure.

The tight-binding Hamiltonian can be written as

$$H_0 = \sum_{\mathbf{k}} \begin{pmatrix} a_{1,\mathbf{k}}^\dagger & b_{3,\mathbf{k}}^\dagger & b_{1,\mathbf{k}}^\dagger & a_{2,\mathbf{k}}^\dagger & b_{2,\mathbf{k}}^\dagger & a_{3,\mathbf{k}}^\dagger \end{pmatrix} h(\mathbf{k}) \begin{pmatrix} a_{1,\mathbf{k}} \\ b_{3,\mathbf{k}} \\ b_{1,\mathbf{k}} \\ a_{2,\mathbf{k}} \\ b_{2,\mathbf{k}} \\ a_{3,\mathbf{k}} \end{pmatrix} \quad (2.12)$$

where  $a_{n,\mathbf{k}}$  ( $a_{n,\mathbf{k}}^\dagger$ ) and  $b_{n,\mathbf{k}}$  ( $b_{n,\mathbf{k}}^\dagger$ ) are the annihilation (creation) operators of electrons on layer  $n$  and sublattice A and B respectively, and

$$h(\mathbf{k}) = \begin{pmatrix} \Delta_1 + \Delta_2 + \delta & \frac{1}{2}\gamma_2 & \gamma_0 g(\mathbf{k})^* & \gamma_4 g(\mathbf{k})^* & \gamma_3 g(\mathbf{k}) & 0 \\ \frac{1}{2}\gamma_2 & \Delta_2 - \Delta_1 + \delta & 0 & \gamma_3 g(\mathbf{k})^* & \gamma_4 g(\mathbf{k}) & \gamma_0 g(\mathbf{k}) \\ \gamma_0 g(\mathbf{k}) & 0 & \Delta_1 + \Delta_2 & \gamma_1 & \gamma_0 g(\mathbf{k})^* & \gamma_4 g(\mathbf{k})^* \\ \gamma_4 g(\mathbf{k}) & \gamma_3 g(\mathbf{k}) & \gamma_1 & -2\Delta_2 & \gamma_0 g(\mathbf{k})^* & \gamma_4 g(\mathbf{k})^* \\ \gamma_3 g(\mathbf{k})^* & \gamma_4 g(\mathbf{k})^* & \gamma_4 g(\mathbf{k}) & \gamma_0 g(\mathbf{k}) & -2\Delta_2 & \gamma_1 \\ 0 & \gamma_0 g(\mathbf{k})^* & 0 & \gamma_4 g(\mathbf{k}) & \gamma_1 & \Delta_2 - \Delta_1 \end{pmatrix} \quad (2.13)$$

where  $g(\mathbf{k})$  follows the same definition in Eq. 2.6.  $\gamma_i$ 's are the hopping integral between sublattices indicated in Fig. 2.3c. The hopping between sublattice  $A_1$  and  $A_3$ , between  $B_1$  and  $B_3$  and between  $A_1$  and  $B_3$  are ignored.  $\Delta_1$  is the potential difference between the top and bottom layer.  $\Delta_2$  is the difference between the potential of the central layer and the mean-field potential of the outer layers.  $\delta$  is the potential difference between coupled and uncoupled sublattice sites.  $\Delta_1$  can be controlled by applying a perpendicular electrical displacement field. The rest parameters are listed in Table. 2.1. The parameter sets were based on [69] and [70] with small change to fit the experimental data.

$\gamma_0$	$\gamma_1$	$\gamma_2$	$\gamma_3$	$\gamma_4$	$\delta$	$\Delta_2$
3.1	0.38	-0.015	-0.29	-0.141	-0.0105	-0.0023

Table 2.1: Values of tight binding parameters for rhombohedral trilayer graphene used. All numbers are in unit of eV.

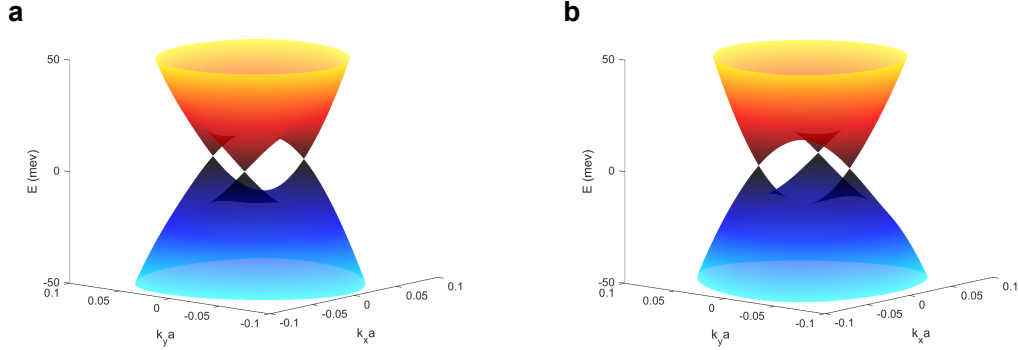


Figure 2.4: Band structure of rhombohedral trilayer graphene calculated from the continuum model. a, Band structure near valley  $K$ . b, Band structure near valley  $K'$ .

Applying the small momentum expansion in Eq. 2.9 and define  $v_i = \frac{\sqrt{3}a}{2}\gamma_i$ , we obtained the six-band continuum model of rhombohedral trilayer graphene near valley  $K$

$$h(\mathbf{k}) = \begin{pmatrix} \Delta_1 + \Delta_2 + \delta & \frac{1}{2}\gamma_2 & v_0\pi^\dagger & v_4\pi^\dagger & v_3\pi & 0 \\ \frac{1}{2}\gamma_2 & \Delta_2 - \Delta_1 + \delta & 0 & v_3\pi^\dagger & v_4\pi & v_0\pi \\ v_0\pi & 0 & \Delta_1 + \Delta_2 & \gamma_1 & v_0\pi^\dagger & v_4\pi^\dagger \\ v_4\pi & v_3\pi^\dagger & \gamma_1 & -2\Delta_2 & v_0\pi^\dagger & v_4\pi^\dagger \\ v_3\pi^\dagger & v_4\pi^\dagger & v_4\pi^\dagger & v_0\pi & -2\Delta_2 & \gamma_1 \\ 0 & v_0\pi^\dagger & 0 & v_4\pi & \gamma_1 & \Delta_2 - \Delta_1 \end{pmatrix} \quad (2.14)$$

The Hamiltonian near valley  $K'$  can be obtained by replacing  $k_x$  with  $-k_x$  in Eq. 2.14

The band dispersion relation can be obtained by numerically diagonalizing Eq. 2.14. The basic procedure is to first discrete the  $k_x$  and  $k_y$  points in the momentum space. For each discrete value of  $k_x$  and  $k_y$ , we calculate the eigenvalues of the (numerical) matrix

$h(\mathbf{k})$ , which gives the energy of the six bands at  $(k_x, k_y)$ . The result for  $\Delta_1 = 0$  is shown in Fig. 2.4. Only the two low energy bands are shown.

Near the  $K$  and  $K'$  points, the conduction and valence bands touch with each other from three "pockets". The presence of the "pockets" is called "trigonal warping" [71, 72], which is mainly contributed by the interlayer hopping between sites that are right on the top and the bottom of each other. In between two adjacent pockets, there is a saddle point. The saddle points play an important role in determine the electronic properties rhombohedral trilayer graphene, which will be discussed in detail later.

### 2.2.3 Carrier Density, Density of States and Van Hove Singularity

With the energy band dispersion relation known, we can calculate the energy dependence of carrier density  $n_e(E)$  and the density of states  $D(E)$ . At finite temperature, the energy  $E$  is replaced by the chemical potential  $\mu$ .

The carrier density  $n_e = N_e/A$ , where  $N_e$  is the number of carriers in the system,  $A$  is the area.  $N_e$  can be calculated by summing up all the occupied states in the momentum space. When the chemical potential is  $\mu$ ,

$$N_e = \sum_n \sum_{\mathbf{k} \in \text{BZ}} f(\epsilon_n(\mathbf{k})) \quad (2.15)$$

where

$$f(\epsilon) = \frac{1}{e^{(\epsilon-\mu)/k_B T} + 1} \quad (2.16)$$

is the Fermi-Dirac distribution function.

Numerical calculation of  $N_e$  requires to discretize the  $\mathbf{k}$  points in the momentum space. Although the  $\mathbf{k}$  points are discrete in nature due to the finite size of the system,



the typical grid size of numerical calculations are much larger than the actual grid size. More precisely, suppose the sampling spacing of  $k_x$  and  $k_y$  are  $\Delta k_x$  and  $\Delta k_y$ , and the length scale of the system is  $L$ , then

$$\Delta k_x, \Delta k_y \gg \frac{1}{L} \quad (2.17)$$

The numerical discretization of  $\mathbf{k}$  divides the momentum space into multiple cells  $C_1, C_2, \dots$  each cell occupy an area of  $\Delta k_x \Delta k_y$ . The  $\mathbf{k}$  points in the momentum space can be grouped based on which cell they belong to.

$$\begin{aligned} N_e &= \sum_{\mathbf{k} \in \text{BZ}} f(\epsilon(\mathbf{k})) \\ &= \sum_i \sum_{\mathbf{k} \in C_i} f(\epsilon(\mathbf{k})) \\ &= \sum_i N_i f(\epsilon(\mathbf{k}_i)) \end{aligned} \quad (2.18)$$

where in the last line, the value of  $\epsilon(\mathbf{k})$  is replaced by the value of the sampled point  $\epsilon(\mathbf{k}_i)$ .  $N_i$  is the number of  $\mathbf{k}$  in  $C_i$ . Since the density of  $\mathbf{k}$  points in the momentum space is  $A/(2\pi)$ ,

$$N_i = \frac{A}{2\pi} \Delta k_x \Delta k_y \quad (2.19)$$

Substituting Eq. 2.19 in to Eq. 2.18,

$$N_e = \sum_{k_{ix}, k_{iy}} \Delta k_x \Delta k_y \frac{A}{(2\pi)^2} f(\epsilon(\mathbf{k}_i)) \quad (2.20)$$

and

$$n_e = \frac{N_e}{A} = \sum_{k_{ix}, k_{iy}} \frac{\Delta k_x \Delta k_y}{(2\pi)^2} f(\epsilon(\mathbf{k}_i)) \quad (2.21)$$

Therefore,  $n_e$  can be numerically calculated by summing the occupation probability for

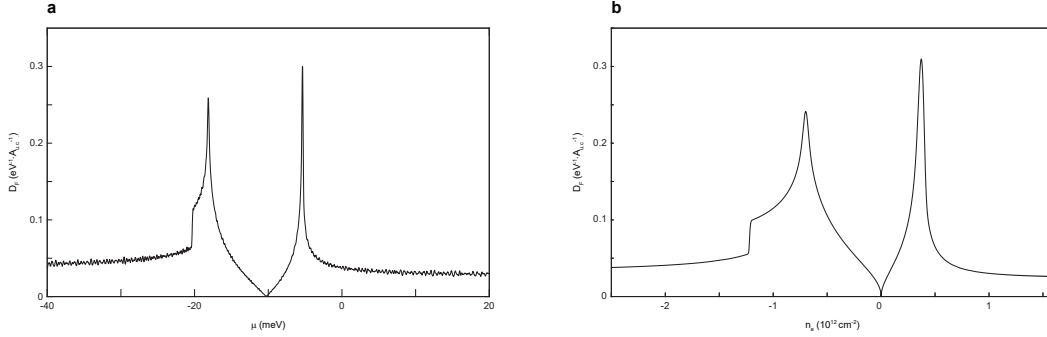


Figure 2.5: Density of states calculated from the six-band continuum model at  $\Delta_1 = 0$ . a,  $D_F$  as a function of chemical potential. b,  $D_F$  as a function of carrier density  $n_e$ .  $A_{\text{u.c.}}$  is the area of the unit cell.

all possible states in the discrete lattice momentum space.

The density of states at the Fermi surface  $D_F$  can be calculated by taking the numerical derivative of  $n_e$ ,

$$D_F(\mu) = \frac{\Delta n_e}{\Delta \mu} \quad (2.22)$$

The calculated  $D_F$  is shown in fig. 2.5, plotted as a function of the chemical potential, and carrier density respectively. Without doping ( $n_e = 0$ ),  $D_F = 0$ , which is a property of semimetal. In the conduction and valence band, there is a peak in the density of states profile, they are originated from the saddle points of the energy band.

Alternatively,  $D_F$  can be calculated by convert the summation of  $\mathbf{k}$  into an integral

$$\frac{1}{A} \sum_{k_x, k_y} = \frac{1}{(2\pi)^2} \int dk_x dk_y \quad (2.23)$$

This is a good approximation for dense  $\mathbf{k}$ -grids. By using Eqn. 2.23 in Eqn. 2.15, and applying Stokes theorem,

$$D_F(\epsilon_n) = \frac{1}{4\pi^2} \sum_n \int_{S_n} \frac{dk_x dk_y}{|\nabla_{\mathbf{k}} \epsilon(\mathbf{k})|} \quad (2.24)$$

Here the intrinsic spin and valley degree of freedom are ignored. The integrand is singular at the band extrema, where  $\nabla_{\mathbf{k}}\epsilon(\mathbf{k}) = 0$ . It can be proved that for a two-dimensional system, the integral also diverges if the extrema is a saddle point, which is called a Van Hove singularity[73]. The peaks in Fig. 2.5a and b are originated from the Van Hove singularities.

## 2.3 Rigid-band Model of Interaction

The electron magnetism is a result of Coulomb interaction and cannot be captured by the single-electron continuum model. A typical model to characterize magnetism is the Hubbard model[74].

$$H = \sum_{i,j} T_{i,j} \sum_{\sigma} a_{i\sigma}^{\dagger} a_{j\sigma} + \frac{1}{2} U \sum_i \sum_{\sigma=\uparrow,\downarrow} n_{i\sigma} n_{i-\sigma} \quad (2.25)$$

where  $\sigma$  labels the electron spin, and

$$n_{i\sigma} = a_{i\sigma}^{\dagger} a_{i\sigma} \quad (2.26)$$

is the electron density operator. In the Hubbard model, the first term is the single-electron kinetic energy, expressed in the Wannier basis, and often treated with tight-binding approximation.  $T_{ij}$  is the hopping integral between different lattice sites. The second term characterizes the electron-electron interaction, where  $U$  is a real parameter that characterizes the interaction strength. This term disfavors a state where two electrons with opposite spin occupy the same lattice site. In rhombohedral trilayer graphene, the electrons has both spin and valley degree of freedom. The Hubbard model needs to be

extended to include four flavors.

$$\begin{aligned}
H &= \sum_{i,j} T_{i,j,\alpha} a_{i\alpha}^\dagger a_{j\alpha} + \frac{1}{2}U \sum_i \sum_{\alpha \neq \beta} n_{i\alpha} n_{i\beta}, \quad \alpha, \beta = (K \uparrow, K \downarrow, K' \uparrow, K' \downarrow) \\
&\equiv H_0 + H_1
\end{aligned} \tag{2.27}$$

where we define the kinetic energy and interaction to be  $H_0$  and  $H_1$  respectively.

The Hubbard model is analytically unsolvable. Even numerical calculation is complicated. We can apply approximation to simplify it. For  $H_0$ , we apply tight-bind approximation and continuum limit, as we did in the previous section. More specifically, we replace  $H_0$  with Eq. 2.14 and Eq. 2.12. For  $H_1$ , we first apply the random phase approximation[75] which ignored the second-order terms of density fluctuation

$$\begin{aligned}
H_1 &= \frac{1}{2}U \sum_i \sum_{\alpha \neq \beta} n_{i\alpha} n_{i\beta} \\
&\approx \frac{1}{2}U \sum_i \sum_{\alpha \neq \beta} \langle n_{i\alpha} \rangle \langle n_{i\beta} \rangle \\
&= \frac{1}{2}UN \sum_{\alpha \neq \beta} \langle n_\alpha \rangle \langle n_\beta \rangle \quad \alpha, \beta = (K \uparrow, K \downarrow, K' \uparrow, K' \downarrow)
\end{aligned} \tag{2.28}$$

where in the second line, the density operators are replaced with its expectation values (random phase approximation). In the third line, the lattice site indices are removed because of the translational symmetry of the system. A further approximation can be made by assuming the density of states is independent of interaction and carrier density, which is called the rigid-band approximation.

$$\begin{aligned}
H_1 &= \frac{1}{2}UN \sum_{\alpha \neq \beta} \langle n_\alpha \rangle \langle n_\beta \rangle \\
&\approx \frac{1}{2}UN \sum_{\alpha \neq \beta} \langle n_\alpha \rangle_0 \langle n_\beta \rangle_0 \quad \alpha, \beta = (K \uparrow, K \downarrow, K' \uparrow, K' \downarrow)
\end{aligned} \tag{2.29}$$

With the rigid-band approximation applied, the relation between chemical potential and carrier density within each spin- and valley-flavor is independent of the interaction and can be completely determined by the non-interaction band dispersion relation, as discussed in the previous section. The problem to solve is: at a fixed total carrier density

$$n = n_{K\uparrow} + n_{K\downarrow} + n_{K'\uparrow} + n_{K'\downarrow}, \quad (2.30)$$

find a parameter set of  $(n_{K\uparrow}, n_{K\downarrow}, n_{K'\uparrow}, n_{K'\downarrow})$ , such that the total energy of the system

$$E = \sum_{\alpha} E_0(\mu_{\alpha}) + \frac{1}{2}UN \sum_{\alpha \neq \beta} n_{\alpha}n_{\beta} \quad (2.31)$$

is minimized and the constriction 2.30 is satisfied. The ground state of the system is completely determined by the parameter set  $(n_{K\uparrow}, n_{K\downarrow}, n_{K'\uparrow}, n_{K'\downarrow})$ .

In Eq. 2.31, the density  $n_{\alpha}$  and total kinetic energy  $E(\mu_{\alpha})$  is completely determined by the energy band dispersion relation.

$$n_{\alpha} = \int_0^{\mu} D(\epsilon) d\epsilon \quad (2.32)$$

$$E(\mu_{\alpha}) = \int_0^{\mu} \epsilon D(\epsilon) d\epsilon \quad (2.33)$$

Although the interaction in the rigid-band model is deeply simplified, it turns out to be good enough to capture the magnetic phase transitions in the rhombohedral trilayer graphene. And the minimized computation scale allows for thoroughly exploration of the parameter space. The model 2.31 implicitly assumes the interaction preserved the SU(4) spin- and valley- rotation symmetry, in which case the four spin- and valley- flavors are equivalent. The model can be generalized to situations where the SU(4) symmetry is not

preserved.

$$H_1 = \frac{N}{2} \sum_{\alpha \neq \beta} U_{\alpha\beta} n_\alpha n_\beta \quad (2.34)$$

where  $n_\alpha$  and  $n_\beta$  is still calculated using Eq. 2.32, but the interaction strength is different depending on the spin- and valley-flavor involved[76, 77].

# Chapter 3

## Experimental Techniques

### 3.1 Overview

This chapter discusses the experimental techniques applied to fabricate and measure the rhombohedral trilayer graphene devices. To identify and isolate the metastable rhombohedral trilayer graphene domains, the Raman spectroscopy and atomic force microscope-based cutting is used. The Van der Waals heterostructure is assembled with a dry transfer technique. The transistor geometry is then formed with plasma etching and metal deposition. Fig. 3.1 shows the procedure of device fabrication. The device is characterized by measuring the gate-tuned capacitance and resistance at low temperature. The magneto-resistance measurement and Shubnikov de Haas oscillation analysis is well utilized to resolve the Fermi surface and magnetic ordering. The following sections will discuss these techniques in details.

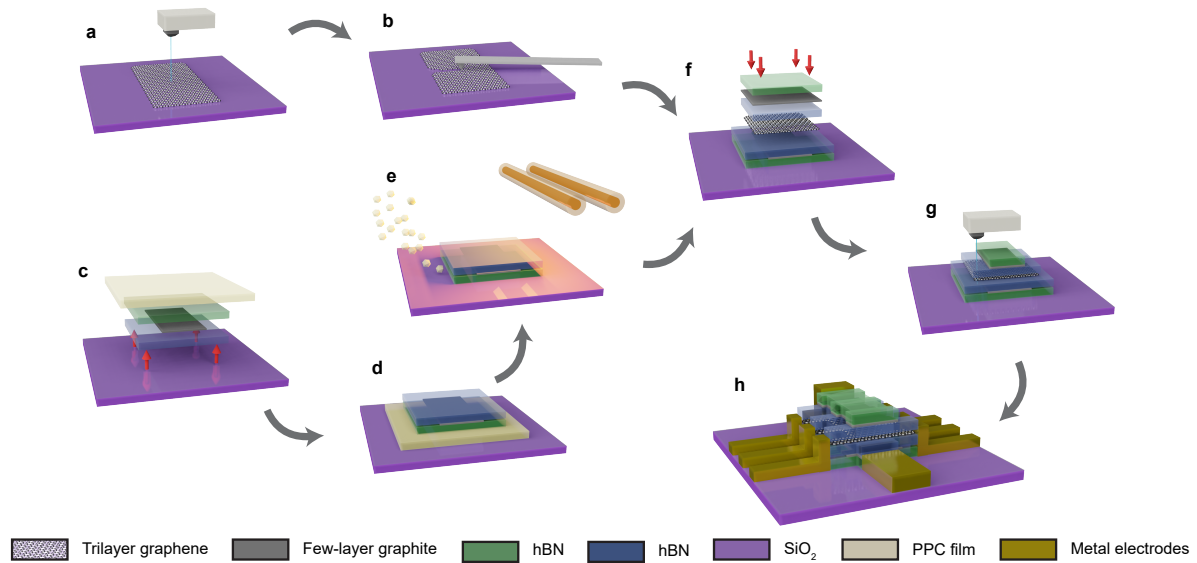


Figure 3.1: Procedure of device fabrication

## 3.2 Sample Fabrication

### 3.2.1 Preparation of the Trilayer Graphene Flakes

#### Mechanical Exfoliation

The trilayer graphene flakes are prepared by exfoliating bulk graphite crystal with tapes. The flakes are then transferred onto a silicon chip with a 285 nm thick dry-grown silicon dioxide layer on the surface. The layer number of a flake can be roughly identified from an optical micrograph. A typical example is shown in Fig.3.2, where the exfoliated flakes contain monolayer, bilayer and trilayer parts.

#### Raman Spectroscopy

While the layer numbers can be identified from the optical image, the stacking order is not distinguishable. We identify the stacking order with Raman spectroscopy[41, 42,



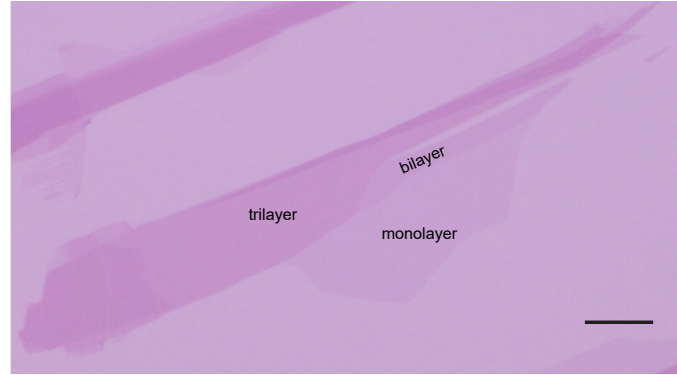


Figure 3.2: Optical micrograph of a typical exfoliated graphene flake on a silicon chip with 285 nm dry oxide layer on the surface. The layer numbers can be identified by the optical contrast. The scale bar represents 10  $\mu\text{m}$ .

43, 44].

Raman scattering is the inelastic scattering of photon by matter. During this process, part of the photon energy is absorbed by the matter. For crystals, the absorbed energy is in the form of lattice vibration, or phonons. Therefore, the energy difference of incident and reflected photons is determined by the phonon modes of the crystal. This energy difference is usually represented by Raman shift, the wave vector difference of incident and reflected light.

Fig. 3.3 shows the typical Raman spectrum of monolayer, bilayer and (bernal-stacked) trilayer graphene, measured with an excitation wavelength of 488nm. The most prominent features of the spectrum two major peaks. One of them is at around  $1580\text{cm}^{-1}$ , usually named the 'G-band'. The other is at around  $2750\text{cm}^{-1}$ , named 'G'-band' or '2D-band'. There are other weak peaks at different Raman shift, and have been studied in details. Both the G-band and 2D-band are originated from the phonon modes of graphene lattice[78].

The G-band corresponding to a two-fold degenerated in-plane transverse optical mode

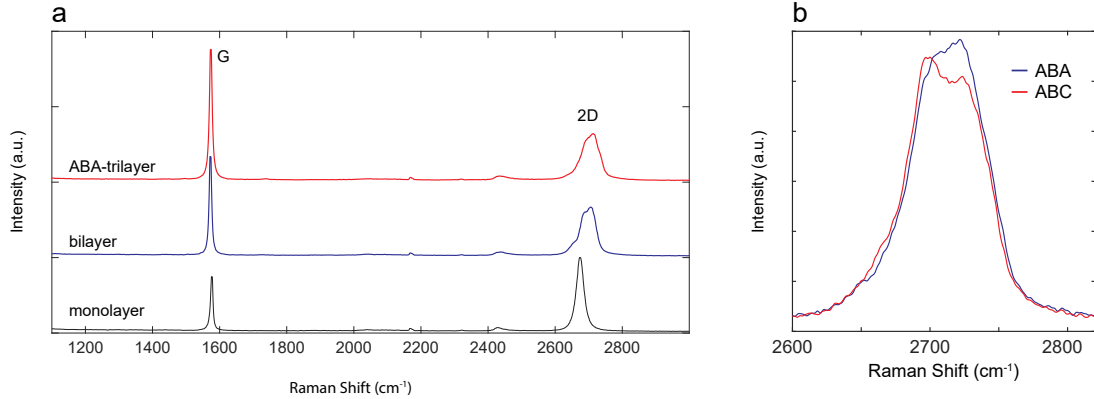


Figure 3.3: Raman spectrum of graphene measured with 488nm excitation. a, Layer-dependence of the Raman spectrum. b, Raman spectrum of ABA- and ABC-stacked trilayer graphene near the 2D-band.

and longitudinal optical phonon mode at the  $\Gamma$ -point of the phonon band Brillouin zone. The 2D-band has a more complex origin. It is a second-order process that is contributed by a combination of the transverse optical mode and an inter-valley scattering. Peak-fitting analysis has shown that the 2D-band contains multiple peaks that have similar energy. In multi-layer graphene, the relative intensity of these peaks is affected by the stacking order. This provides an approach to identify the rhombohedral domains from mechanically exfoliated trilayer graphene flakes.

Fig.3.3b shows the Raman spectrum of ABA- and ABC-stacked trilayer graphene near the 2D-band. The 2D-peak of ABC-stacked trilayer graphene exhibits a stronger asymmetry compare to that of the ABA-stacked trilayer graphene.

The mechanically exfoliated trilayer graphene usually contains both ABA- and ABC-domains. To identify these domains, a spatial map of the Raman spectrum is necessary.

The spacial map can be realized by placing the sample on a step motor-driven XY-stage and measuring the Raman spectrum for each point on the sample. After that, the peak maxima of the 2D-band is extracted for each point. Fig. 3.4 shows the result on an trilayer graphene flake. The optical image of the flake is shown in Fig. 3.4a. The spatial

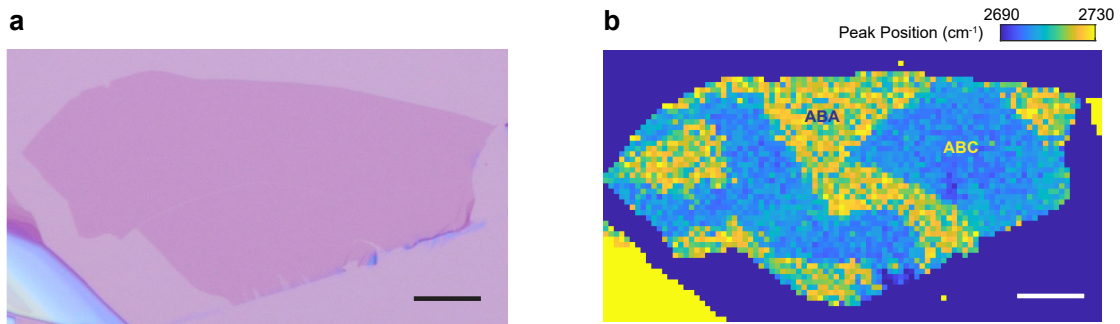


Figure 3.4: Mapping the stacking orders. a, Optical micrograph of a trilayer graphene on silicon/silicon oxide substrate. b, Raman spectrum map of the flake in panel a. The color scale represents the Raman shift value at which the 2D-band reaches the maximal intensity. The scale bar is  $10\mu\text{m}$  in both panels.

map of the Raman spectrum is shown in Fig. 3.4b, where we use color to represent the peak position of the 2D-band. The blue and yellow region corresponds to the ABC- and ABA- stacked domain respectively. The sample contains both type of stacking order, which is the case for most trilayer graphene flakes prepared by mechanical exfoliation.

### Atomic Force Microscope Cutting

As mentioned before, the ground state of trilayer graphene is in ABA-stacking, while the ABC-stacked phase is a metastable state. Therefore, carefulness must be taken to manipulate the ABC-stacked trilayer graphene.

While the ABC-domains are metastable. The domain walls between the ABA- and ABC-domains are unstable and tends to move under perturbation. Therefore, samples contains domains walls are more likely to relax to the stable ABA-phase during the fabrication process. To overcome this problem, we cut the trilayer graphene flakes to isolate the ABC-domains. The conventional technique to cut the micrometer-scaled material is to pattern the material with photoresist/electron-beam resist and etch with corrosive chemicals or plasma. This is not ideal in our situation since the resist will contami-

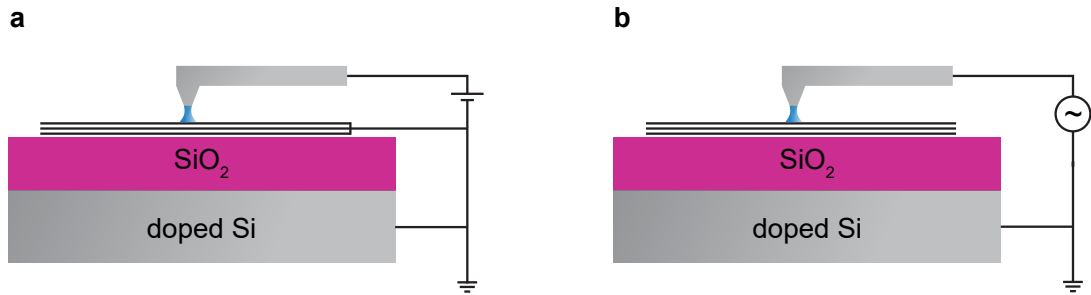


Figure 3.5: Schematics of AFM cutting based on anodic oxidation. a, cutting with a d.c. voltage applied on the probe. The sample needs to be electrically connected to the ground. b, cutting with an a.c. voltage. No electrical connection to the sample is required since it is capacitively coupled to the doped silicon layer.

nate the surface of the trilayer graphene flakes and induce disorder. We instead use a lithography free approach: cut the flake with an atomic force microscope (AFM) probe. Previous works have shown that when an d.c. voltage is applied between the graphene sample and the AFM probe that is close to the sample surface, an electrical-chemical reaction will occur between the water absorbed on the tip end and the graphene and form graphene oxide. The graphene oxide is further removed by the probe as the probe is moving across the sample. In this way, a trench is made along the path of the AFM probe.[79, 80, 81, 82, 83] A schematic of this technique shown in Fig.3.5. This technique has been applied to fabricate graphene tunneling junctions.

However, this technique requires electric access to the graphene. The mechanically exfoliate graphene samples are deposited on a silicon dioxide layer, which is an insulator. Electrical access to the graphene flakes required patterning metal electrodes to the flake. An alternative techniques have recently been developed to solve this problem, which is to replace the d.c. voltage with an a.c. voltage[84]. (Fig. 3.5b. Since the trilayer graphene is capacitively coupled to the doped-silicon substrate, a current can go through the graphene even no electrical connection is directly made to the graphene flake.

The actual experiment was performed on a dimension Icon AFM with SCM-PIT-V2

probe. The front side of the probe is coated with a platinum/iridium alloy coating layer which is electrically conductive. When cutting the sample, the tip is engaged to the sample in contact AFM mode. An a.c. voltage with 10V amplitude and 10kHz frequency is applied on the tip. The a.c. voltage is generated by an internal oscillator of the AFM controller, but may also be generated by an external instrument. Since the reaction is between graphene and water absorbed on the probe apex. A humidity control is required if the relative humidity of the environment is below 50%. Usually higher humidity gives better results, but also increase the risk of electrical breakdown of the piezo scanner. In practice, we control the humidity within the range of 50% to 80%. While cutting, the tip is moving at a speed of 300 nm/s. Although the trench can be made with higher speed ( $> 1\mu\text{m/s}$ ), it turns out that it increases the chance for the ABC-domains to relax to the ABA-phase. The width of the trench made is usually 50 nm to 100 nm wide.

Fig. 3.6 shows a typical result of AFM cutting. The exfoliated trilayer (a) graphene sample is firstly checked with Raman spectroscopy to locate the ABC-stacked domains (b). Multiple trenches are made within the ABC-stacked domains by AFM cutting so that the regions labeled with numbers 1,2,3 are purely in ABC-stacking order(c). For sufficiently large samples, the ABC-domains are usually divided into several regions to increase the chance of preserving the stacking order after fabrication.

An interesting fact is that the AFM cutting technique does not make reliable electrical isolation, especially when the trench is not a straight line. This is not an issue for our purpose since a trench can effectively remove the domain walls even if it does not completely electrically isolate the regions it separated. Carefulness must be taken, however, when this technique is used for other purposes such as forming complicate gate structures.

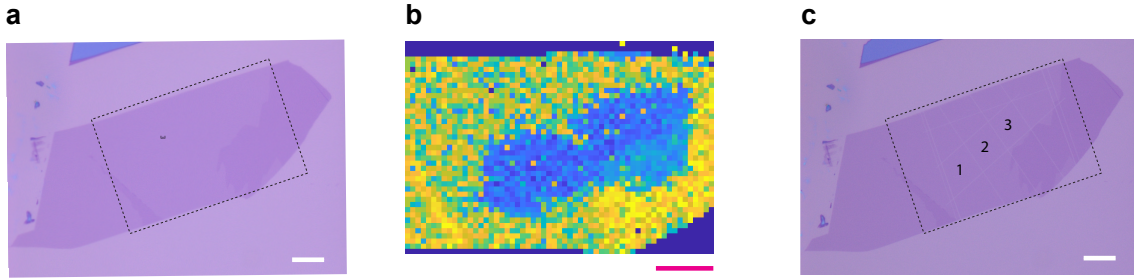


Figure 3.6: Isolating the ABC domains by AFM cutting. a, Optical micrograph of a trilayer graphene sample. The scale bar represents  $10\mu\text{m}$ . b, Raman spectrum map of the sample in a. The approximate scan range is indicated by black dashed lines in a. The sample has both ABA- and ABC- stacked phases. The blue region is the ABC domain. The scale bar represents  $10\mu\text{m}$ . c, Optical micrograph of the same sample in a after AFM cutting. The trenches are visible under the microscope and divides the sample into multiple pieces. The regions labeled 1,2,3 are within the ABC-phase determined by the Raman spectroscopy and will be used to fabricate devices. The scale bar represents  $10\mu\text{m}$ .

### 3.2.2 Preparation of the Van der Waals Heterostructures

In order to electrically tune the carrier density and apply interlayer potential, the RTG needs to be fabricated into a heterostructure[85] with gate electrodes on both sides. The gates need to be close to but electrically isolated from the RTG. This can be achieved by separate the gates from the RTG with a hexagonal boron nitride (hBN) layer. This technique is developed by Dean et al[86] and since then are widely used in the two-dimensional material community.

The hBN is a layered material with a band gap of  $5.95\text{eV}$ . It shares similar crystal structure to graphite. Each layer forms a honeycomb lattice with boron and nitrogen atoms sit on the A- and B- sublattice sites. The lattice constant of hBN is  $2.504\text{\AA}$ , close to the value of graphite. Experiment has shown that the disorder effects of graphene and its multilayer can be significantly suppressed by putting the graphene layer on top of hBN or encapsulate the graphene layer with two hBN layers. This makes hBN an ideal dielectric material for the RTG devices.

The gates need to be made from electrically conductive material, so that a voltage can be applied on it. The conventional technique is to deposit metal on top of the dielectrics. The metal, however, usually induces disorder to the system and makes it challenging to probe electrical properties of the graphene layer with small energy scale such as fractional quantum Hall effect. This can be improved by replacing the metal gates with multilayer graphite gates, which can be obtained by mechanical exfoliation, same as RTG. Unlike metal, the gate electrodes formed by multilayer graphite is a single-crystal with flat surface in the atomic scale. Comparison of capacitance measurement on metal-gated and graphite-gated bilayer graphene devices has shown significant improvements from the graphite gates. The thickness of graphite gates is typically chosen between 5 nm to 10 nm. The gates need to be thick enough so that it shows good metallic nature. This is important for capacitance measurement where the density of states variation of the gates can induce additional signal, especially when a strong magnetic field is applied. For transport measurement, however, such effect is not obvious and even monolayer graphene gates give good results. On the other hand, a thick gate increases the difficulty in device fabrication because it takes longer to etch and requires thicker metal electrodes to make electrical contacts.

With few-layer graphite gates and hBN dielectric, the cross-section structure of the heterostructure is shown in Fig. 3.7.

The heterostructure is assembled by transferring the exfoliated flakes with polypropylene carbonate (PPC) film[87], which is a polymer that can stick to graphene and hBN flakes with Van der Waals force. The PPC film is mounted on a microscope slide and using polydimethylsiloxane (PDMS) as an elastic substrate. The basic structure of the pickup slide assembly is shown in Fig. 3.8.

The conventional procedure is to assemble the heterostructure from top to bottom. The hBN on the top is picked up first, followed by the top graphite gate layer, the

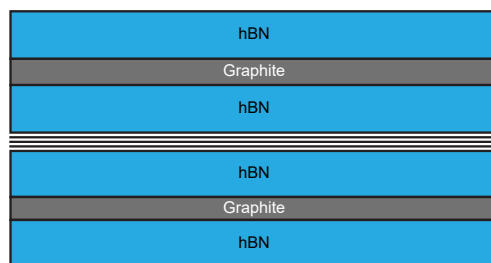


Figure 3.7: Cross-section of the dual-graphite gated RTG heterostructure.

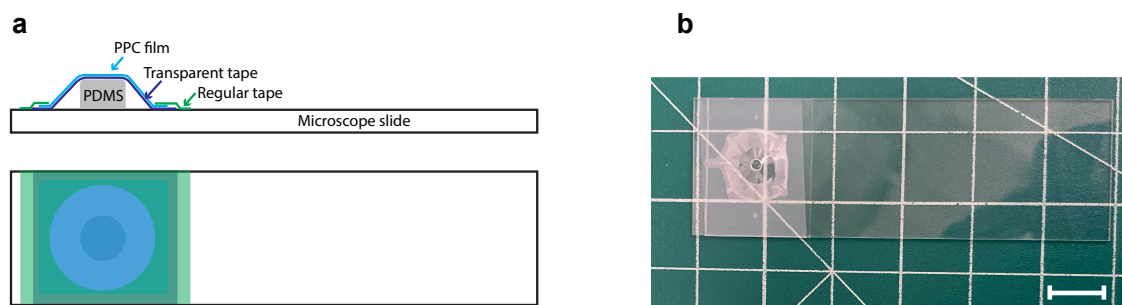


Figure 3.8: PPC film pickup side. Scale bar represents 1 cm.



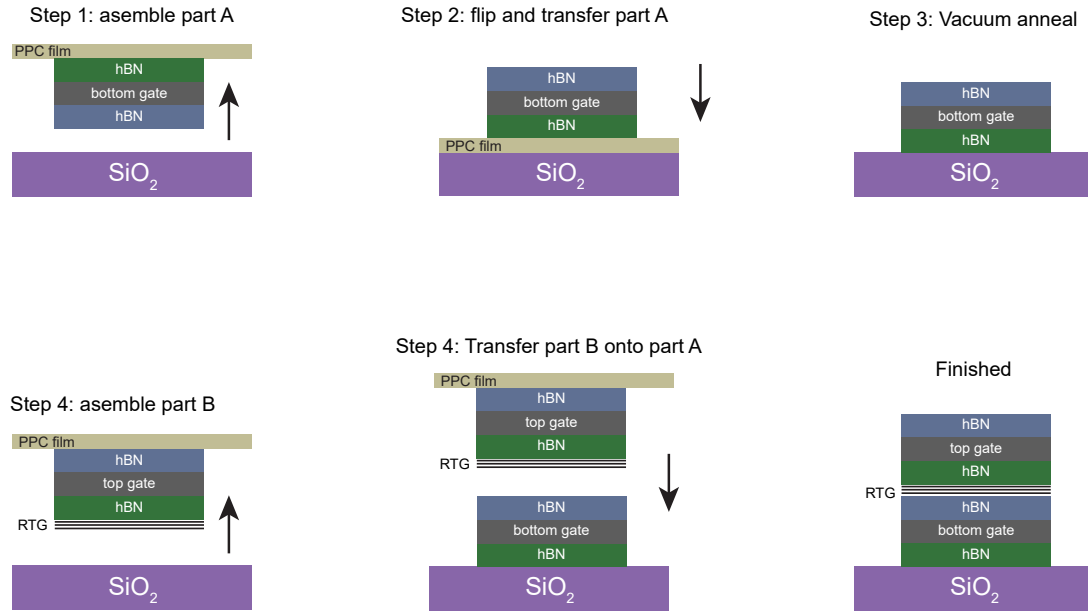


Figure 3.9: Procedure of Van der Waals heterostructure fabrication

second hBN layer, the RTG flake, the third hBN layer, etc. This procedure, while straightforward, is not good for making samples with RTG.

As mentioned before, the ABC-stacked order of trilayer graphene is a metastable state. During the transfer process, shear force will be applied to the materials. The external force will have a chance to convert the RTG to ABA-stacking order even if the ABC-domains are isolated. To increase the rate of success, the mechanical manipulation of the RTG layer need to be minimized. If the heterostructure is assembled from the top layer to the bottom layer, the RTG layer will need to be transferred multiple times to pick up the layer under it. In practice, the ABC- stacking order is almost impossible to survive this process.

To address this problem, we developed a two-step process to assemble the heterostructure. The main idea is to divide the heterostructure into two parts, fabricate them separately and finally assemble the two parts together. The process is schematically shown

in Fig. 3.9.

### **Bottom Part Preparation**

The first step is to assemble the heterostructure below the RTG, which is two hBN layer with a few-layer graphite layer (which eventually become the bottom gate of the device) encapsulated in between. During this process, the surface in direct contact to the PPC film is contaminated while the other side of the stack remains pristine. Since the upper face of this stack will directly touch the RTG, we need to flip the stack upside down to have the pristine surface facing up[88, 89]. This is realized by peeling off the PPC film (together with the tap holding it) from the pickup slide assembly after all the three layers are picked up, then flip the film/stack upside down and deposit onto the substrate. After the film landed, the substrate is heated to 150°C to soften the PPC film, so it is jointed to the substrate. The sample is subsequently annealed at 375°C under vacuum ( $< 10^{-5}$ Torr) for two hours, during which the PPC film will decompose, leaving the hBN/graphite/hBN stack to land onto the substrate. The upper surface remains intrinsic as it does not directly contact with organic solvents or polymers.

### **Top Part Preparation**

The second step is to assemble the upper part of the heterostructure. The stack is assembled following the conventional procedure, which is to subsequently pick up the layers from top to bottom. However, additional effort is needed to prevent the RTG from relaxation.

Firstly, the pickup slide assembly is made with a 3 mm diameter PDMS pads. The large diameter reduces the curvature of the PPC film and therefore reduced the mechanical stress applied to the flakes being picked up. On the other hand, a small curvature increases the difficulty of manipulation. So for general purpose, PDMS pads with 2

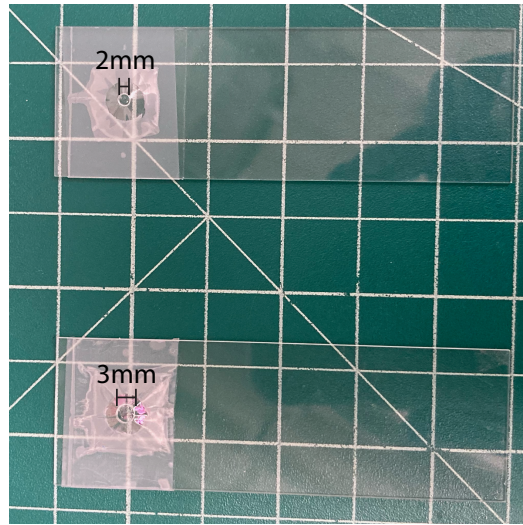


Figure 3.10: PPC pickup slide assembly used for general purpose (top) and for picking up RTG. A large diameter of the PDMS is used for RTG to reduce the curvature of the PPC film and therefore reduce mechanical stress applied on RTG.

mm diameter is ideal for applications when mechanical stress is not a problem. (E.g. fabrication of the bottom part)

Secondly, alignment between the pickup slide and the exfoliated flakes also turns out to be important. When assembling the top part, the hBN layer on the top needs to be large enough to cover the RTG flake. We align the corner of the top hBN with the touchdown center, while aligning the RTG to a region that is close to the touchdown center. In this way, minimum tension is applied to the RTG sample while manipulation of the film by changing the sample's temperature is still possible.

With part A and B fabricated, Part A is transferred onto top B. During the whole process, the RTG flake is only transferred once, this minimized the chance of relaxation.

Even with all the efforts made, the chance for RTG to convert to ABA-stacking order is still considerably high. One potential improvement that can be made is to optimize the direction from which the shear force is applied to the RTG sample during the transfer, which has been studied by a recent work[90]. It is shown that the shear force applied to a

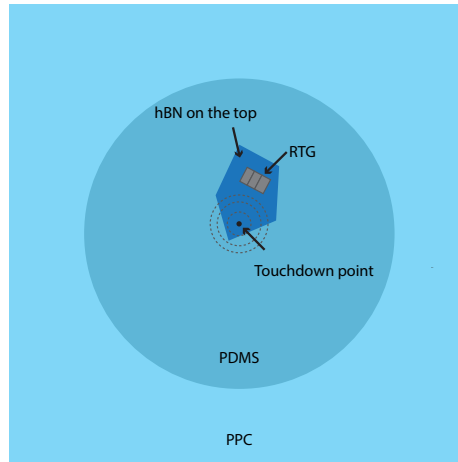


Figure 3.11: Alignment between the heterostructure and the pickup slide.

specific direction will more likely to convert the stacking order. To avoid this, the lattice orientation of the RTG is measured by Raman spectroscopy, and then the pickup slide and the sample is properly aligned so that the shear force is applied from a direction in which the RTG is most stable.

### 3.2.3 Fabrication of the Dual-gated Transistor

With the Van der Waals heterostructure assembled and transferred, the next step is to etch the sample into the proper device geometry and to make electrical contact to the conductive layers for measurement. But before that, it is better to re-check the stacking order of the trilayer graphene flakes. This can be done by taking the Raman spectrum of the encapsulated RTG.

While the presence of hBN does not interfere to the Raman signal from RTG since the spectrum of hBN does not have a peak with similar energy to the 2D-peak of graphene, the few-layer graphite gates does since the spectrum of trilayer graphene and multi-layer graphite is nearly identical. Therefore, the Raman spectrum can only be taken inside regions where the RTG and graphite gates do not overlap. To make this possible, proper

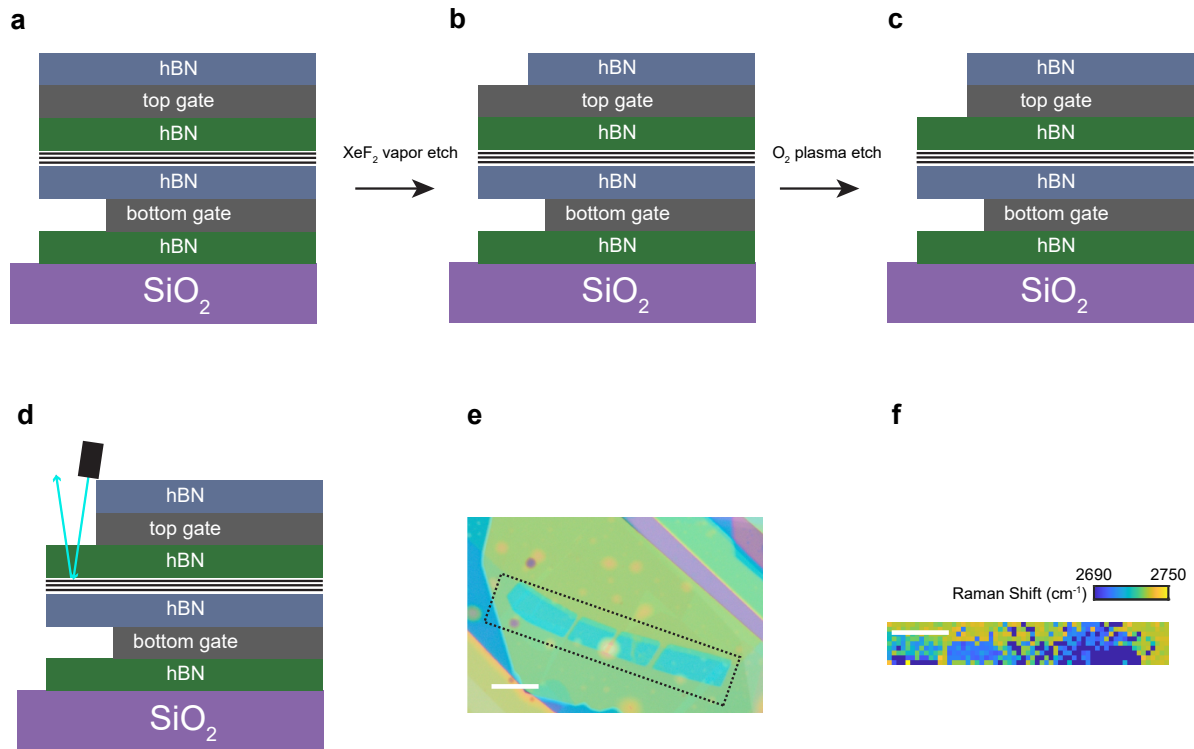


Figure 3.12: Procedure to Measure the Raman spectrum of encapsulated RTG. a, Layout of the heterostructure. Part of the RTG needs to not overlap with the bottom gate. b and c, etch of the top hBN layer and top gate, after which a window is opened where the RTG flake is the only conductive layer. d, Measuring the Raman spectrum through the window. e, optical image of a sample with the etched windows. The boundary box indicates the range in which the Raman spectrum is measured. f. Spatial map of the Raman spectrum of the sample in e.

design of layout of the Van der Waals heterostructure is required.

The layout we used is shown in Fig. 3.12a. The RTG is aligned with the bottom gate so that part of the RTG flake is outside the range of the bottom gate. Although same arrangement can be made for the top gate, it is not necessary since the top layers can be removed by etch process. The top gate is instead usually formed by a graphite flake with large area so that it convert the entire region of RTG. This reduces the complexity of assembling the heterostructure.

In order to measure the Raman spectrum of RTG, part of the top gate needs to

be removed, which can be achieved by xenon difluoride ( $\text{XeF}_2$ ) vapor etch followed by oxygen ( $\text{O}_2$ ) plasma etch, which selectively etches hBN and graphite respectively. After the etch process, a window is opened, allowing measuring Raman spectrum of the trilayer graphene to confirm the stacking order. While the spectrum map can only be done within the range of the etch window, an isolated trilayer graphene flake usually has a uniform (either ABA- and ABC-)stacking order. Therefore, an isolated flake that remains in ABC-stacking order within the etched window usually remains in ABC-stacking order in the entire region. While not accurate, the information obtained from the Raman spectrum significantly speed up the fabrication process.

After the stacking order is confirmed, the sample is etched by inductively coupled plasma of trifluoromethane and oxygen mixture to form the transistor geometry. A metal layer of 3 nm chromium/15 nm palladium/150 nm gold is deposited onto the sample in an electron-beam evaporator to form electrical contact.

During the fabrication process, the masks used for all etch and metal deposition process is polymethyl methacrylate (PMMA) with molecular weight of 950k. The mask is prepared by spin-coat the 8% PMMA solution in anisole at a speed of 4000 rpm, followed by baking the sample at  $180^\circ\text{C}$ , which produces a PMMA layer of around 900 nm thick. For etch process, although thin layers of hard mask such as hydrogen silsesquioxane (HSQ) and aluminum usually gives higher resolution. These materials can generate large surface tension and increase the risk of relaxation of the ABC-stacking order of trilayer graphene.

### 3.3 Electrical Measurement

Two types of measurement were applied to study the electronic properties of RTG. One is to measure the resistance of the samples, or transport measurement. The advan-

tage of transport measurement is its simple instrument setup and minimal perturbation applied to the system. Only a tiny a.c. current (as low as 0.5nA) with low frequency (<50Hz) is driven through the sample and aggressive low pass filtering can be applied to reduce the electron temperature. This allows phenomena with very small energy scale to be detected. The downside of transport measurement is the complex origin of resistance. Transport phenomena are usually complicated and affected by multiple facts. Apart from the intrinsic properties of the system such as density states, other facts such as disorder, size of the sample and edge states may alter the transport sample resistance as well. The complex origin makes it difficult to link the experimentally measured resistance to physical quantities that is directly calculated from theoretical models. Therefore, in addition to resistance measurement, we measure a different quantity, the capacitance between the top and bottom gates, or penetration field capacitance. Unlike the complicated transport phenomena, penetration field capacitance can be linked to theoretical calculated quantities by a simple relation.

$$C_p = \frac{1}{2c_0} \frac{\partial \mu}{\partial n} = \frac{1}{2c_0} \kappa \quad (3.1)$$

where  $\kappa$  is called the inverse electronic compressibility (or "incompressibility" in some literatures). It characterizes how much chemical potential is changed as a unit amount of electronics per area are adiabatically added to the system. In the non-interactive picture,  $\kappa$  is the inverse of density of states at the Fermi surface ( $1/D_F$ ), which can be directly calculated from the theoretical energy band model, as discussed in Chapter 2. In Eq. 3.3, the constant  $c_0$  is the averaged geometric capacitance factor

$$c_0 = \frac{1}{2} (c_T + c_B) \quad (3.2)$$

where  $c_T$  ( $c_B$ ) is the capacitance between the top (bottom) gate and RTG when RTG is treated as ideal metal ( $D_F = \infty$ ).

On the other hand, measuring the penetration capacitance is technically more difficult than resistance. The main reason is that the sample capacitance is much smaller than the capacitance of the instrument (or "parasitic capacitance"). Special technique must be applied to obtain high enough sensitivity. We will discuss the details later but the consequence is it is impossible to maintain low electron temperature while measuring the penetration field capacitance.

To study RTG, we combine both techniques to overcome the drawbacks of them.

### 3.3.1 Transport Measurement

The transport measurement is performed following the conventional technique, in which we apply a four-wire configuration to remove the contact resistance. A Stanford SR860 lock-in amplifier is used as the excitation source and voltmeter. A Stanford SR560 voltage preamplifier is used to preamplify the voltage signal. The frequency range used is from 10Hz to 50Hz, usually chosen based on the noise spectrum so minimized instrumental noise is achieved. Since the sample resistance is quite small, we excite the sample with a constant current. The amplitude varies from 0.5nA to 10nA depending on the purpose of the measurement.

#### Hall Resistance

The geometry of the devices we fabricated have four electrical contacts. All of them are on one side of the sample. This allows conventional measurement of the longitudinal resistance  $R_{xx}$ , which means the direction of the voltage drop detected is parallel to the current flow. This type of measurement is schematically shown in Fig. 3.12 a and b.



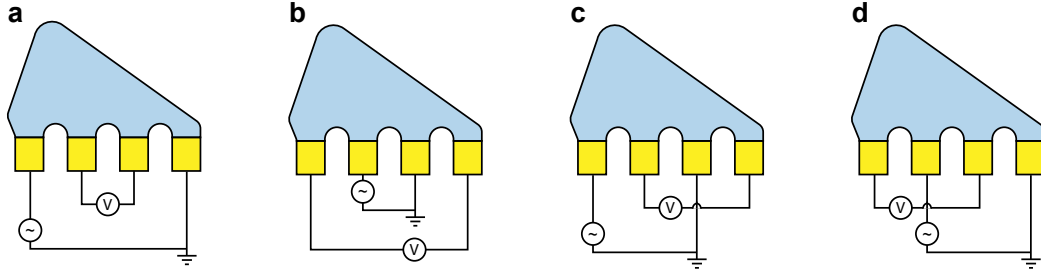


Figure 3.13: Transport measurement configuration. a and b, Measurement of  $R_{xx}$ , c and d, Measurement of  $R_{xy}$ .

However, sometimes we do need to measure the Hall resistance, in which the voltage drop detected is perpendicular to the current flow. The device geometry makes direct measurement of  $R_{xy}$  not possible. To address this problem, we measure the resistance in the two configurations shown in Fig. 3.13c and d (denoted as  $R_{xy}^1$  and  $R_{xy}^2$ ). Based on Onsager relation[91], the difference of the measured resistance is the Hall resistance  $R_{xy}$ .

$$R_{xy} = R_{xy}^1 - R_{xy}^2 \quad (3.3)$$

### Shubnikov de Haals Oscillation

One of the transport measurement techniques we used to study the Fermi surface geometry is Shubnikov de Haals (SdH) Oscillation. In which we measure the longitudinal resistance  $R_{xx}$  as a function of a magnetic field that is perpendicular to the sample ( $B_{\perp}$ ). The magneto resistance will show periodic feature in  $1/B$ . Since the electrons cycle around the Fermi contours, the area  $A$  surrounded by the electron's trajectory can help to determine the shape of the Fermi surface. The area  $A$  is related to the oscillation frequency  $f$  by

$$f = \frac{h}{2\pi e} A \quad (3.4)$$

When a system has a simple Fermi surface, the frequency of resistance oscillation is proportional to the area of the Fermi surface. When complex Fermi surface (such as annular Fermi surface), the oscillation of magneto resistance will be a superposition of multiple harmonic oscillations. Analyzing the oscillation component in frequency space by performing Fourier transform will reveal the Fermi surface geometry. The SdH oscillation is heavily used in this work since the Fermi surface configuration is complex and directly affect the magnetic ordering. The details will be discussed in later chapters.

### 3.3.2 Penetration Field Capacitance Measurement

As mentioned before, the capacitance of the sample is usually orders of magnitude smaller than the parasitic capacitance, making it challenging to detect. To address this problem, we measure the capacitance with an a.c. capacitance bridge circuit with an in-situ amplifier serving as an impedance transformer.

The circuit diagram is shown in Fig. 3.14a. One of the gates of the RTG device is connected to one electrode of a reference capacitor whose capacitance is a constant. Two a.c. voltage with the same frequency and relative phase locked are applied on the other gate of the RTG sample as well as the other electrode of the reference capacitor. (denoted  $\tilde{V}_{\text{ex}}e^{i\phi_{\text{ex}}}$  and  $\tilde{V}_{\text{ref}}e^{i\phi_{\text{ref}}}$  respectively). The voltage between the sample and the reference capacitor (denoted  $\tilde{V}_{\text{b}}$ ) is monitored.

The whole capacitance bridge need to designed into a compact module to load into the cryostat. The module needs to be separated from external wires with large impedance so that the parasitic capacitance is minimized. To realize this, a high electron mobility transistor (HEMT) is mounted close to the sample, so that  $\tilde{V}_0$  can be monitored without introducing low impedance wires to the capacitance bridge. Although the transistor gate still needs to be biased, the bias voltage can be applied through a 100M $\Omega$  resistor to

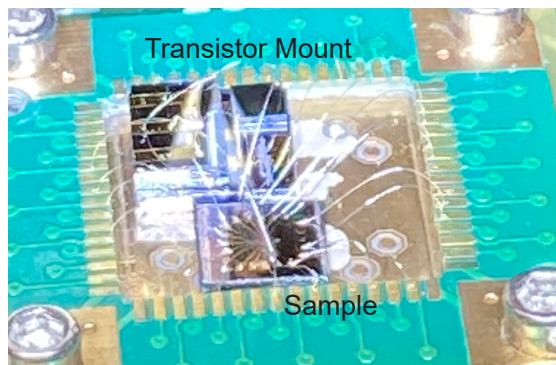
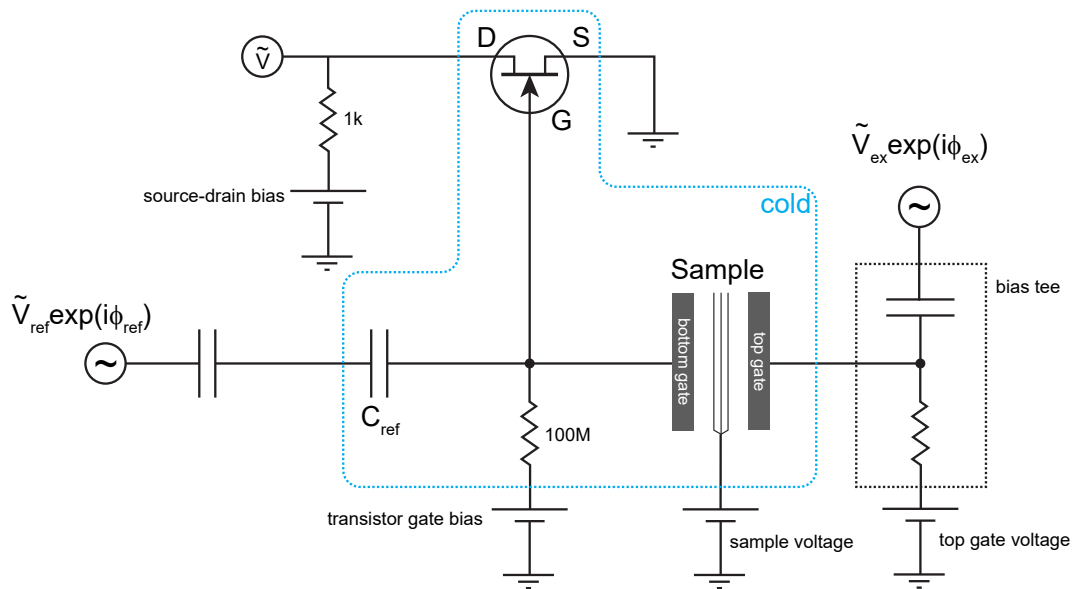


Figure 3.14: Capacitance bridge circuit. a, Circuit diagram. b, actual sample that is loaded into the cryostat.

ensure high impedance. The d.c. level of the top gate can be shifted with a bias tee, so that the d.c. and a.c. voltage can be applied on the gate at the same time. In order to match the impedance, a capacitor with the same capacitance value as the bias tee is connected between the a.c. voltage source and the reference capacitor. A d.c. voltage is also applied on the RTG layer, so that the device can act like a dual-gated transistor without changing the bottom gate voltage (which is fixed to bias the HEMT). In order to drive the HEMT, a source drain bias voltage (50mV to 100mV) is also required. This introduces a source-drain current. This current is usually orders of magnitude larger than the current flowing through the RTG sample and contributes a significant amount of Joule heating, limiting the electron temperature and making it impossible to probe phenomenon that only visible at ultra-low temperature. In the actual measurement, there is no significant change of the sample property when the nominal sample temperature is below 300mK, which indicates the base electron temperature is around 300mK when the transistor is powered up.

To measure the capacitance, the first step is to balance the capacitance bridge, which is done by changing  $\tilde{V}_{\text{ref}}$  and  $\phi_{\text{ref}}$  to zero  $\tilde{V}_0$ . In this case, assume  $\phi_{\text{ex}} = 0$ ,

$$\begin{pmatrix} V_{\text{ref}}^x \\ V_{\text{ref}}^y \end{pmatrix} = \frac{V_{\text{ex}}}{C_{\text{ref}}} \begin{pmatrix} -C_s \\ D_s \end{pmatrix} \quad (3.5)$$

where  $C_s$  is the capacitance of the RTG sample. The impedance of the sample also has resistive component, this is characterized by the "dissipation"  $D_s = 1/(R_s\omega)$ .  $\omega$  is the angular frequency of the a.c. voltage. Eq. 3.3.2 allows calculation of the sample capacitance with  $C_{\text{ref}}$  known.

Balancing the capacitance bridge is a time-consuming procedure. To speed up measurement, the balancing is not performed at every point in the measurement parameter

space. Instead, balancing is only performed at a fixed point and the capacitance at other points are calculated by measuring  $V_0$  and assuming linear response. When off balance,  $V_0$ ,  $\tilde{V}_{\text{ex}}$ ,  $\tilde{V}_{\text{ref}}$  can be linked by a linear transformation

$$\tilde{V}_0 = \mathbf{M}\tilde{V}_{\text{ref}} + \tilde{V}_{\text{offset}} \quad (3.6)$$

where

$$\mathbf{M} = A \begin{pmatrix} \cos \theta & -\sin \theta \\ \sin \theta & \cos \theta \end{pmatrix} \quad (3.7)$$

and

$$\tilde{V}_{\text{offset}} = \tilde{V}_{\text{ex}} \begin{pmatrix} C_s \cos \theta + D_s \sin \theta \\ C_s \sin \theta - D_s \cos \theta \end{pmatrix} \quad (3.8)$$

The parameters  $A$  and  $\theta$  in  $\mathbf{M}$  can be calculated by using the value of  $C_s$  and  $D_s$  in balance. When off balance,  $C_s$  and  $D_s$  can be calculated from Eq. 3.8.

### Convert measured values to $\kappa$

Although the absolute value of  $C_s$  can be obtained from the experiment based on the analysis above and  $\kappa$  is immediately calculated. Two facts prevents this in the actual experiment. First, the accurate determination of  $C_{\text{ref}}$  is impossible. The reference capacitor in the experiment is made by scratching the deposited metal patterns, which is usually a couple of femto farrar. The small capacitance makes it difficult to obtain the accurate value. Second, the capacitance bridge can never be perfectly balanced, this will give an offset that becomes important when the actual change of  $c_s$  is small.

With the above two reasons, the quantity directly measured in the actual experiment is  $M = (C_p + C_{\text{parasitic}})/C_{\text{ref}}$ , where  $C_p$  is the capacitance between the top and bottom gate,  $C_{\text{ref}}$  is the capacitance of the reference capacitor,  $C_{\text{parasitic}}$  is the par-

asitic capacitance of the instrument. The inverse compressibility is related to  $C_p$  by  $C_p = \frac{C_t C_b}{C_t + C_b + \kappa^{-1}} \approx \kappa C_t C_b$  [92], where  $C_{t(b)}$  is the geometric capacitance between the top (bottom) gate and the trilayer graphene. To obtain  $\kappa$ ,  $M$  is measured at two extremes, denoted  $M_\infty$  and  $M_0$ .  $M_\infty$  corresponds to when the trilayer graphene is a good metal, and is achieved by applying a large out-of-plane magnetic field and tuning the Fermi level within a partially filled Landau level.  $M_0$  corresponds to when the trilayer is incompressible, which can be achieved by applying a large displacement field  $D$  while keeping the carrier density  $n_e = 0$ . In the former case  $C_p = 0$ , therefore  $M_\infty = C_{\text{parasitic}}/C_{\text{ref}}$ . In the later case,  $C_p = (M_0 - M_\infty)C_{\text{ref}} = \frac{C_t C_b}{C_t + C_b}$ . From the equations above,  $\kappa = \frac{1}{2C} \frac{M - M_\infty}{M_0 - M_\infty}$ , where the averaged geometric capacitance  $C = (C_t + C_b)/2$  can be obtained by linear fitting of the carrier density  $n_e$ , which is known for fixed Landau level filling providing a calibration standard.

# Chapter 4

## Stoner Ferromagnetism

### 4.1 Overview

In this chapter, we discuss the van Hove singularities induced spontaneous ferromagnetic polarization of the electron system into one or more spin- and valley flavors. By measuring penetration field capacitance on the dual graphite-gated van der Waals heterostructures, we find a cascade of density- and electronic displacement field tuned phase transitions marked by negative electronic compressibility when an electrical displacement field  $D$  (or effectively, an interlayer potential) is applied across the sample, this is experimentally realized by varying the static voltage applied on the two gates. The transitions define the boundaries between phases in which quantum oscillations have either four-fold, two-fold, or one-fold degeneracy, associated with a spin and valley degenerate normal metal, spin-polarized ‘half-metal’, and spin and valley polarized ‘quarter metal’, respectively. For electron doping, the salient features of the data are well captured by a phenomenological Stoner model that includes a valley-anisotropic Hund’s coupling, likely arising from electron-electron interactions at the scale of the graphene lattice. For hole filling, the single particle band structure features a finite-density van Hove singularity,

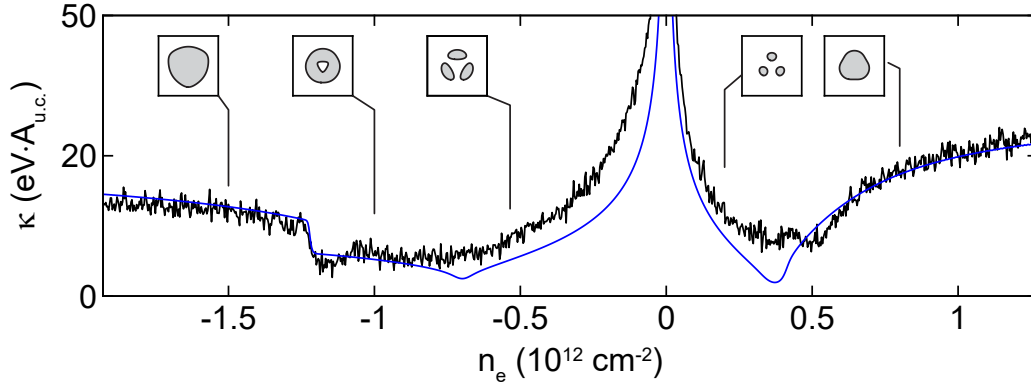


Figure 4.1: Black: inverse compressibility measured at  $D = 0$ . Blue: inverse compressibility calculated from the single particle, six-band continuum model.

and we observe a richer phase diagram featuring a delicate interplay of broken symmetries and transitions in the Fermi surface topology.

Most of the experiment discussed in this chapter is from Zhou, et al, Half and quarter metals in rhombohedral trilayer graphene, arXiv:2104.00653 (2021), although some most recent observations are also discussed.

## 4.2 Inverse compressibility at zero displacement field

Although most of the magnetic phase transitions are observed at finite  $D$ , I would like to discuss the  $D = 0$  case first. In this regime, effects of the electron-electron interaction is not significant and can serve as a good calibration standard to constrict model parameters.

Fig. 4.1 shows the comparison of  $\kappa$  obtained by penetration field capacitance measurement and theoretical calculation from the six-band continuum model. Apart from the peaks at the charge neutrality points, the features at around  $n_e = -1.2 \times 10^{12} \text{cm}^{-2}$  and  $n_e = 0.4 \times 10^{12} \text{cm}^{-2}$  are also predicted by the model, corresponding to the change of Fermi surface topology. The shape of the Fermi contours are schematically shown as



insets.

To further confirm the Fermi surface geometry, we measured the longitudinal magnetoresistance to analyze the Shubnikov de Haas oscillations, which is shown in Fig. 4.2. The original data is shown in panel a. For a fixed density, we perform fast Fourier transform of the  $R_{xx}$  vs  $1/B_{\perp}$  result to analyze the frequency component which is shown in panel b. Here, the y axis is the frequency of  $1/B_{\perp}$  normalized by the total carrier density.

$$f_{\nu} = \frac{f_{1/B}}{n_e h/e} \quad (4.1)$$

For simple Fermi surfaces, the inverse of  $f_{\nu}$  represents the degeneracy of electrons. When the system is heavily doped with electrons and holes, the strongest peak is at  $f_{\nu} = 1/4$ , which is consistent with the four-fold spin- and valley- degeneracy. At low electron/hole density, a peak appears at  $f_{\nu} = 1/12$  instead of  $1/4$ , indicating a twelve-fold degeneracy. The additional three-fold degeneracy comes from the presence of three isolated pockets in the band structure shown in Fig. 2.4 when the Fermi surface is close to the charge neutrality point, sometimes named "gully" in literature.

In both the four-fold and twelve-fold degenerated phases, the oscillations also shows addition peaks at  $f_{\nu}$  that are integer multiples of  $1/4$  and  $1/12$ , which are the harmonics of the base oscillation frequencies, originated from multiple cyclotron motions of the electrons.

Between the hole-doped 4-fold degenerated and 12-fold degenerated regions, there is an intermediate phase where a pair of oscillation is presented and the normalized frequency  $f_{\nu}$  of the oscillations has dependency on the total carrier density  $n_e$ , while the difference of the two frequency is fixed at  $1/4$ . These features indicate the Fermi surfaces has annular geometry, where the high-frequency and low-frequency modes corresponds to the inner and outer Fermi contours. Since the carriers of the inner and outer Fermi

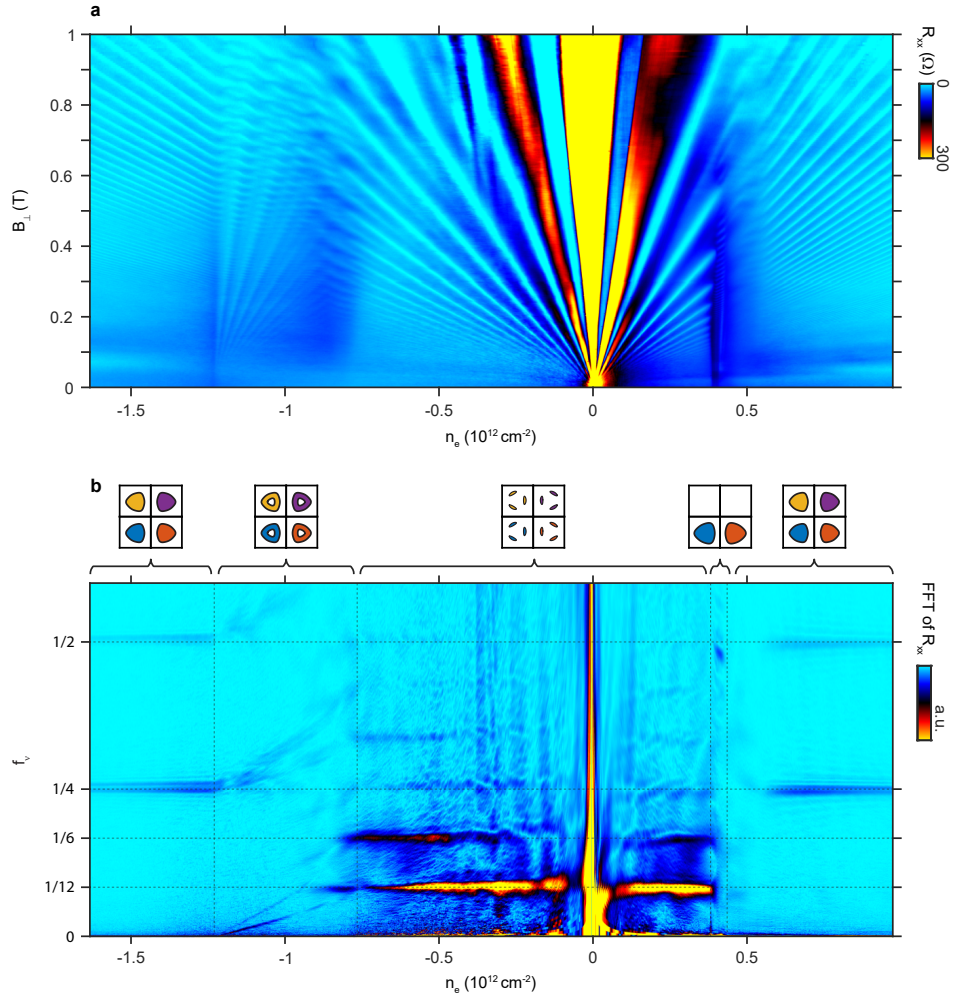


Figure 4.2: Shubnikov de Haas oscillation at  $D = 0$ . a,  $R_{xx}$  vs  $n_e$  and  $B_{\perp}$  measured at  $D = 0$ . b, Fast Fourier transform of data in a, the range of  $B_{\perp}$  chosen is 0.02T to 1T. Data are plotted as a function of  $f_{\nu} = f_B/(\phi_0 n_e)$ , where  $f_B$  is the oscillation frequency (measured in Tesla) and  $\phi_0 = h/e$  is the magnetic flux quantum.  $f_{\nu}$  can be interpreted as the fraction of the total Fermi surface area enclosed by a given orbit. The multiple phases are schematically represented by the Fermi contours on the top.

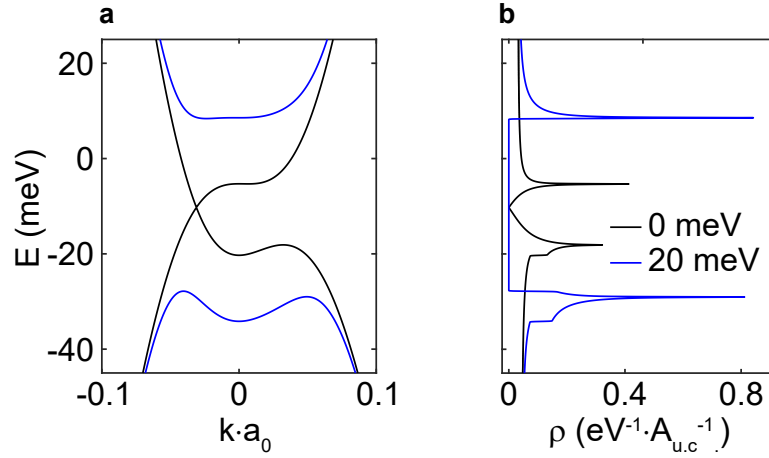


Figure 4.3: a, Band structure of rhombohedral trilayer graphene with an interlayer potential  $\Delta_1 = 0$  (black) and 30 meV (blue) calculated from the six-band continuum model (see S.I.). Here  $a_0 = 0.246$  nm is the graphene lattice constant. b, Corresponding single-particle density of states  $\rho$  versus energy at zero temperature.  $A_{\text{u.c.}}$  is the area of the unit cell.

surfaces are electrons and holes respectively, the difference of the two frequencies represent the normalized total carrier density, which is fixed at  $1/4$ , corresponds to 4-fold spin- and valley-degeneracy, same as the phase at higher density with simple Fermi surface topology. The SdH oscillations give consistent results with the calculation from the continuum model. The results indicate the Coulomb interactions do not dominate the electronic properties at  $D = 0$ .

### 4.3 Displacement field-tuned Magnetic Phase Transition

An important property of RTG is that the energy band structure has significant dependence on the interlayer potential  $\Delta_1$ . This means the band structure can be modulated by applying an electrical displacement field  $D$ . Fig. 4.3 shows the band structure and corresponding density of states of RTG calculated with  $\Delta_1 = 0$  and  $\Delta_1 = 20$  meV respec-

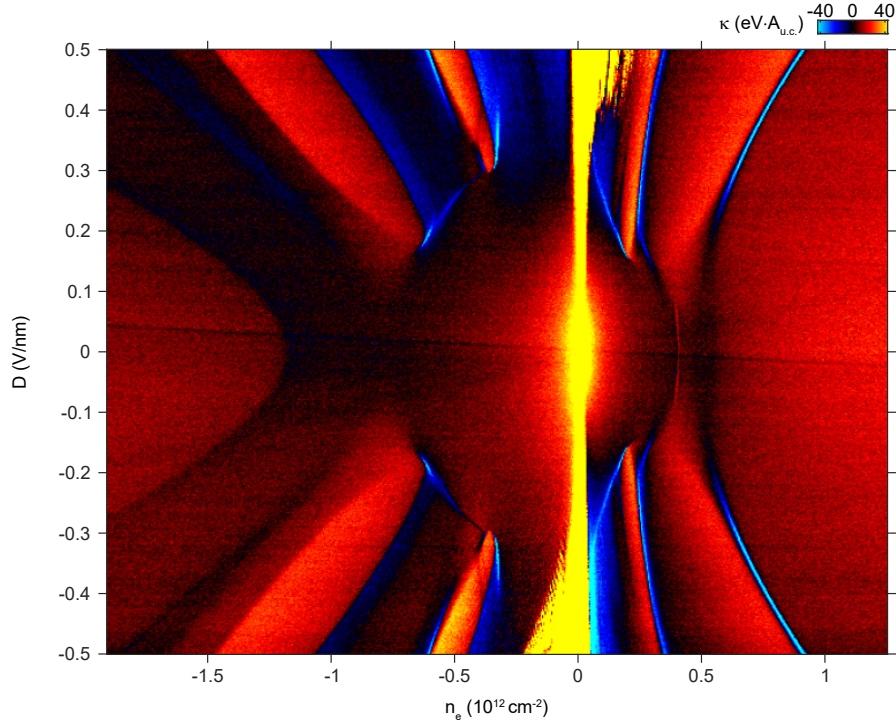


Figure 4.4: False-color plot of the inverse compressibility as a function of displacement field and carrier density.

tively. RTG is a semi metal at  $\Delta_1=0$  and becomes a semiconductor with an energy gap at finite  $\Delta_1$ . Although less significant, the trigonal warping effect, and therefore the Van Hove Singularity, still exist. The density of states profile at  $\Delta_1=20\text{meV}$  shows enhanced peaks at the band top/bottom of the valence/conduction band as shown in Fig. 4.3.

Fig. 4.3 shows the inverse compressibility measured at zero magnetic field and base temperature. At all values of  $D$ , the inverse compressibility has a maximum at charge neutrality, consistent with the Dirac nodes (for  $D = 0$ ) or displacement field induced band gap (for  $|D| > 0$ ) expected from the single particle band structure.

At finite  $D$ , the experimental  $\kappa$  features multiple regions of near constant compressibility separated by boundaries where  $\kappa$  is strongly negative. (See also linecuts in Fig. 4.5.) Negative compressibility is generally associated with electronic correlations[93],

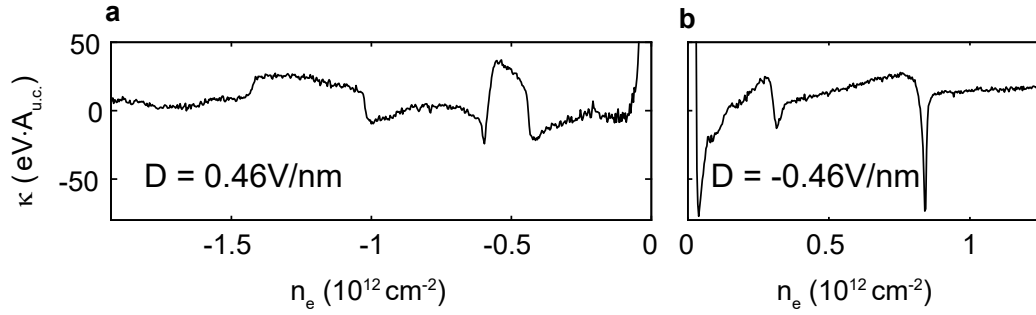


Figure 4.5: Inverse compressibility as a function of displacement field and carrier density at  $D = 0.46 \text{ V/nm}$  (a) and  $-0.46 \text{ V/nm}$  (b).

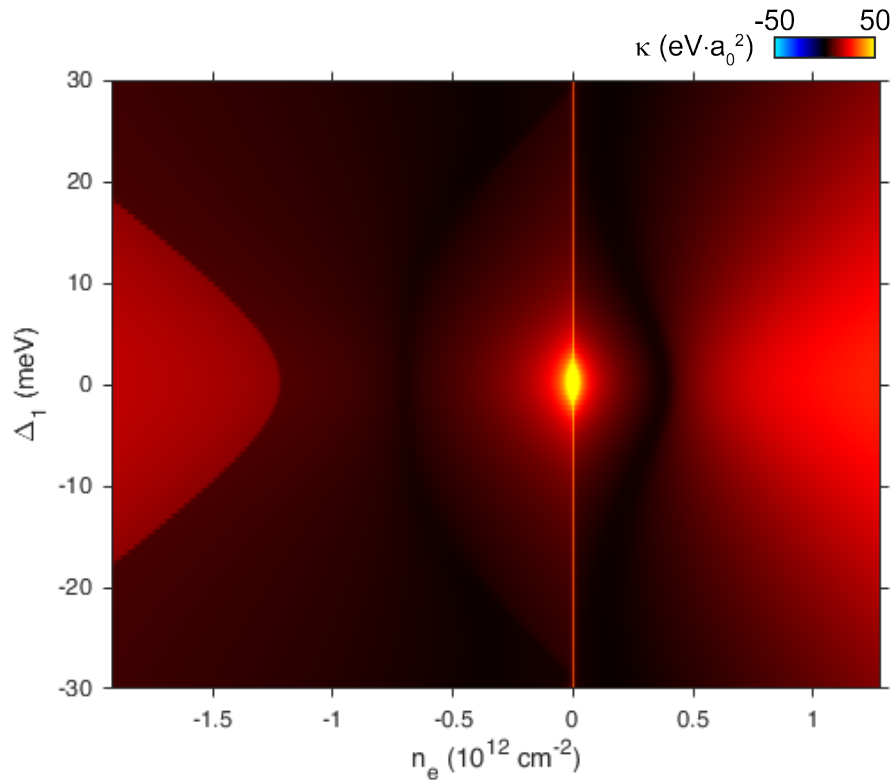


Figure 4.6: False-color plot of the inverse compressibility as a function of displacement field and carrier density calculated from the six-band continuum model.

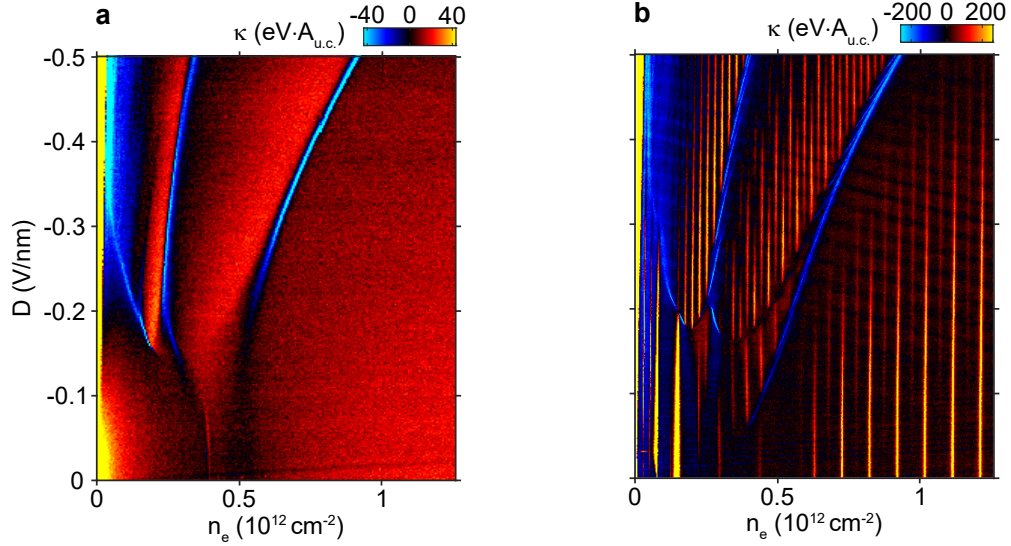


Figure 4.7: False-color plot of the inverse compressibility as a function of displacement field and carrier density for electron doping. a,  $B_{\perp}=0$ . b,  $B_{\perp}=1\text{T}$ .

and may arise at first order phase transitions characterized by phase separation. For electron doping, the high  $|D|$  phase diagram appears to consist of three distinct phases at low, intermediate, and high density separated by first order phase transitions, while for hole doping ( $n_e < 0$ ) the phase diagram is more complex. In both cases, however, negative compressibility features develop at finite  $|D|$  and evolve towards higher  $|n_e|$  with increasing  $|D|$ .

As a comparison, the  $\kappa$  vs  $n_e$  and  $D$  is also calculated from the continuum model, shown in Fig. 4.6. While it matches the experimental data well at  $D = 0$ , the emerged features at finite  $D$  observed in experiment have no correspondence in the calculated results, further prove the interactive nature of those features.

From Fig. 4.4, we can see that  $\kappa$  is invariant with the sign change of  $D$ , which is consistent with the symmetry of the device geometry. On the other hand, the systems exhibits significant particle-hole asymmetry, which is a property that is already reflected by the band structure.(see Fig. 4.3a and Fig. 2.2). We will discuss the phase diagram of

the conduction band first since it is simpler.

Since the phases separated by negative compressibility features are not qualitatively different in the data, we perturb the system with a perpendicular magnetic field and the nature of competing phases is immediately revealed by finite magnetic field measurements, shown for electron doping in Fig. 4.7b for a magnetic field  $B_{\perp} = 1\text{T}$  applied perpendicular to the sample plane. At this field, energy gaps between Landau levels are easily visible as peaks in the inverse compressibility, while the phase boundaries are only slightly altered relative to the zero magnetic field case. As is evident in Fig. 4.7b the phase transitions observed at  $B = 0$  separate regions of contrasting Landau level degeneracy. In the high density phase, the Landau levels have the combined four-fold degeneracy of the spin and valley flavors native to graphene systems; similarly, at low  $n_e$  and low  $D$ , a 12-fold symmetry emerges due to additional degeneracy of local minima in the strongly trigonally warped Fermi surface[94, 70]. However, in the intermediate and low-density phases, respectively, the degeneracy is reduced to two-fold and one-fold. This trend is evident in low-magnetic field magnetoresistance oscillations in the three regimes, Fourier transforms of which are shown in Fig. 4.8. The loss of degeneracy is consistent with a zero magnetic field phase diagram which contains two distinct phases that spontaneously break the combined spin- and valley isospin symmetry. In this picture, the intermediate density phase consists of *two* degenerate Fermi surfaces at  $B_{\perp} = 0$ , constituting a ‘half-metal’ as compared to the normally four-fold degenerate graphene, while the low-density phase has a single Fermi surface and is thus a ‘quarter-metal.’

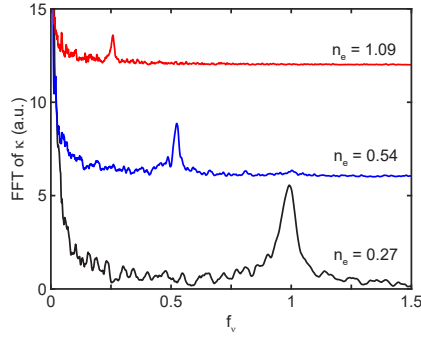


Figure 4.8: Fourier transform of  $R_{xx}(1/B)$  at  $D = -0.43$  V/nm and the indicated values of  $n_e$ , expressed in units of  $\times 10^{12} \text{cm}^{-2}$ . Data are plotted as a function of  $f_\nu = f_B/(\phi_0 n_e)$ , where  $f_B$  is the oscillation frequency (measured in Tesla) and  $\phi_0 = h/e$  is the magnetic flux quantum.  $f_\nu$  can be interpreted as the fraction of the total Fermi surface area enclosed by a given orbit.

## 4.4 Stoner Ferromagnetism

To better understand the mechanisms leading to the rich magnetic phase diagram observed, we study a four-component Stoner model discussed in Chapter 2.

$$E = \sum_{\alpha} E_0(\mu_{\alpha}) + \frac{1}{2}UN \sum_{\alpha \neq \beta} n_{\alpha}n_{\beta} \quad (4.2)$$

Here  $A$ ,  $A_{\text{u.c.}}$  are the area of the sample and unit cell respectively,  $\alpha$  and  $\beta$  index the four spin- and valley flavors, and  $n_{\alpha}$  and  $\mu_{\alpha}$  are the density and chemical potential for a given flavor  $\alpha$ . The first term, with  $E_0(\mu_{\alpha}) = \int_0^{\mu} \epsilon \rho(\epsilon) d\epsilon$ , where  $\rho(\epsilon)$  is a density of states per area, accounts for the kinetic energy, and is minimized by occupying all flavors equally. The second term accounts for the effect of exchange interactions, whose strength is parameterized by a constant energy  $U$  and which we assume to be symmetric within the spin- and valley isospin space. The exchange energy is minimized when fewer flavors are occupied.

The calculation is firstly performed to find a combination of  $n_{\alpha}$  to minimize the total energy (details discussed in Chapter 2, an example is shown in Fig. 4.9a, which is



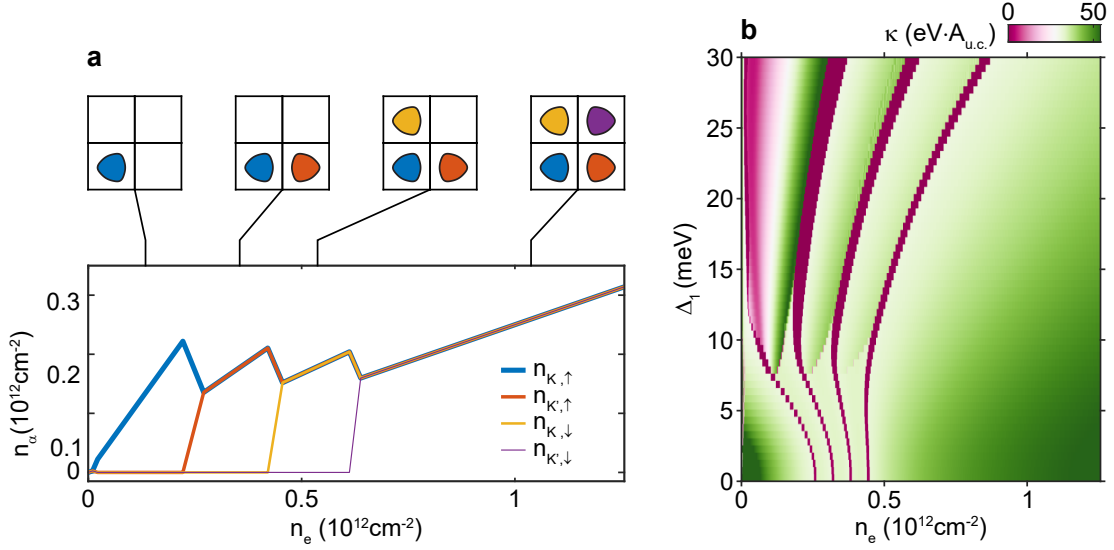


Figure 4.9: Stoner magnetism. a, Partial densities of each spin-valley flavor density calculated from the Stoner model at a fixed interlayer potential of 20 meV. b, Inverse compressibility at  $B = 0$  calculated from the Stoner model described in the main text with  $U = 30$  eV,  $J = -9$  eV. Inset: Same results with  $U = 30$  eV,  $J = 0$ .

calculated with  $\Delta_1=20$  eV.). Then  $\kappa$  is obtained with numerical derivative.

The inverse compressibility calculated within this model (Figure 4.9b) captures several key features of the experimental data. First, the model produces a cascade of symmetry broken phases in which the degeneracy of the Fermi surface is reduced (Fig. 4.9a). Moreover, the phase transitions separating these phases follow trajectories in the  $n_e - D$  plane very similar to those observed experimentally. This dependence can be directly related to the evolution of the band-edge van Hove singularities, which cause the Stoner criterion for ferromagnetism to be satisfied at ever higher  $|n|$  with increasing  $|D|$  as more states accumulate near the band edge.

However, the model deviates significantly from the experimental data, predicting a three-fold degenerate phase that is not observed. The spurious phase can be traced to the artificial  $SU(4)$  symmetry of interactions within these models. More accurately, the internal symmetry group of rhombohedral trilayer graphene consists of  $SU(2)$  spin

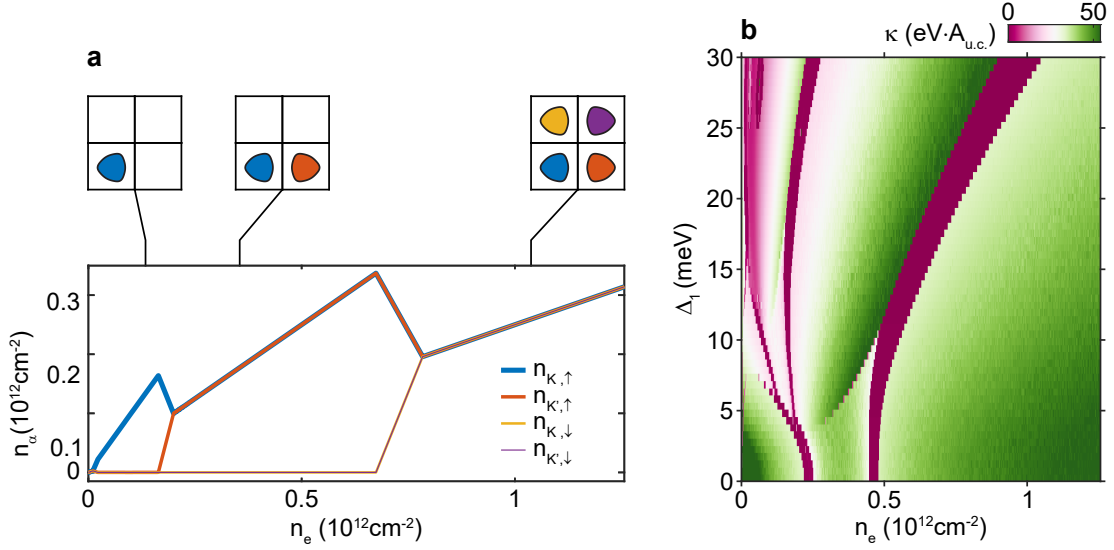


Figure 4.10: Stoner magnetism with anisotropic interaction. a, Partial densities of each spin-valley flavor density calculated from the Stoner model at a fixed interlayer potential of 20 meV. b, Inverse compressibility at  $B = 0$  calculated from the Stoner model described in the main text with  $U = 30$  eV,  $J = -9$  eV.

conservation, charge conservation, time reversal, and the lattice symmetries. Within this lower symmetry group, a variety of interactions that are anisotropic within the spin- and valley-space are allowed, particularly Hund's-type couplings which favor phases with particular broken spin and/or valley symmetries (see S. I.).

This problem has been considered in the context of spontaneous symmetry breaking in graphene quantum Hall ferromagnets[95, 77], taking the form of an intervalley spin exchange coupling that favors the formation of a canted antiferromagnetic state at charge neutrality. Motivated by this observation, we introduce a flavor anisotropy of the form

$$\Phi'/A = JA_{\text{u.c.}} (n_{K\uparrow} - n_{K\downarrow}) (n_{K'\uparrow} - n_{K'\downarrow}). \quad (4.3)$$

which is an example of Eq. 2.3. For  $J > 0$ , this term favors opposite spin polarization in the two valleys, as is thought to occur in graphene quantum Hall ferromagnets, while

for  $J < 0$  this term corresponds to a Hund's coupling and favors valley unpolarized, spin ferromagnetic ground states. The phase diagram including this term—which is independent of the sign of  $J$ , is shown in Fig. 4.10 for  $U = 30$  eV, with  $|J|/U = 0.3$ .

To constrain the precise broken symmetries in the half- and quarter-metal phases, we study the evolution of the phase transitions in an in-plane magnetic field, which couples primarily to the electron spin through the Zeeman effect. The resulting change in density at which a given transition occurs is directly proportional to the difference in Zeeman energy between the two competing phases, making tilted fields a sensitive probe of relative spin polarization. As shown in Fig. 4.11a, Zeeman energy favors the half-metal over the fully symmetric—and necessarily spin unpolarized—state. Moreover, the phase transition density shows a cusp at  $B_{\parallel} = 0$ , implying an energy difference that is linear in  $B_{\parallel}$  as expected for a ferromagnetic half metal with a divergent spin susceptibility at  $B = 0$ . In contrast, the transition between half- and quarter metal is unaffected by  $B_{\parallel}$  as expected for identical—and presumably full—spin polarization in both phases. Measurements of the Hall effect (Figs. 4.11b) show anomalous Hall effect in the quarter-metal phase but no corresponding effect in the half-metal. This is expected due to the contrasting Berry curvatures in the two valleys, which cancel for valley unpolarized states but may give rise to an intrinsic anomalous Hall effect for valley polarized states[96]. Taken together, we conclude that the quarter metal is spin- and valley polarized while the half-metal is spin polarized but valley unpolarized. Interestingly, this implies a ferromagnetic Hund's coupling ( $J < 0$ ), in contrast to the quantum Hall ferromagnet in mono- and bilayer-graphene[97].

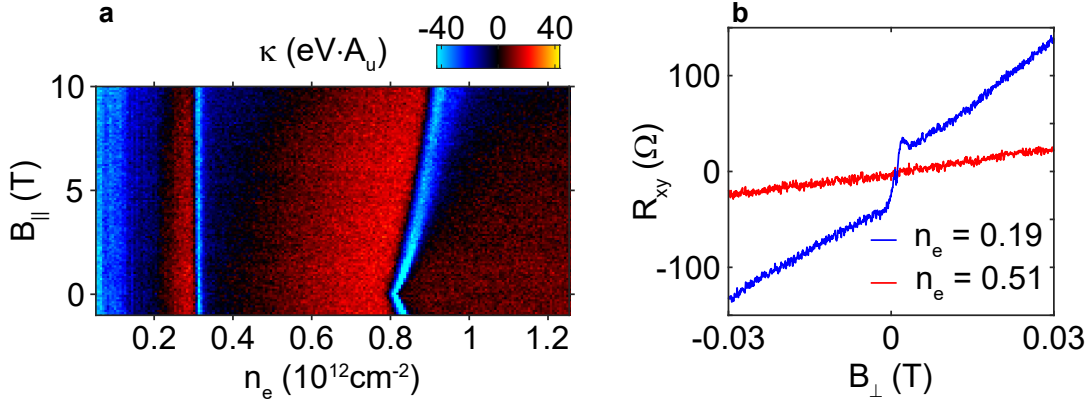


Figure 4.11: Order of symmetry breaking. a, Partial densities of each spin-valley flavor density calculated from the Stoner model at a fixed interlayer potential of 20 meV. b, Inverse compressibility at  $B = 0$  calculated from the Stoner model described in the main text with  $U = 30$  eV,  $J = -9$  eV.

## 4.5 Ferromagnetism and Fermi surface topology in the valence band

As compared to electron doping, hole-doped rhombohedral trilayer shows a considerably more complex phase diagram, as is seen in the  $B_{\perp} = 1$  T magneto capacitance data shown in Fig. 4.12b. The contrast between the phase diagrams of the valence and conduction bands can be related to the single particle band structure, which differs markedly between the two. Most importantly, in the valence band the density of states diverges at a finite density  $n_e^* \approx -5 \times 10^{11} \text{cm}^{-2}$ , which corresponds to the merger of three disjoint Fermi pockets at low hole density into a single annular Fermi surface. At still higher  $|n_e|$ , the small electron pocket centered at each corner of the Brillouin zone disappears, leading to a step discontinuity (see Fig. 4.1b). As a result, density-driven phase transitions in the valence band may be of several general types. First, as in the conduction band isospin symmetries may break, reducing the degeneracy of the Fermi surface. In addition, Lifshitz transitions in the topology of the Fermi surface, which are already evident

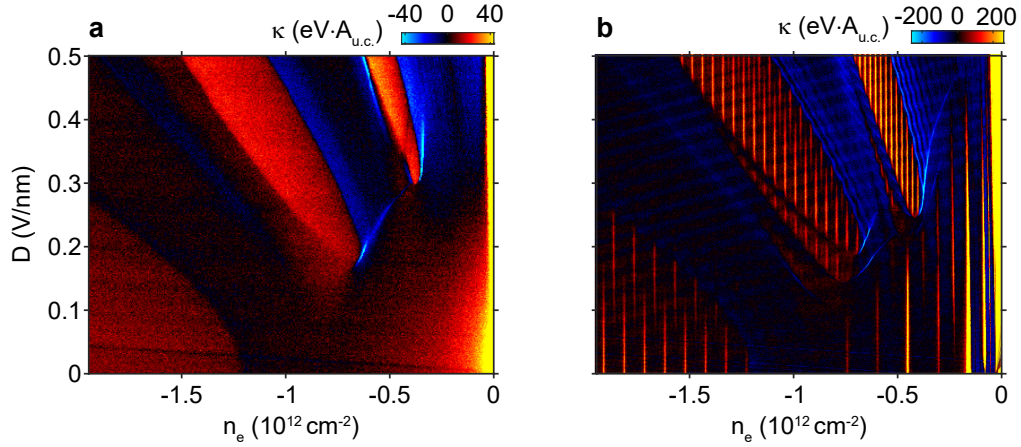


Figure 4.12: False-color plot of the inverse compressibility as a function of displacement field and carrier density for hole doping. a,  $B_{\perp}=0$ . b,  $B_{\perp}=1\text{T}$ .

in the single particle band structure, may occur. Finally, the nonmonotonic dependence of density of states on  $n_e$  may favor states with partial isospin polarization, analogous to conventional ferromagnets, and allowing for Lifshitz transitions of a second type in which new Fermi surfaces are nucleated in previously unoccupied spin/valley flavors.

To disentangle these phases experimentally, we measure the resistivity as a function of perpendicular magnetic field and  $n_e$  and plot the Fourier transform of  $R_{xx}(1/B)$  in Figs. 4.13 with frequencies normalized to that corresponding to the total carrier density. Peak position thus indicates the fractional share of the total electrons enclosed by a given Fermi contour. At the highest values of  $|n_e|$ , a single peak (and its harmonics) is visible at  $f_{\nu} = 1/4$ , consistent with four Fermi surfaces each enclosing an equal share of the total density. As  $n_e$  crosses the threshold of  $n_e \approx 1.7 \times 10^{12} \text{ cm}^{-2}$  in Fig. 4.13c (corresponding to the step in compressibility highlighted in Figs. 4.1) the frequency of the quarter-density peak begins to grow, and a second peak emerges at low frequency. We interpret this as indicating a Lifshitz transition where a small electron Fermi surface is nucleated in the middle of the (now annular) Fermi sea, precisely as predicted by the single particle band structure.

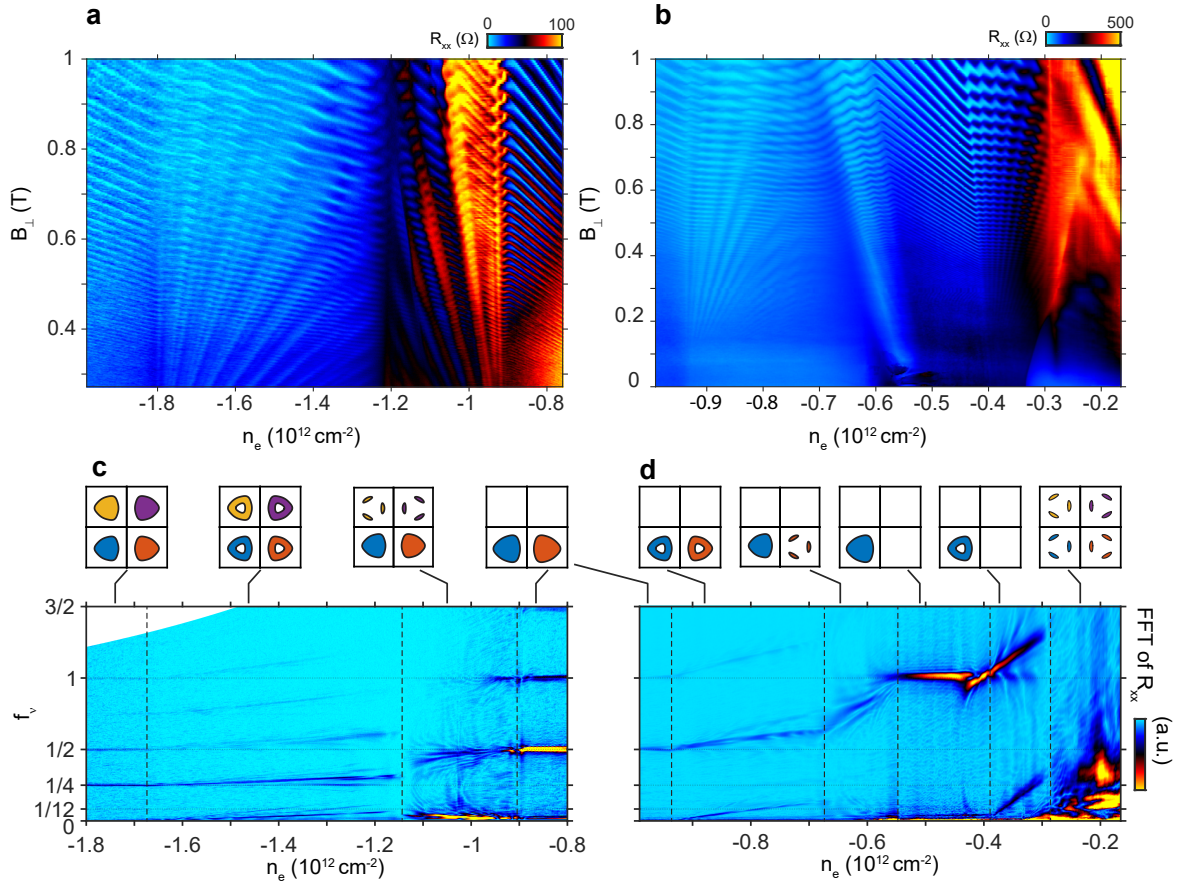


Figure 4.13: SdH oscillation at hole doping. a and b  $R_{xx}$  vs  $n_e$  and  $B_{\perp}$  at  $D = 0.23 \text{ V/nm}$  and  $D = 0.40 \text{ V/nm}$  respectively. c, Fourier transform of quantum oscillations in resistivity measured at  $D = 0.23 \text{ V/nm}$ . Panels on the top show schematic Fermi contours in density domains distinguished by their quantum oscillations. d, As in panel c, but for  $D = 0.40 \text{ V/nm}$ .

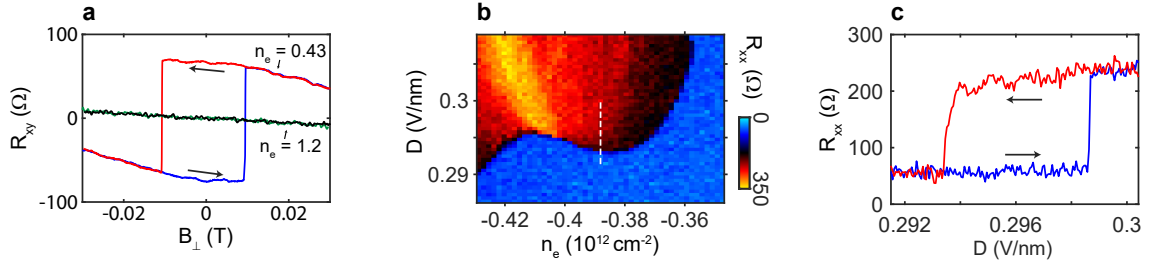


Figure 4.14: Hysteretic transport. a, Low magnetic field Hall resistivity measured at  $D = 0.43\text{V/nm}$  at two values of  $n_e$ . Hysteretic anomalous Hall effect is observed in the valley-polarized quarter metal, but not in the valley unpolarized half metal. b, Detail of the phase boundary between the quarter metal and symmetric low-density state. c, Resistivity measured as a function of  $D$  across this boundary. The transition is strongly first order, showing hysteresis as a function of applied gate voltages.

Upon further lowering of  $|n_e|$  towards zero, a sudden transition in the quantum oscillations is observed near  $n_e \approx -1.15 \times 10^{-12}$  in Fig. 4.13c. This threshold corresponds to a subtle but visible low  $\kappa$  feature in Fig. 4.1. On the low  $|n_e|$  side of the transition, the oscillation frequencies are less well-defined, but show spectral weight concentrated most prominently at  $f_\nu$  slightly less than 0.5 and at very low frequencies. These features are consistent with a Stoner-type transition to a partial isospin polarized (PIP) phase, with majority and minority charge carriers in two distinct pairs of isospin flavors. These contours continuously evolve until the  $f_\nu$  of the high frequency peak converges to 1/2, whereupon the low frequency peak disappears, consistent with a Lifshitz transition from the PIP phase into a half-metal. Remarkably, this pattern repeats itself as the density is lowered further, as shown in Fig. 4.13d: the simple half-metal transitions into an half-metal with an annular Fermi sea, then to a PIP phase with one majority and one minority flavor, then into a simple quarter metal and then into an annular quarter metal before isospin symmetry is restored at the lowest densities. At these very low densities, each isospin flavor hosts three Fermi pockets, leading to observed oscillation frequencies near  $f_\nu = 1/12$ .

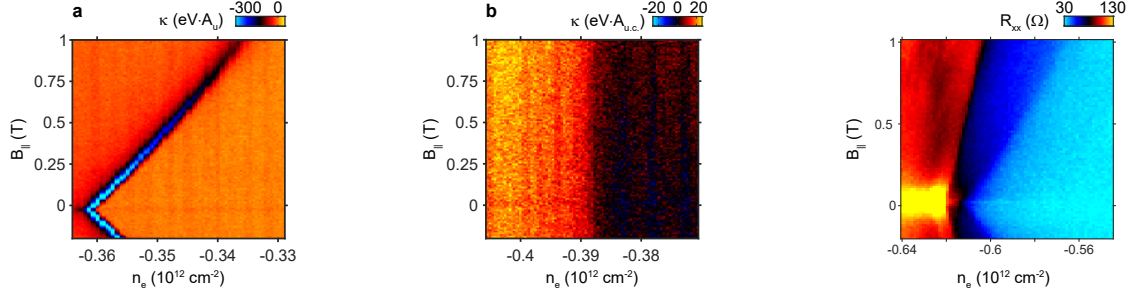


Figure 4.15: In-plane magnetic field dependence of the phase boundaries. a,  $\kappa$  vs  $n_e$  and  $B_{\parallel}$  at  $D = 0.37\text{V/nm}$ , which covers the phase boundary between a 4-fold degenerate phase and a 1-fold degenerate phase. b, Same as a, measured at  $D = 0.33\text{V/nm}$ , which covers a phase boundary between a 1-fold degenerate phase with a simple Fermi surface and a 1-fold degenerate phase with annular Fermi surface. c,  $R_{xx}$  vs  $n_e$  and  $B_{\parallel}$  at  $D = 0.37\text{V/nm}$ , which covers a phase boundary between a 4-fold degenerate phase and a 2-fold degenerate phase.

As for the electron side, many of these transitions show characteristic  $B_{\parallel}$ -dependence (Fig. 4.15)) that allow us to confirm the spin- and valley-polarizations of the half- and quarter-metal states, which we find to be similar to those on the electron side. We note, however, that transitions involving the PIP phases do not generally show simple linear-in- $B_{\parallel}$  behavior; combined with the complexity of the finite  $B_{\perp}$  magnetoresistance suggests that these domains may harbor multiple PIP phases.

## 4.6 Phase transition in the 1x phase at hole doping

As mentioned in the previous section, the complexity of the phase diagram at hole doping can originate from the complicated Fermi surface and the presence of PIP phases. However, even for phases with simple and identical Fermi surfaces, the spin- and valley can still form different ordering. This is the case for the hole-doped phase where both spin- and valley- degeneracy are lifted, and the Fermi surface is circular.

Fig. 4.16 shows the inverse compressibility near the "simple" 1x phase. With an 1T out-of-plane magnetic field applied (Fig. 4.12), this region shows no spin- and valley



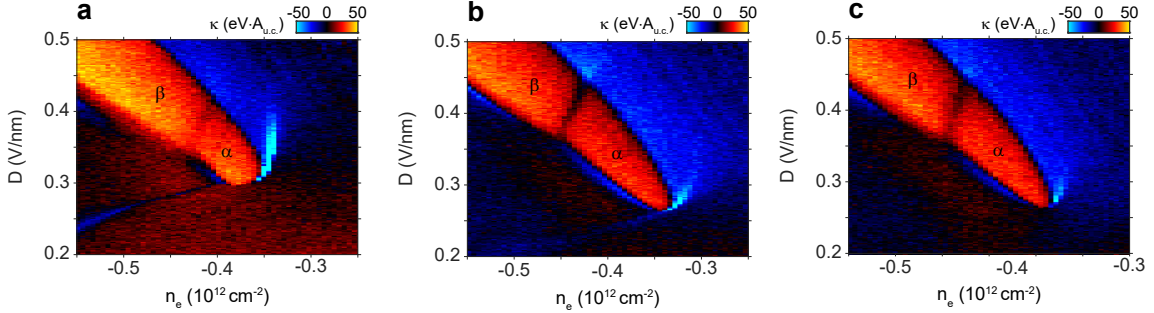


Figure 4.16: False-color plot of the inverse compressibility as a function of displacement field and carrier density for hole doping near the spin- and valley- symmetry broken phase. a,  $B_{\parallel}=0$ . b,  $B_{\parallel}=3\text{T}$ . c,  $B_{\parallel}=12\text{T}$ .

degeneracy, therefore the naive assumption would be that the entire region is spin- and valley-polarized state. However, as shown in Fig. 4.16, this region has actually two separated phases, which we named "α-phase" and "β-phase" respectively. The phase boundary is blurry but distinguishable, and become sharp with an in-plane magnetic field applied.

From (ref), with both spin- and valley- symmetry broken, there are three possible phases: the spin- and valley- polarized phase (an example is  $\langle K, \uparrow \rangle$ ), the spin-polarized intervalley coherent phase (an example is  $\langle K, \uparrow \rangle + e^{i\theta} \langle K', \uparrow \rangle$ ), and the spin valley-locked intervalley coherent phase (an example is  $\langle K, \uparrow \rangle + e^{i\theta} \langle K', \downarrow \rangle$ ). For the above three phases, only the first one is valley-polarized, and only the last one is spin-unpolarized. The α- and β-phase is probably two of them.

The signature of valley-polarization is anomalous Hall effect and magneto hysteresis as no long-range magnetic ordering is possible for spin-polarized phases in the absence of spin-orbit interaction. Therefore, we measured the Hall resistance across the two phases, shown in Fig. 4.16. The β-phase shows a typical anomalous Hall effect with hysteresis. This immediately reveal the nature of the β-phase: a spin- and valley- polarized state, similar to the 1x phase at electron doping. Contrary to the β-phase, the α-phase does not show an obvious anomalous Hall effect or magneto hysteresis, although the response

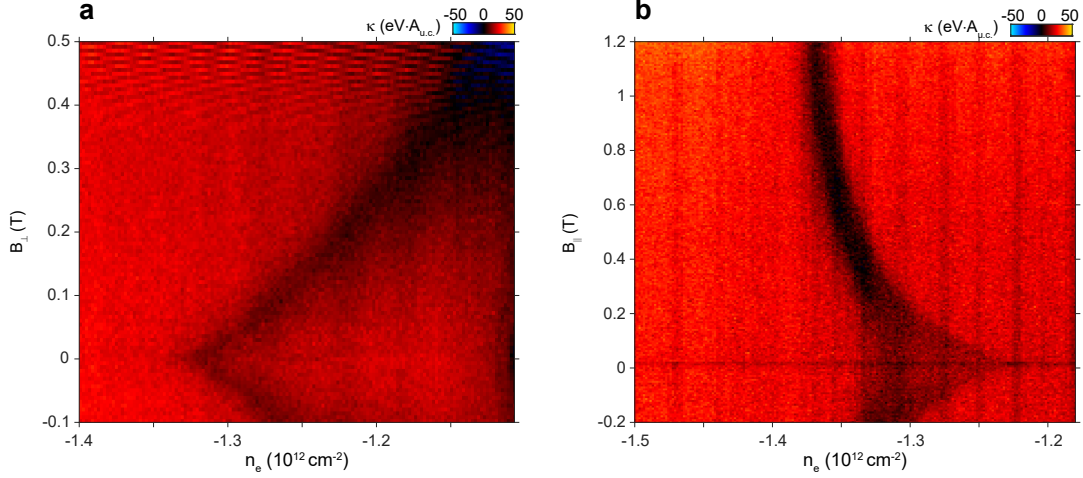


Figure 4.17: False-color plot of the inverse compressibility as a function of displacement field and carrier density for hole doping near the spin- and valley- symmetry broken phase. a,  $B_{\parallel}=0$ . b,  $B_{\parallel}=3\text{T}$ . c,  $B_{\parallel}=12\text{T}$ .

of the Hall resistance to magnetic field still deviates from the norm Hall effect. The non-linear response is similar to multi-band system, where electrons from more than one band contribute to the Hall resistance.

The result from measurement of Hall effect shows that the  $\beta$ -phase is spin- and valley-polarized, while the  $\alpha$ -phase belongs to one of the other two phases, where the valley-degree of freedom forms inter-valley coherent state. This is also consistent with the magneto-resistance measurements result shown in Fig. 4.17a. A valley-polarized phase has finite orbital magnetic moment and therefore favored by out-of-plane magnetic field.

On the other hand, Fig. 4.17b shows that an in-plane magnetic field favors the  $\alpha$ -phase. Since the  $\beta$ -phase has already the largest possible spin-polarization. The response to in-plane magnetic field can only be an orbital effect. In multilayer graphene system, the interlayer hopping allows circular motion of electrons perpendicular to the sample plane. This cyclotron motion will generate a magnetic moment that is parallel to the sample

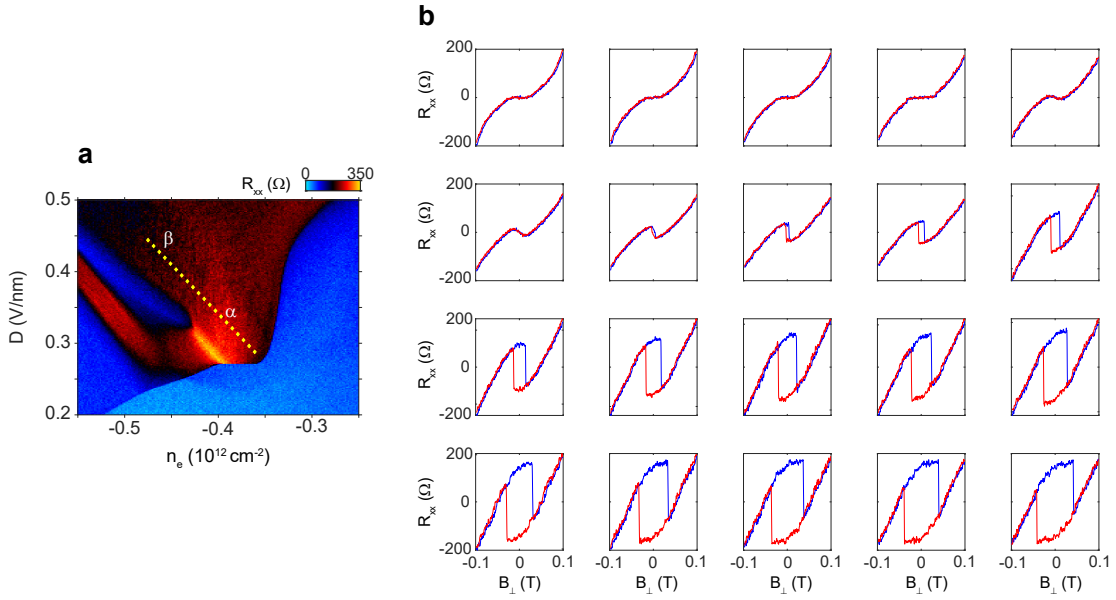


Figure 4.18: Hall effect in the 1x phase at hole doping. a, Longitudinal resistance measured as a function of  $n_e$  and  $D$  near the simple 1x phase. b, Anomalous Hall effect measured across the  $\alpha$ - and  $\beta$ -phase transition. From top to bottom, from left to right, the corresponding value of  $n_e$  and  $D$  are labeled in panel a.

plane. Given that this effect is usually smaller or comparable to the Zeeman effect. The  $\alpha$ -phase is more likely to be a spin-polarized intervalley coherent state. Both the  $\alpha$ - and  $\beta$ - phases are spin-polarized, but the intervalley coherent state has a larger in-plane orbital magnetic moment and therefore favored by a large in-plane magnetic field.

Puzzle still remains for the nature of the two phases. On the one hand, the mechanism for an intervalley coherent state to gain more in-plane magnetic moment compared to a valley-polarized phase is not obvious. On the other hand, the classification of spin-valley- nondegenerated state into three phases is only accurate when the Fermi surface is within an energy gap. For metallic state, there are more flexibility for electrons to occupy specific states in the momentum space to, for example, maximize orbital magnetization. These phenomena are beyond Stoner's theory.

## 4.7 Hartree-Fock model

*The content of this section is from Zhou, H et al, Half and quarter metals in rhombohedral trilayer graphene, arXiv:2104.00653 (2021). The content is mainly contributed by Tobias Holder and Erez Berg.*

To test the robustness of the results obtained from the simple Stoner model, we perform a more detailed Hartree-Fock analysis of the cascade of spin and valley symmetry-breaking transitions as a function of density. We begin with the Hamiltonian  $H_0$  in Eq. 4.7, and add to it a screened Coulomb interaction

$$H_c = \frac{1}{2} \sum_{\alpha, \beta, i, j} \int d^2r d^2r' U(|\mathbf{r} - \mathbf{r}'|) \psi_{i\alpha}^\dagger(\mathbf{r}) \psi_{j\beta}^\dagger(\mathbf{r}') \psi_{\beta j}(\mathbf{r}') \psi_{i\alpha}(\mathbf{r}), \quad (4.4)$$

where  $\alpha, \beta = 1, \dots, 4$  runs over the spin and valley indices,  $i, j = 1, \dots, 6$  label the two sublattices and three layers (this is the six-dimensional space in which  $H_0$  is written), and  $\psi_{j\alpha}^\dagger(\mathbf{r})$  creates an electron at position  $\mathbf{r}$ , sublattice/layer  $j$ , and spin/valley  $\alpha$ . The interaction is taken to be  $U(r) = \int \frac{d^2q}{(2\pi)^2} U(q) e^{i\mathbf{q}\cdot\mathbf{r}}$ , where

$$U(q) = \frac{2\pi e^2 \tanh qd}{\epsilon q}, \quad (4.5)$$

corresponding to screening by two symmetric metallic gates at a distance  $d$  above and below the system ( $\epsilon$  is an effective dielectric constant, which includes the HBN and the screening from the remote bands of the trilayer graphene).

The screened Coulomb potential is assumed to depend only on the local density of electrons, and does not depend on any of the internal indices (such as spin and valley). This type of interaction is expected to dominate when the average distance between charge carriers is much larger than the inter-atomic spacing, as is always the case in our system. Later, we will include phenomenologically the effects of short-distance interac-

tions that may depend on the spin and valley indices.

We treat the Hamiltonian  $H = H_0 + H_c$  within the Hartree-Fock approximation. To this end, we use a variational quadratic Hamiltonian  $H_{\text{var}}$  to generate a variational state, and minimize the variational free energy over the parameters of  $H_{\text{var}}$ . In order to simplify the calculation, we restrict the variational state in several ways: 1. All the bands away from the Fermi level are “frozen”, i.e., we do not allow the variational Hamiltonian to mix the active (partially filled) band with the completely filled or completely empty bands; 2. We allow only states that preserve the separate spin and valley conservation symmetries of the Hamiltonian. The first simplification is justified as long as the remote bands are separated from the active band by a sufficiently large gap. Most crucially, it requires the displacement field to be sufficiently large compared to the magnitude of the Coulomb interaction. The second simplification omits the possibility of states that break the valley conservation symmetry spontaneously by occupying states that are coherent superposition of the two valleys. We leave the study of such states to future theoretical work.

The blue curves in Fig. 4.19 show representative results for the variational Hartree-Fock free energy per electron as a function of the electronic density of different types of spin- and valley-polarized states, measured relative to the symmetric state (where all the spin and valley flavors are populated equally). As in the Stoner model, the states labelled by  $l = 1, 2, 3$  are states in which  $l$  spin or valley flavors are populated, and the other  $4 - l$  flavors are empty. The results are qualitatively similar to those of the Stoner model, in that the system undergoes a cascade of first-order transitions upon increasing the density from the charge neutrality point, according to the sequence (1,2,3,4). Qualitatively similar results are also obtained for other values of the displacement field  $\Delta_1$  and for a hole-doped system.

In order to match the experiment, where the  $l = 3$  state is not observed, we need to

consider interaction terms beyond the long-range Coulomb interaction [Eq. (4.4)] which is SU(4) symmetric in spin and valley space. Interactions at ranges of the order of a few lattice constants (either Coulomb or phonon-mediated) can depend on the spin and valley indices of the electrons. We model these short-range terms as

$$H_A = \frac{\tilde{U}}{2} \int d^2r : (n_K + n_{K'})^2 : + \frac{\tilde{V}}{2} \int d^2r : (n_K - n_{K'})^2 : + \tilde{J} \int d^2r : \boldsymbol{\sigma}_K \cdot \boldsymbol{\sigma}_{K'} :, \quad (4.6)$$

where  $n_K(\mathbf{r})$  and  $n_{K'}(\mathbf{r})$  are the local densities of electrons in the two valleys. The operators  $\boldsymbol{\sigma}_K(\mathbf{r})$ ,  $\boldsymbol{\sigma}_{K'}(\mathbf{r})$  are the local spin densities, defined as  $\boldsymbol{\sigma}_K(\mathbf{r}) = \sum_{s_1, s_2} \psi_{Ks_1}^\dagger(\mathbf{r}) \boldsymbol{\sigma}_{s_1, s_2} \psi_{Ks_2}(\mathbf{r})$  (and similarly for  $\boldsymbol{\sigma}_{K'}$ ), where  $\boldsymbol{\sigma}_{s, s'}$  are Pauli matrices acting in spin space, and  $\psi_{Ks}^\dagger$  is the creation operator for electrons at valley  $K$  and spin  $s = \uparrow, \downarrow$  in the active band that crosses the Fermi level (which we project to in our calculation). Normal ordering of an operator  $\hat{O}$  is denoted by  $:\hat{O}:$ . The  $\tilde{U}$  term is a local spin and valley-isotropic interaction,  $\tilde{V}$  parameterizes the difference in the local interaction strength between electrons of the same valley and electrons in different valleys, and the  $\tilde{J}$  term is a spin-exchange Hund's rule coupling between electrons of different valleys. Eq. (4.6) is the most general contact (zero-range) interaction term between electrons in the active band, which is compatible with all the symmetries of the problem.

Our parameterization of the short-range interactions is related to that used by Kharitonov [77] in modeling the spin and valley polarization of electrons in the zero Landau levels in graphene,

$$H_A = \int d^2r \left[ \frac{u_z}{2} : (\psi^\dagger \tau^z \psi) (\psi^\dagger \tau^z \psi) : + u_\perp : (\psi^\dagger \tau^+ \psi) (\psi^\dagger \tau^- \psi) : + H.c. \right], \quad (4.7)$$

where  $\tau$  are Pauli matrices that act in valley space and  $\psi^\dagger = (\psi_{K\uparrow}^\dagger, \psi_{K\downarrow}^\dagger, \psi_{K'\uparrow}^\dagger, \psi_{K'\downarrow}^\dagger)$ , by the following relations:  $\tilde{U} = -\frac{u_\perp}{4}$ ,  $\tilde{V} = u_z - \frac{u_\perp}{4}$ ,  $\tilde{J} = -\frac{u_\perp}{2}$ .

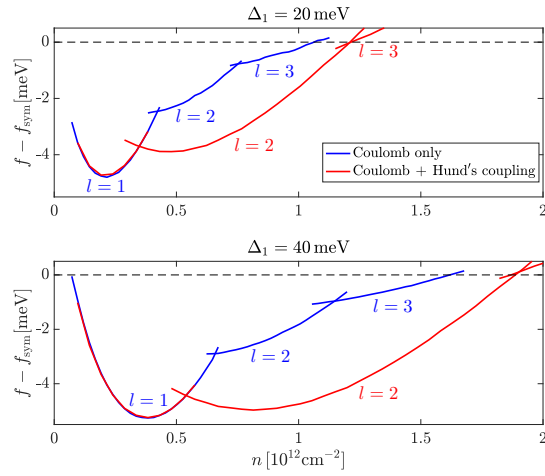


Figure 4.19: Free energy  $f$  per electron as a function of electron density, measured relative to that of a spin and valley-symmetric state,  $f_{\text{sym}}$ . The blue curve shows the result of a calculation with only a long-range, spin and valley-symmetric screened Coulomb interaction (Eq. (4.4)). The red curve was obtained by including also an interaction of the form (4.6) with  $\tilde{J} = -0.03U(q = 0)$  (see Eq. (4.5)),  $\tilde{U} = \tilde{V} = 0$ . The top (bottom) panel shows results for a displacement field of  $\Delta_1 = 20\text{meV}$  ( $\Delta_1 = 40\text{meV}$ ), respectively. The label  $l$  indicates the number of populated spin and valley flavors. The effective dielectric constant was taken to be  $\epsilon = 8$ , and the distance to the metallic gates is  $d = 150a_0$ , where  $a_0$  is the unit cell size of graphene. The calculations were performed at a low but finite temperature,  $T = 0.2\text{meV}$ .

We have explored the Hartree-Fock phase diagram of the system including the short-range interaction term (4.6) for a few parameter sets, leaving a complete mapping of the phase diagram for future work. The red curves in Fig. 4.19 show the free energy as a function of electronic density with an additional ferromagnetic Hund's rule coupling of strength  $\tilde{J} = -0.03U(q=0)$  (with  $U(q)$  given by Eq. (4.5)). The other parameters in Eq. 4.6,  $\tilde{U}$  and  $\tilde{V}$ , were set to zero. As can be seen in the figure, this value of the Hund's coupling is sufficient to completely suppress the  $l=3$  phase, in agreement with the experiment. Since  $\tilde{J} < 0$ , the region labelled by  $l=2$  is a valley-unpolarized, spin-polarized phase; this phase is favored by the  $J$  term compared to the  $l=3$  region, causing the disappearance of the latter phase. For  $|\tilde{J}| < 0.03U(0)$ , the  $l=3$  region reappears. The  $l=2$  region has the same spin polarization per electron as the  $l=1$  region, in agreement with experiment (see Figs. 4.7 and 4.12 of the main text).

The  $l=3$  region can also be suppressed by increasing  $\tilde{V}$  while keeping  $\tilde{U} = -\tilde{V}$ , which increases the repulsion between electrons in the same valley relative to the repulsion between electrons of opposite valleys. However, even for  $\tilde{V}$  as strong as  $0.25U(q=0)$ , the  $l=3$  region is not completely eliminated. Thus, within our model, we conclude that the inter-valley Hund's rule coupling  $\tilde{J}$  is much more effective than the  $\tilde{V}$  term in suppressing the  $l=3$  region.

The anisotropic interaction terms that are necessary to suppress the 3-fold region in our calculations originate from lattice scale Coulomb repulsion or electron-phonon coupling. The natural scale for such terms can be estimated as  $\int_0^{a_0} d^2r e^2/(\epsilon r) = 2\pi e^2 a_0/\epsilon$ , where  $a_0 = 0.246$  nm is the graphene unit cell size and  $\epsilon$  is an effective dielectric constant, taken for simplicity to be identical to that used in the long-range Coulomb interaction (4.5). Since we have used  $d = 150a_0 \approx 40$  nm in our calculations, the short-range interactions are naively estimated to be of the order of 0.5% – 1% of  $U(q=0)$ . The Hund's rule term needed to suppress the  $l=3$  region is of this order of magnitude



(although somewhat larger).

It is interesting to note that the current experiment strongly suggests that the 2-fold region is fully spin polarized, indicating that  $\tilde{J} < 0$ . In contrast, in the  $\nu = 0$  quantum Hall insulator in both monolayer and bilayer graphene, experiments indicate that the ground state is a valley-unpolarized, nearly spin-unpolarized state (a “canted antiferromagnet” [98, 99]), corresponding to  $\tilde{J} > 0$ . The difference between the two may come from the strong renormalization of the short-range anisotropic interactions from remote bands, which may be very different in our system than in monolayer and bilayer graphene in the quantum Hall regime.

# Chapter 5

## Superconductivity

### 5.1 Overview

Owing to the instability of Fermi liquids to arbitrarily weak attractive interactions[100], most elemental metals become superconducting at sufficiently low temperatures. However, some metals become magnetic instead. In these systems, time reversal symmetry is spontaneously broken, suppressing conventional superconducting pairing that relies on the degeneracy of Kramer’s pairs. The competition between magnetism and superconductivity can be understood from the point of view of the density of states: high density of states simultaneously favors superconductivity[101] and magnetism[1], with the ground state determined by the relative strength of the effective attractive interaction—typically mediated by phonons—and inter-electron Coulomb repulsion. In other situations, for example in heavy-fermion compounds[102], magnetism and superconductivity may be cooperative. In this scenario, magnetic fluctuations may themselves mediate attractive interactions between electrons[103], typically resulting in superconductivity with pairing symmetries other than s-wave.

In this chapter we discuss the observation of superconductivity in rhombohedral tri-

layer graphene (RTG) on the cusp of an isospin symmetry breaking transition. The crystal structure of RTG is shown in Fig. 2.2a. As in other honeycomb carbon systems, near zero doping the Fermi surfaces are localized to the two inequivalent valleys at the corners of the hexagonal Brillouin zone. Of relevance for isospin symmetry breaking, the valley provides an internal degree of freedom in addition to the electron spin. In the absence of an applied perpendicular displacement field  $D$ , the noninteracting electronic structure[72, 23] of RTG is described by three Dirac crossings in each valley (see Fig. 2.3b). At finite carrier density  $n_e \approx 10^{12} \text{cm}^{-2}$ , these Dirac pockets merge at a saddle-point van Hove singularity, where the density of states diverges (2.5). At finite  $D$  the Dirac cones become gapped, and the van Hove singularities are enhanced in magnitude. Experimentally, RTG hosts a cascade of transitions at finite doping[61, 104] where one or more of the spin- and valley symmetries spontaneously breaks. These instabilities appear to be generic to rhombohedral graphite[62], and are predicted to apply to Bernal bilayer graphene as well[105].

*Most content of this chapter is from Zhou, H. et al., Superconductivity in rhombohedral trilayer graphene. “ arXiv:2106.07640 (2021).*

## 5.2 Superconducting phenomenology in RTG

The main result of this chapter is summarized in Fig. 5.1, which shows a false-color plot of the longitudinal resistivity  $R_{xx}$  as a function of  $D$  and  $n_e$ . We observe three distinct superconducting states at these densities, which render in bright cyan on the color scale of Fig. 5.1e and which we denote SC1, SC2 and SC3. All states show nonlinear transport signatures typical of superconductivity at sufficiently low temperatures (see Figs. 5.2 and additional data in Fig. 5.3).

Fitting the nonlinear voltage to a Berezinskii–Austerlitz–Thouless model[106, 107]

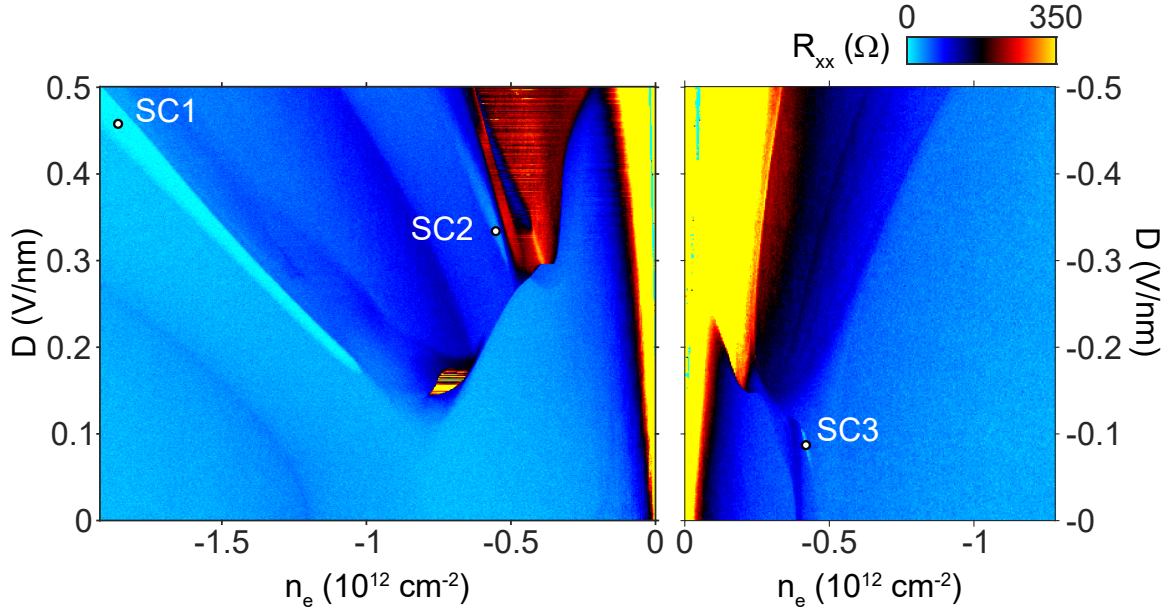


Figure 5.1: Resistivity as a function of electron density  $n_e$  and perpendicular displacement field  $D$  measured at base temperature.

gives  $T_{\text{BKT}} = 106\text{mK}$  for SC1,  $T_{\text{BKT}} = 16\text{mK}$  for SC3 while for SC2  $T_{\text{BKT}}$  appears to be just below the base temperature of our measurement system (see Fig. 5.4).

Notably, both superconducting states occur near transitions in the normal state resistivity associated with a change in the degeneracy of the Fermi surface—in other words, superconductivity occurs at a symmetry breaking transition. To better understand this connection, we measure quantum oscillations at low magnetic fields  $B_{\perp} < 1T$  (Fig. 5.5a) in the density range spanning SC1 at fixed  $D = 0.4\text{V/nm}$ . Several oscillation periods are visible across this range, indicating complex Fermi surfaces. To understand these data more quantitatively, we plot the Fourier transform of  $R_{xx}(1/B_{\perp})$  as a function of  $f_{\nu}$ , the oscillation frequency normalized to the total carrier density (Fig. 5.5b).  $f_{\nu}$  corresponds to the fraction of the total Fermi sea area enclosed by the Fermi surface generating the peak. Three regions of qualitatively different quantum oscillation spectra are visible. At extreme right, a single peak at  $f_{\nu} = 1/2$  indicates two equal area Fermi surfaces each

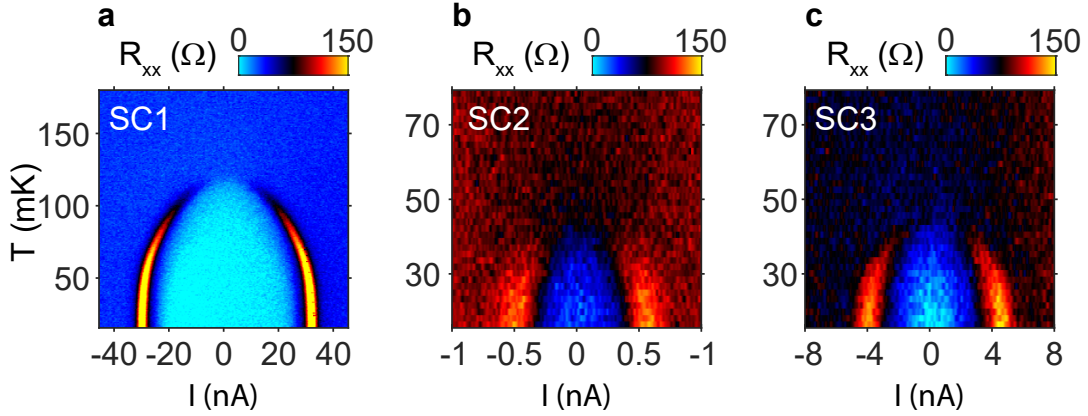


Figure 5.2: Temperature and current dependence of the differential resistivity  $dV/dI$  measured at the points in the  $n - D$  plane indicated in Fig. 5.1.

enclosing half the total Fermi sea. We associate this regime with a spin polarized, valley unpolarized ‘‘half-metal’’ state[104] with a simply connected Fermi sea in each valley. At the extreme left of the plot, several oscillation peaks with density dependent frequencies are visible. These correspond to the inner- and outer boundaries of an annular Fermi sea with the full four-fold spin- and valley-degeneracy (and harmonics). Intermediate between these two phases, the oscillation spectrum is more complex, including both strong peaks at  $f_\nu \lesssim .5$  as well as at  $f_\nu < .1$ . We identify this regime with one or more partially isospin polarized (PIP) phases, where the system has broken one of the spin- or valley symmetries but is not completely polarized into two isospin components. Comparing the quantum oscillation spectrum to base temperature transport measurements at  $B=0$  (Fig. 5.5) shows that SC1 occurs within the symmetric, annular phase and adjacent to the boundary with the PIP phase.

The appearance of superconductivity so close to a symmetry breaking phase transition opens the possibility of an unconventional superconducting state. A characteristic of many unconventional superconductors is their fragility with respect to disorder, due to the inapplicability of Anderson’s theorem[108]. Disorder in superconductors is quantified

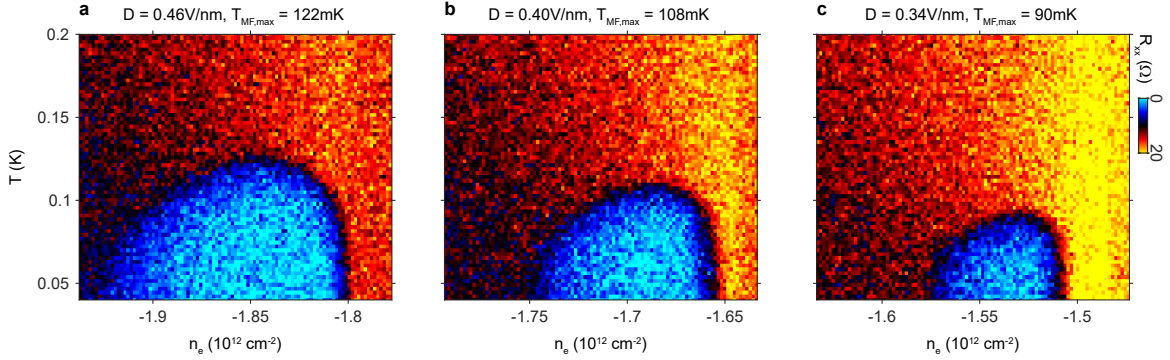


Figure 5.3: Displacement field dependence of SC1. a,  $R_{xx}$  vs  $n_e$  and  $T$  at  $D = 0.46\text{V/nm}$ . b, Same as panel a but measured at  $D = 0.40\text{V/nm}$ . c, Same as panel a and b but measured at  $D = 0.34\text{V/nm}$ .

by the ratio of the coherence length ( $\xi$ ) to the mean free path ( $\ell$ ),  $d = \xi_0/\ell$ , with the superconductivity destroyed when  $d \approx 1$  for unconventional superconductors[109]. To assess  $d$  in RTG, we study the magnetoresistance of both the superconducting and normal states.

Fig. 5.6 show the dependence of SC1 on the out-of-plane magnetic field  $B_{\perp}$ . The critical  $B_{C\perp}$  is in the 10mT range. Within Ginzburg-Landau theory,  $B_{C\perp}$  is related[110] to the coherence length by  $2\pi\xi^2 = \phi_0/B_{C\perp}^C$ , where  $\phi_0$  is the superconducting flux quantum. As a result,  $\xi \approx 150 - 250\text{nm}$  for SC1.  $\ell$  may be estimated from the Drude conductivity  $R \approx \frac{h}{e^2} \frac{1}{4k_f\ell}$  where  $h$  is Planck's constant,  $e$  is the elementary charge,  $k_f$  is the Fermi wave vector. Taking  $k_f = \sqrt{\pi n_e} \approx .25\text{nm}^{-1}$  and a normal state resistance of  $R \approx 20\Omega$  produces an estimate of  $\ell \approx 1\mu\text{m}$ , considerably larger than  $\xi$  and implying  $d \lesssim 0.2$ . However, this estimate for  $\ell$  is comparable to the lateral dimensions of our device, calling into question the validity of the Drude approach[87]. In fact, qualitative features suggest  $\ell$  may be considerably longer. Fig. 5.7a show a circuit schematic for measuring the nonlocal magnetoresistance, which has been used to detect transverse electron focusing in other graphene heterostructures[111, 112]. Measured data in the regime of SC1 (Fig. 5.7b) show a pronounced feature near  $B_{\perp} \approx .1T$ , consistent with transverse electron focusing

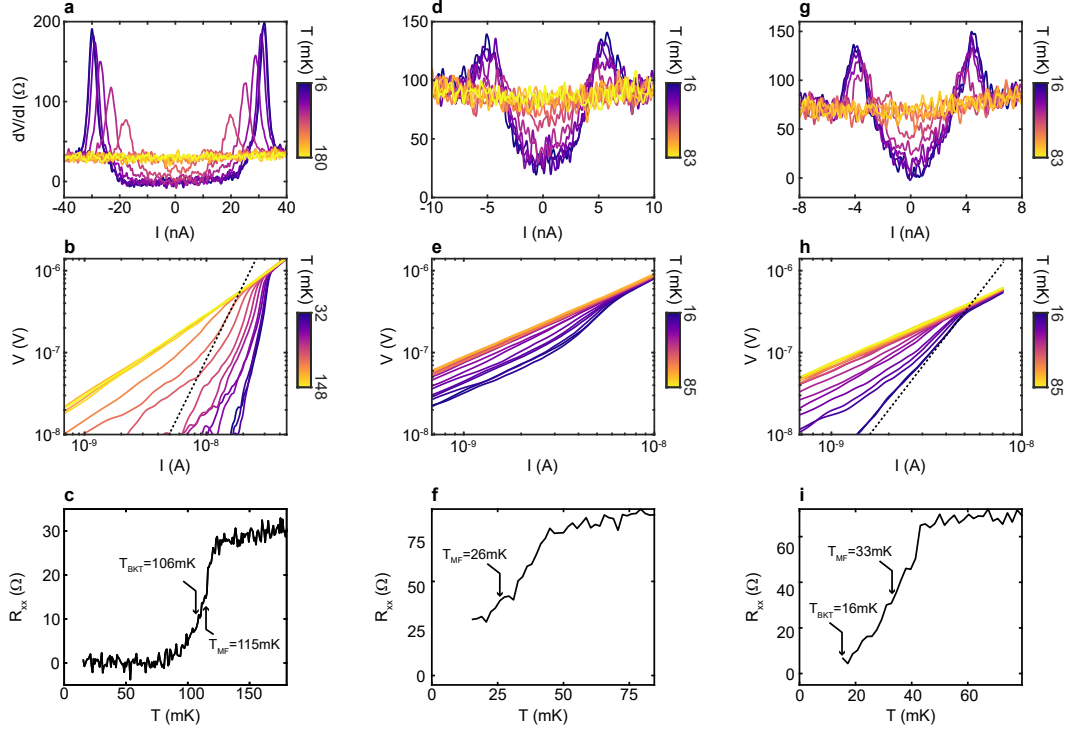


Figure 5.4: Temperature dependence of SC1, SC2, and SC3. a, Temperature dependent  $dV/dI$  measurements of SC1. Measurements were performed at  $n_e = -1.8 \times 10^{12} \text{cm}^{-2}$ ,  $D = 0.46 \text{V/nm}$ . b,  $V(I)$  for SC1. The dashed line shows  $V \propto I^3$  we take  $T_{BKT}$  as the highest temperature where the  $V(I)$  curve shows  $I^3$  scaling. c,  $R_{xx}(T)$  for SC1 with  $T_{BKT}$  and  $T_{MF}$  indicated. d, Same as panel a, but for SC2. Measurements were performed at  $n_e = -0.55 \times 10^{12} \text{cm}^{-2}$ ,  $D = 0.33 \text{V/nm}$ . e, Same as panel b, but for SC2. f, Same as panel c, but for SC2. g, Same as panels a and d, but for SC3. Measurements were performed at  $n_e = 0.41 \times 10^{12} \text{cm}^{-2}$ ,  $D = -0.087 \text{V/nm}$ . h, Same as panels b and e, but for SC3. i, Same as panels c and f, but for SC3.

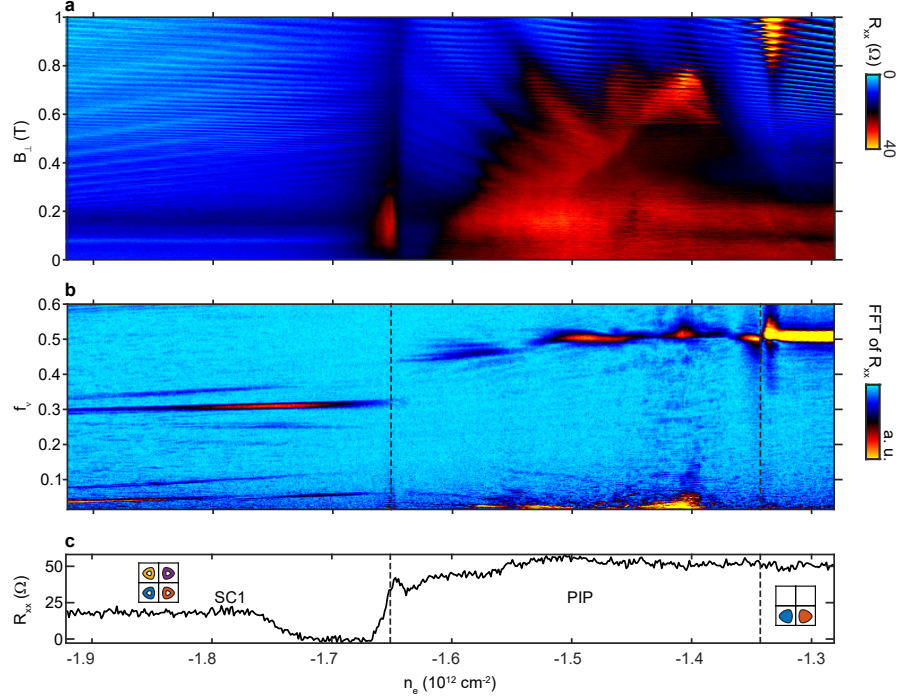


Figure 5.5: SdH oscillation and Fermiology near SC1. a,  $R_{xx}$  vs  $n_e$  and  $B_{\perp}$  measured at  $D = 0.4\text{V/nm}$ . b, Fast Fourier transform of the results in panel a along the y-direction. Phases with different Fermi surfaces are separated by dashed lines. c,  $R_{xx}$  vs  $n_e$  at  $B = 0$ . Insets: Schematic Fermi contours of the different phases identified by SdH oscillations.

between the contacts, which are separated by a pitch of  $L \approx 2.3\mu\text{m}$ . This feature—which is observed across all densities in our device (Fig. 5.7)—suggests  $\ell \gtrsim \pi L/2 \approx 3.5\mu\text{m}$ . Taking this estimate for  $\ell$  gives a disorder parameter  $d \sim .05$ . These estimates place the superconductivity firmly in the clean limit, where unconventional superconductivity may be expected to survive.

To further explore the properties of SC1, we show the response to an in-plane magnetic field in Fig. 5.8a. The in-plane critical field  $B_{\parallel C}$  is several hundred millitesla, more than one order of magnitude larger than  $B_{\perp C}$  consistent with the 2D nature of the superconductivity. To explore the mechanism for the magnetic field induced breakdown of superconductivity, Fig. 5.8b shows the dependence of both  $T_{\text{BKT}}$  and  $T_{1/2}$  on  $B_{\parallel}$ . The



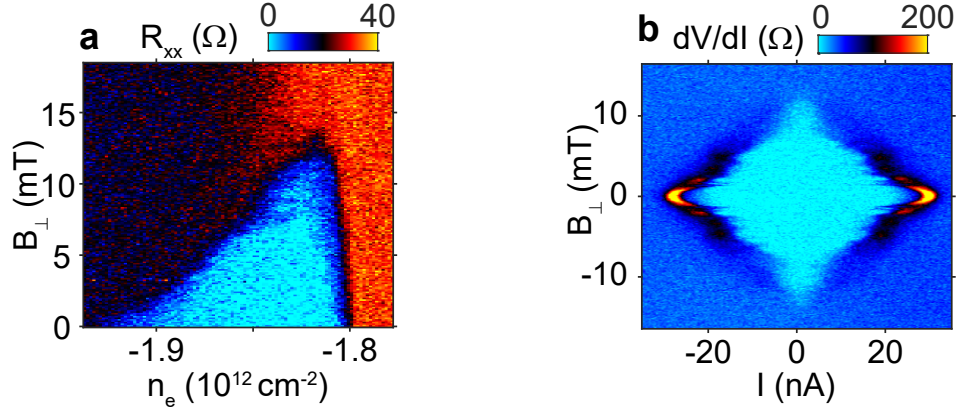


Figure 5.6:  $B_{\perp}$ -dependence of SC1. a,  $B_{\perp}$ -dependent  $R_{xx}$  measured at  $D = 0.4\text{V/nm}$ . b,  $B_{\perp}$ -dependence of the nonlinear resistivity at  $n_e = -1.83 \times 10^{12}\text{cm}^{-2}$  and  $D = 0.46\text{V/nm}$ .

data are well fit by the relation  $T_C/T_C^0 = 1 - (B_{C\parallel}/B_{C\parallel}^0)^2$  for a superconductor limited by Pauli paramagnetism[113, 114], where  $B_{C\parallel}^0$  and  $T_C^0$  describe the  $T=0$  critical field and  $B_{\parallel} = 0$  critical temperature, respectively. For both fits, we find  $\mu_B B_{C\parallel}^0 / (k_B T_C^0) = 1.7$ , close to the values 1.23 predicted by weak coupling BCS theory without accounting for the Coulomb repulsion or finite temperature effects. We thus conclude that the  $B_{\parallel}$  dependence is likely compatible with a conventional spin-singlet order parameter.

In contrast, the phenomenology of SC2 is not compatible with conventional spin-singlet pairing. As is evident from the quantum oscillations shown in Figs. 5.9, SC2 emerges from a two-fold degenerate annular Fermi sea associated with a spin-polarized half-metal[104].

While the low  $T_C$  of SC2 complicates quantitative analysis of the kind presented for SC1, signatures of SC2 persist to very large values of  $B_{\parallel}$ , with  $B_{C\perp}$  and the critical current nearly unchanged for  $B_{\parallel}$  as high as 1T (Figs. 5.11). Taking a conservative estimate of 50mK for  $T_C^0$  and 1T for  $B_{C\parallel}^0$ , SC2 violates the Pauli limit by more than one order of magnitude, consistent with a spin-polarized superconductor.

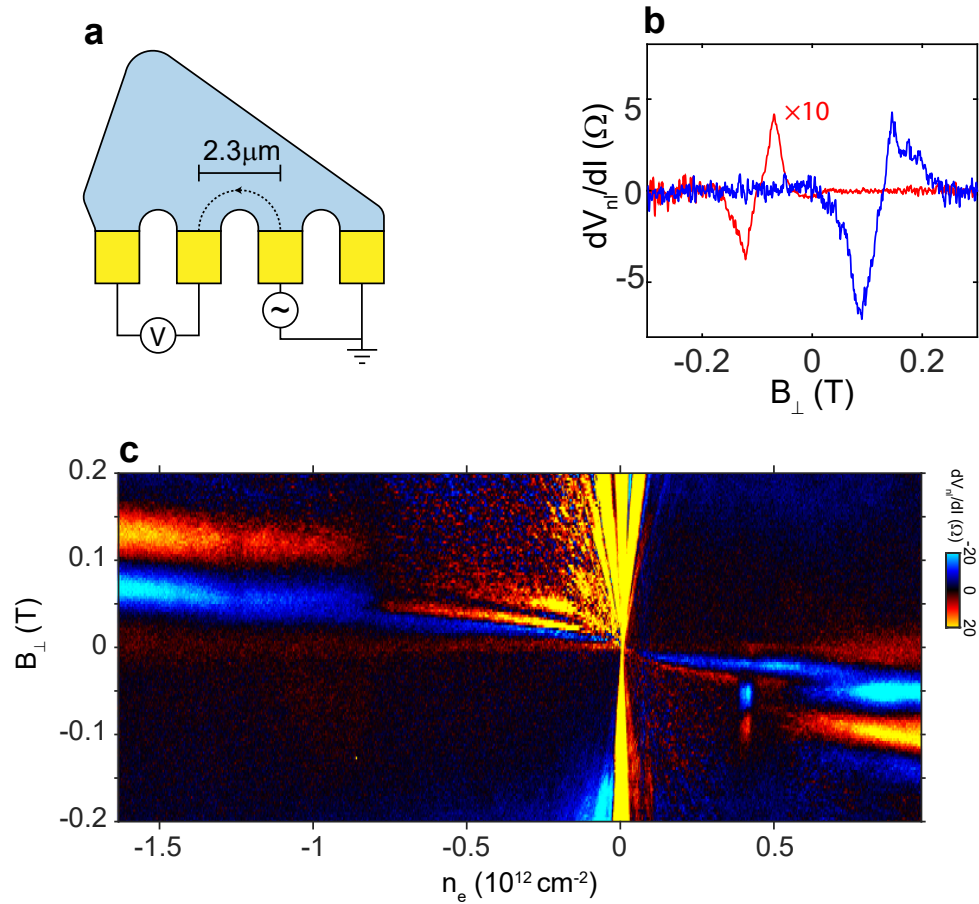


Figure 5.7: Magnetic focusing experiment. a, Device and circuit schematic for measuring transverse magnetic electron focusing. b, Magnetic-focusing induced non-local voltage measured at  $n_e = -1.83 \times 10^{12}\text{cm}^{-2}$ ,  $D = 0.46\text{V/nm}$  (blue) and  $n_e = 1.83 \times 10^{12}\text{cm}^{-2}$ ,  $D = 0$  (red). For the red curve, the nonlocal resistivity has been multiplied by 0.1. c, Non-local resistance measured in the configuration in panel a as a function of  $n_e$  and  $B_\perp$  at  $D=0$ .

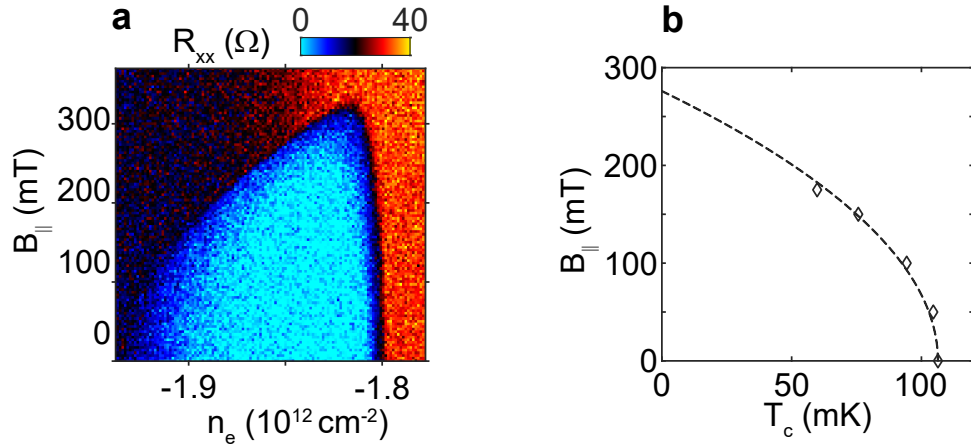


Figure 5.8: In-plane magnetic field response of SC1. a,  $B_{||}$ -dependent  $R_{xx}$  measured at  $D = 0.4\text{V/nm}$ . b,  $B_{||C}$  dependence of  $T_{\text{BKT}}$  and  $T_{1/2}$  measured at  $n_e = 1.83 \times 10^{12}\text{cm}^{-2}$ ,  $D = 0.46\text{V/nm}$ . Lines show fits to the phenomenological relation  $T_C/T_C^0 = 1 - (B_{C||}/B_{C||}^0)^2$ .

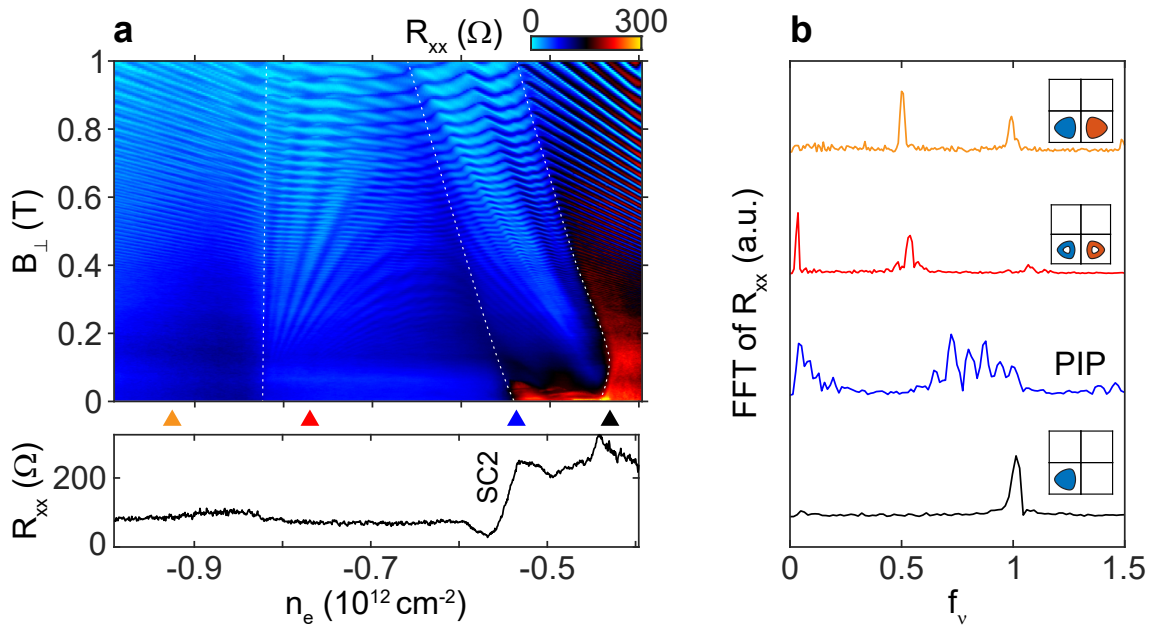


Figure 5.9: Fermiology near SC2. a, Top:  $R_{xx}$  as a function of  $n_e$  and  $B_{\perp}$  for  $D = 0.33\text{V/nm}$ . Bottom:  $R_{xx}$  at  $B = 0$  for  $D = 0.33\text{V/nm}$ . b, Fourier transforms of  $R_{xx}(1/B_{\perp})$  for the values of  $n_e$  indicated by arrows in panel a. Insets: Schematic Fermi contours.

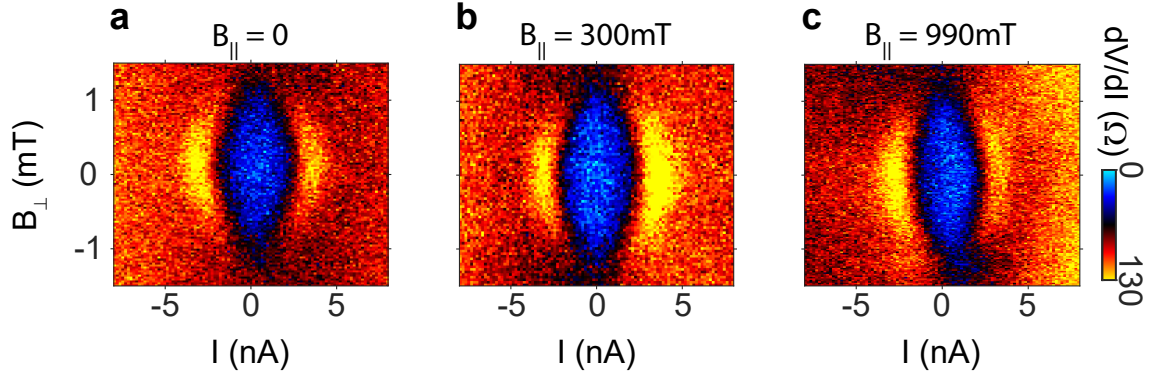


Figure 5.10:  $dV/dI$  measured at  $n_e = -0.55 \times 10^{12} \text{cm}^{-2}$  and  $D = 0.33 \text{V/nm}$

For attractive interactions of finite range, such as arise from electron phonon interactions, pairing potentials are attractive in all angular momentum channels. The potential is strongest in the s-wave channel, favoring conventional spin-singlet pairing in normal metals. In the spin-polarized half-metal regime where SC2 occurs, electrons with reversed spin are separated energetically from the ground state by the exchange energy, which at several meV[104] is at least two orders of magnitude larger than observed superconducting gaps. Spin-singlet pairing is thus energetically precluded. The unique properties of graphene nevertheless allow for superconductivity from conventional pairing mechanisms. Most importantly, the negligible spin-orbit coupling endows the spin-polarized half-metal with spinless time-reversal symmetry, which guarantees degeneracy between electrons in opposite valleys but with the same spin even in the absence of inversion symmetry. The smaller  $T_C$  of SC2 relative to SC1 is consistent with pairing in a higher angular momentum channel by the same interaction. One natural order parameter, proposed for moire systems with similar symmetries, is the spin-triplet, valley singlet  $\langle \hat{c}_{k\uparrow}^\dagger \hat{c}_{-k,\uparrow}^\dagger \rangle$ [115, 116]. This form of superconductivity shares many similarities with conventional superconductors, most notably protection from intra-valley scattering by smooth disorder potentials.

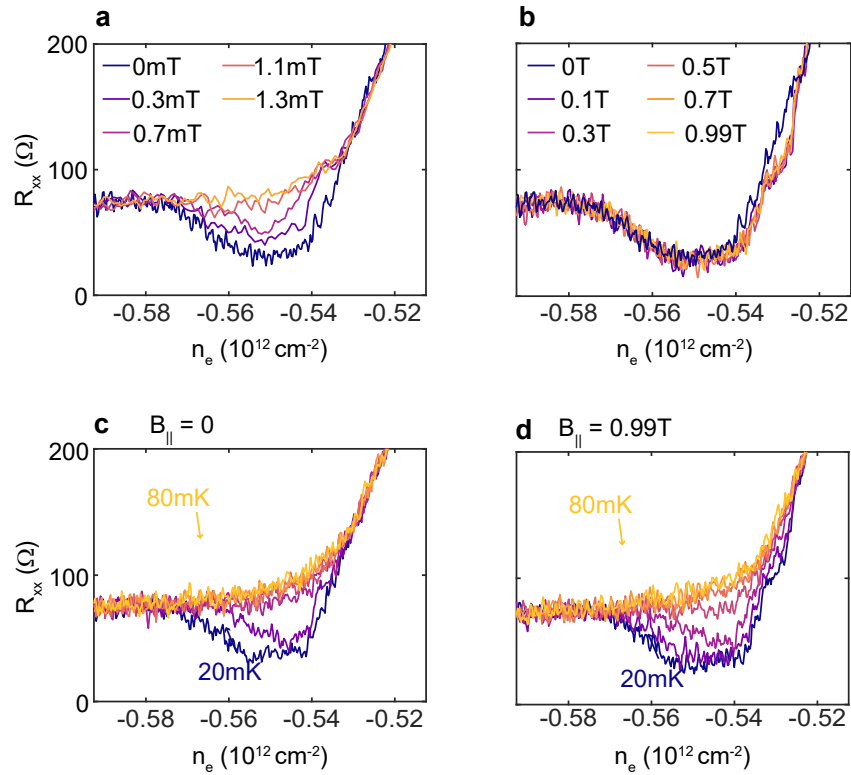


Figure 5.11: Temperature and magnetic field dependence near SC2. a, Temperature dependence of  $R_{xx}$  vs  $n_e$  measured at  $D = 0.33\text{V/nm}$ . Temperatures between traces are equally spaced. b, Same as a, measured with an  $0.99\text{T}$  in-plane magnetic field applied.

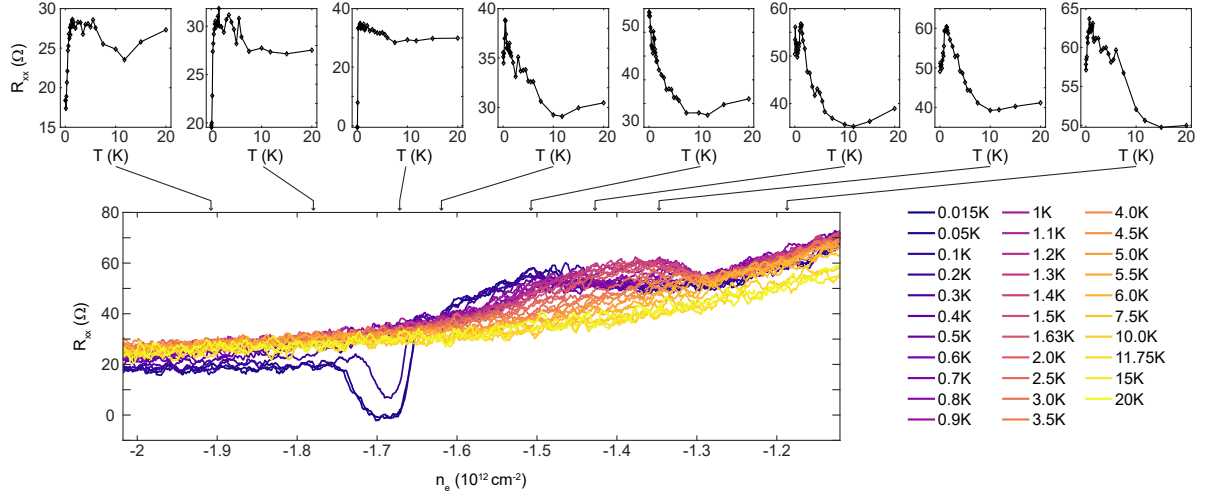


Figure 5.12: Temperature dependence of  $R_{xx}$  measured at  $D = 0.4 \text{ V/nm}$  and  $n_e < 0$  bottom panel shows  $R_{xx}$  as a function of  $n_e$  at different temperature. Top panels show  $R_{xx}$  vs  $T$  at fixed  $n_e$  extracted from the bottom panel.

### 5.3 Discussion

The common features shared by SC1 and SC2 suggest several possible mechanisms, both conventional and all-electronic.

Most obviously, the appearance of superconductivity near symmetry breaking phase transitions suggests that fluctuations of the proximal ordered state may play a role in pairing[103]. The plausibility of this picture hinges on the nature of the transition. Experimentally, the sudden jump in quantum oscillation spectra observed near the superconductors is suggestive of a first order transition. In this case, fluctuations might be suppressed. However, the resistivity of the normal state changes only gradually across the transition, contrasting with other isospin transitions studied in the same sample that are strongly first order[104]. Measurements of the thermodynamic compressibility[104] similarly do not show strong negative compressibility where superconductivity is observed, allowing for the possibility of a continuous transition.

The nature of the proximal ordered state also plays a key role in fluctuation me-

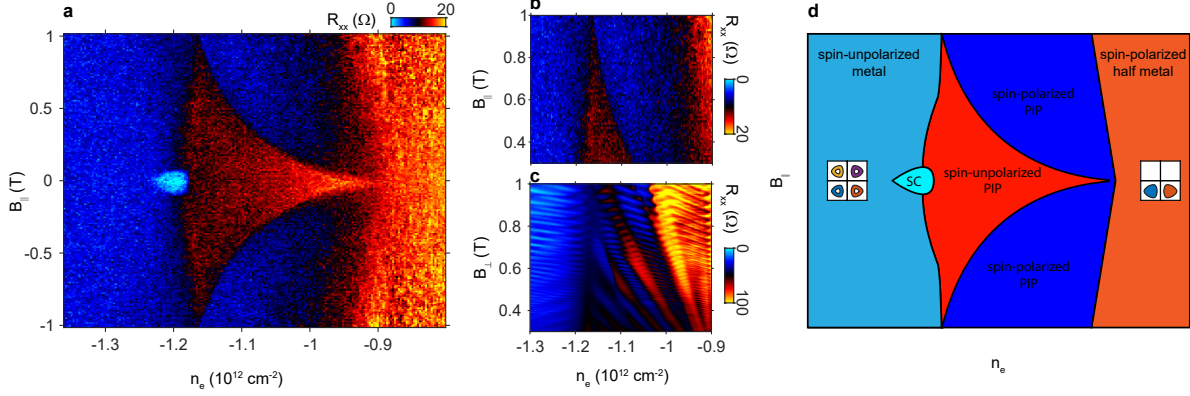


Figure 5.13: Temperature dependence of  $R_{xx}$  measured at  $D = 0.4\text{V}/\text{nm}$  and  $n_e < 0$  bottom panel shows  $R_{xx}$  as a function of  $n_e$  at different temperature. Top panels show  $R_{xx}$  vs  $T$  at fixed  $n_e$  extracted from the bottom panel.

diated superconductors, with different orders producing attraction in different pairing channels[103]. In RTG, in-plane field measurements show that the PIP phase proximal to SC1 is likely spin-unpolarized (Fig. 5.12). To match the experiment, then, a theory of fluctuation mediated superconductivity for SC1 should produce an apparently Pauli-limited superconductor from fluctuations of a spin-unpolarized isospin ordered state—a strong constraint.

Alternatively, superconductivity and symmetry breaking may arise in close proximity from unrelated mechanisms[40, 117]. Within BCS theory, the superconducting transition temperature in the antiadiabatic limit[3] applicable to low-density electron systems is approximated by

$$T_C = T_F e^{-1/\lambda} \quad (5.1)$$

where the Fermi temperature  $T_F \approx 50\text{K}$  in the regime of interest and  $\lambda = g\rho$  is the dimensionless coupling constant characterizing attractive interactions, which depends on the coupling constant  $g$  and the density of states. For a density independent  $g$ —as expected for phonon mediated attraction, for example—superconductivity is observed at

temperature  $T$  when  $\rho$  exceeds  $\rho_{SC} = \frac{1}{g \log(T_F/T)}$ . This approach has been used to predict superconductivity in rhombohedral graphite[118]. However, high density of states also favors symmetry breaking, with the boundary between ordered and disordered states defined by the Stoner criterion,  $\rho_{FM} > 1/U$  where  $U$  parameterizes the Coulomb repulsion.

As  $\rho$  increases—as occurs in our experiment as  $|n_e|$  is reduced—one of two scenarios obtains. For  $\rho_{FM} < \rho_{SC}$ , the Stoner criterion is satisfied first, and the Fermi liquid becomes magnetic. As a result,  $\rho$  decreases, the Kramers degeneracy is lifted, and superconductivity is not observed. Conversely, if  $\rho_{FM} > \rho_{SC}$ , superconductivity is observed. However, as the density of states is *further* increased above  $\rho_{FM}$ , the system nevertheless becomes magnetic. In this case the domain of superconductivity is bounded from below by  $\rho_{SC}$  and from above by  $\rho_{FM}$ . Superconductivity occurs at the cusp of a magnetic transition, precisely as observed, despite the lack of a causal link between the two.

Bolstering the case for this scenario is the fact that both superconductors arise at the threshold of a magnetic transition but are predominantly within the *disordered phase*; quantities such as  $B_{C\parallel}$  and  $B_{C\perp}$  rise gradually as the isospin symmetry breaking transition is approached before rapidly collapsing at the transition itself. However, a key question remains as to whether this picture is consistent with the seemingly narrow range of  $n_e$  over which superconductivity is observed. For example, SC1 occurs over a density range  $\Delta n/n \approx 5\%$ . Comparing the maximum  $T_C \approx 100\text{mK}$  to our estimated base temperature of 30-40mK, we estimate  $\Delta T_C/T_C \approx 0.6 - 0.7$  over this same range. For this to be accounted for entirely by a change in  $\lambda$ ,  $\Delta\lambda/\lambda \approx .1$ , about twice as large as expected from single-particle calculations of the density of states. More detailed calculations (for instance, accounting for both the Coulomb repulsion and finite temperature effects[119]) may assess whether this quantitative discrepancy is significant.

In both phonon- and fluctuation-mediated superconductors, high temperature transport typically shows signs of electron scattering by the same neutral modes that mediate



the superconductivity[120]. We find no sign of enhanced high temperature scattering, at least up to 20K (Fig. 5.12). A mechanism for superconductivity—albeit not usually in the s-wave channel—that does not invoke soft modes was given by Kohn and Luttinger based on the intrinsic instability of the Fermi liquid[121]. While thought to occur only at experimentally inaccessible temperatures and disorder strengths in most materials, it has been proposed[122] that in semiconductor quantum wells with two occupied subbands, this effect may be enhanced. Given the similarity between a two subband system and the annular Fermi seas we describe above, combined with the exceptionally low disorder in RTG, exploration of such mechanisms may be warranted.

In closing, we comment on the possible relationship between the superconductivity reported here and that observed in moiré systems. In RTG aligned to hexagonal boron nitride, the moire potential only weakly perturbs the underlying isospin symmetry breaking[104]. The  $n_e$  and  $B_{\parallel}$  dependence of the signatures of superconductivity observed in that system[64] would appear to be most consistent with SC2. Twisted bilayer[123] and twisted trilayer[124, 125] have different microscopic symmetries; however, they share several features with RTG including enhanced density of states and isospin symmetry breaking. We conjecture that the superconductivity observed in all graphene systems has the same basic origin.

# Chapter 6

## Effects of a Moiré Potential

### 6.1 Overview

Since the lattice structure of graphene and hBN is nearly identical, when the graphene and hBN layer have their lattice nearly aligned, a Moiré pattern is created, where is roughly a period feature with the period larger than those of the graphene and hBN lattices. This effect is schematically shown in Fig .6.2a.

Quantitatively, the wavelength of the Moiré superlattice can be expressed as

$$\lambda = \frac{(1 + \delta)a}{2(1 + \delta)(1 - \cos \phi) + \delta^2}, \quad (6.1)$$

where  $\delta$  is the difference of the lattice constant,  $\theta$  is the relative angle between the two lattice. For graphene (monolayer or multilayer) and hBN, when the two lattice is perfectly aligned ( $\theta=0$ ), the maximum  $\lambda \approx 14$  nm is reached. The presence of Moir'e pattern will alter the energy band structure. The long wavelength of the Moiré pattern will open energy gaps at a moment  $k = 2\pi/\lambda$ . With  $\lambda = 14$ nm, the energy gap is near the band top/bottom of RTG where the energy is not sensitive to momentum. In this case, an

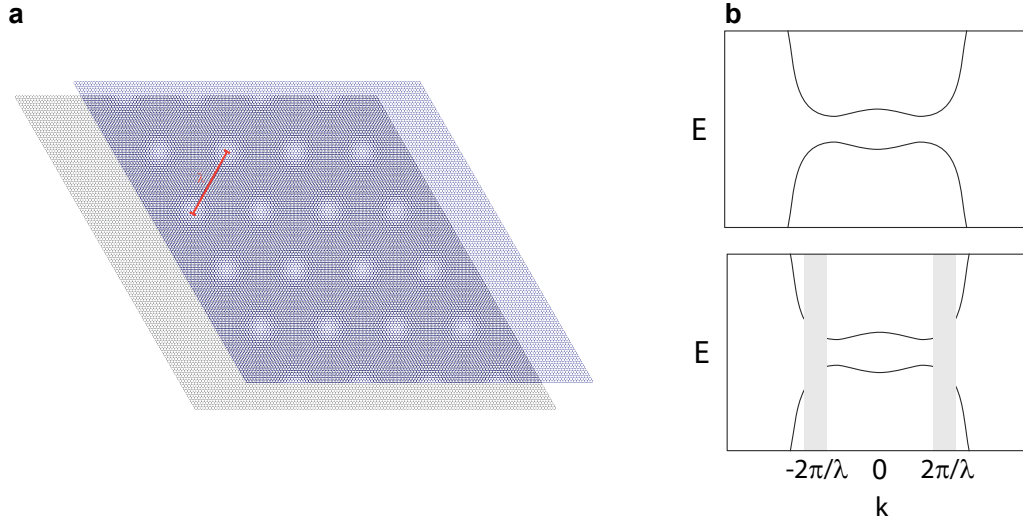


Figure 6.1: Formation of Moiré superlattice. a, schematic of the Moiré superlattice when two honeycomb lattices with a small lattice constant mismatch is aligned to each other. b, Schematic band structure of RTG with (bottom) and without (top) a Moiré superlattice.

isolated flat energy band is formed (See Fig. 6.4 for a schematic illustration.), which can usually induce strongly correlated electron phenomena.

*Part of the results discussed in this chapter is from H. Zhou, T. Xie, A. Ghazaryan, T. Holder, J. Ehrets, E. M. Spanton, T. Taniguchi, K. Watanabe, E. Berg, M. Serbyn, A. F. Young. “Half and quarter metals in rhombohedral trilayer graphene.” arXiv:2104.00653. (2021)*

## 6.2 Effects of the Moiré Potential

Recently, manifestations of strong interaction have emerged in rhombohedral trilayers aligned to hexagonal boron nitride at densities comparable to the phase transitions reported here [63, 64, 8]. In these devices, insulating states have been observed at filling  $\nu = -1$  and  $-2$  of the superlattice unit cell, including an incipient Chern insulator at  $\nu = -1$ . These experimental findings were interpreted as resulting from polarizing an

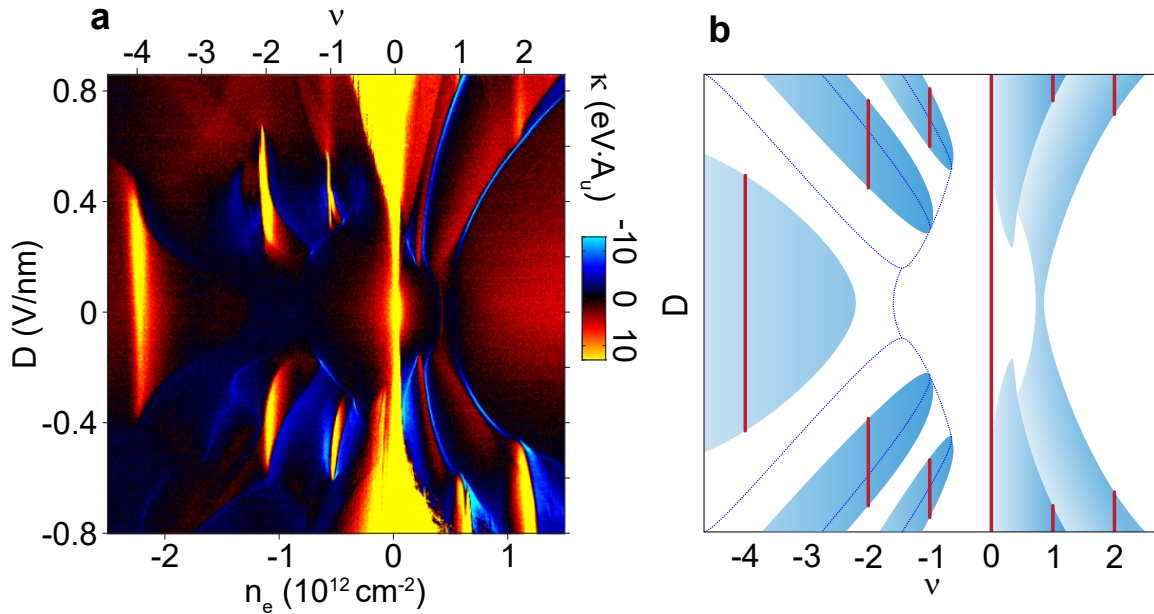


Figure 6.2: Effect of a moiré superlattice potential. **a**,  $\kappa$  measured in sample B where the lattice of the rhombohedral trilayer graphene is aligned to that belonging to one of the encapsulating hBN crystals. **b**, Schematic illustration of the formation of insulating states. Dashed lines indicate Lifshitz transitions described in Fig. 4.12 and blue regions indicate domains of half- and quarter metal states in the absence of the moiré potential.

emergent flat band into one or more valley and spin flavors.

Although these observations can be attributed to the presence of isolated flat bands, it is interesting to reexamine this picture in light of our finding that rhombohedral graphite spontaneously breaks spin and valley symmetry in the absence of a moiré potential, which amounts to quantifying the difference between moiré superlattice and non-moiré superlattice trilayer devices.

We address this question directly by measuring the inverse compressibility data in a rhombohedral trilayer device aligned to one of the encapsulating hexagonal boron nitride layers, but that has otherwise identical geometry to the unaligned device presented in Fig. 6.3a. We find the negative compressibility features associated with Stoner transitions nearly unchanged in the aligned, Moiré device. The primary difference is the

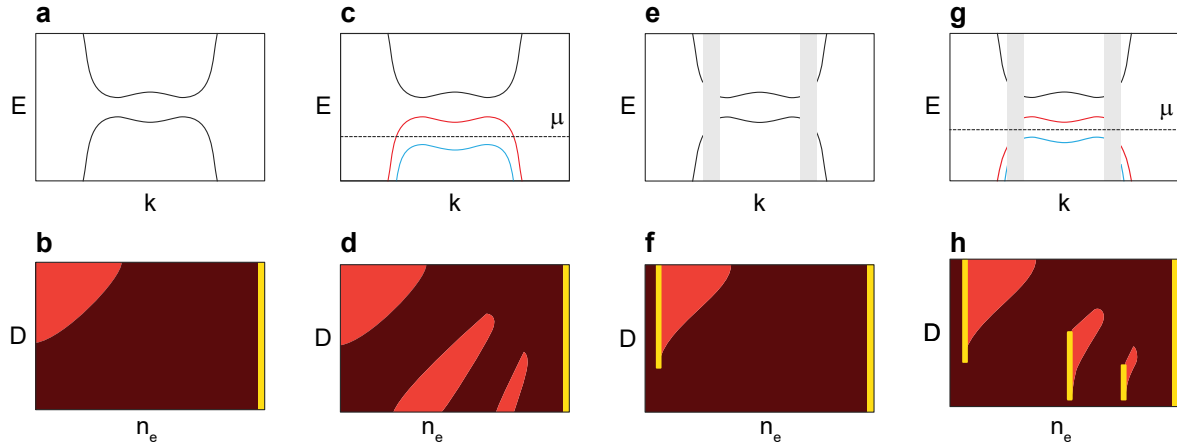


Figure 6.3: Origin of the symmetry breaking insulating states. a, Schematic band structure of RTG in the absence of Moiré potential and electron-electron interaction. b, Schematic inverse compressibility in the  $n_e$  and  $D$  parameter space corresponding to a. c, Same as a, with interaction considered. The red and blue represent symmetry breaking energy band. d, Same as b, with interaction included. e, Same as a, with a Moiré potential present. An energy gap opens up at the border of the superlattice Brillouin zone. f, Same as b, with a Moiré potential included. g, Same as a, with both interaction and a Moiré potential present. The interplay of symmetry breaking and Moiré potential induces multiple isolated symmetry breaking flat bands at specific Fermi level, resulting in symmetry breaking insulating states. h, Same as b, with both interaction a Moiré potential included.

appearance of incompressible states at commensurate fillings  $\nu = \pm 1, \pm 2$  of the moiré unit cell. The relationship between these insulators and the underlying symmetry breaking in non-moiré devices is depicted schematically in Fig. 6.3a, where we overlay the phase boundaries measured in intrinsic trilayers with the domain of stability of the commensurate, incompressible states in moiré patterned trilayers. Evidently, incompressible states emerge whenever the superlattice filling is divisible by the degeneracy of the Fermi surface at the same  $n_e$  and  $D$  absent a moiré. The effect of the moiré can thus be understood as a perturbation that does not qualitatively alter the correlated electron physics already present in the parent trilayer.

This mechanism is schematically illustrated in Fig. 6.4, where we "virtually" turn

on and off the Moiré potential and electron-electron interaction and see how the energy dispersion and inverse compressibility will change. Without the Moiré potential and interaction (Fig. 6.4a and b), the conduction and valence band can be calculated from the continuum model. In this case, the inverse compressibility profile shows only features from the charge neutrality point and the Lifshitz transition, as calculated by the continuum model in Fig. 4.6. If the interaction is considered in intrinsic RTG, we reach a situation we discussed in detail in Chapter 4. In this case, when the Fermi surface is shifted to a position to meet the Stoner criterion, spontaneous symmetry breaking happens and the energy band split into a multiple bands. In this case, additional features show up in the inverse compressibility profile (Fig. 4.6c). In a situation when a Moiré potential exists, but interaction is not strong, an energy gap opens up at  $k = \pm \frac{2\pi}{\lambda}$  but no spontaneous breaking will happen. In this case, an isolated flat band is induced from both the conduction and valence band, and a feature of an incompressible state is expected in the  $\kappa$  vs  $n_e$  and  $D$  profile at both electron and hole doping. (Fig. 6.4e and f.) When both interaction and Moiré potential exist, the interplay of the two facts will allow multiple isolated flat band at proper carrier density (Fig. 6.4g) and therefore multiple incompressible states are expected to exist (Fig. 6.4h).

Our results show that rhombohedral graphene is an ideal platform for well controlled tests of many-body theory, and reveal magnetism in moiré materials[7, 91, 8, 126] to be fundamentally itinerant in nature.

### 6.3 Symmetry Breaking Insulating States

In crystalline systems incompressible gapped states can only occur at commensurate fillings of the lattice. The moiré superlattice is qualitatively important in that it allows for gapped states at carrier densities that can be reached by electrostatics gates, and we

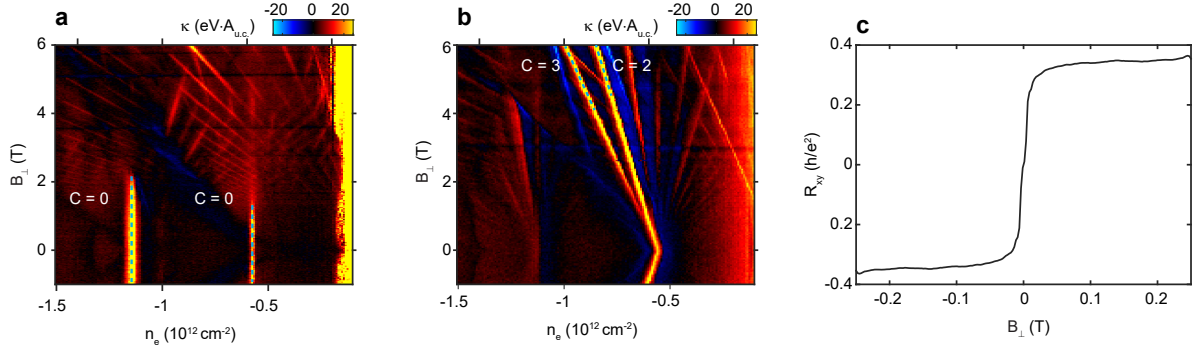


Figure 6.4: Magnetic field response of the insulating states. a, Inverse compressibility versus carrier density and out-of-plane magnetic field at  $D = 0.52$  V/nm measured in sample B. b, same as c measured at  $D = -0.57$  V/nm. c,  $R_{xy}$  versus  $B_{\perp}$  measured at  $n_e = -0.52 \times 10^{12}$  V/nm,  $D = -0.47$  V/nm.

observe several classes of commensurate gapped states driven by electron interaction in our high quality samples. Gapped states are classified by two quantum numbers,  $s$  and  $t$ , which respectively encode the number of electrons per lattice site and the Chern number, which is linked to the quantized Hall conductivity. We classify gaps by the resulting trajectories in the  $n_e$ - $B_{\perp}$  plane,  $\nu = tn_{\phi} + s$ , where  $n_{\phi}$  is the number of magnetic flux quanta per unit cell. Consistent with prior work, we find that commensurate insulators at  $\nu = -1$  and  $\nu = -2$  states are topologically trivial for  $D > 0$ , with  $(s, t) = (-1, 0)$  and  $(-2, 0)$ , respectively (see Fig. 6.5b). In contrast, the  $\nu = -1$  insulators is nontrivial for  $D < 0$  (Fig. 5.4a). Our high resolution data allow us to observe a close competition between robust  $t = -2$  and  $t = -3$  Chern insulators for  $s = -1$ . At high magnetic field, these states occur at different densities, and high inverse compressibility peaks are observed corresponding to both trajectories. As  $B_{\perp}$  tends to zero and the states converge to the same density, the  $t = -2$  state wins the energetic competition, consistent with transport data (see Fig. 6.5 and Ref. [8]).

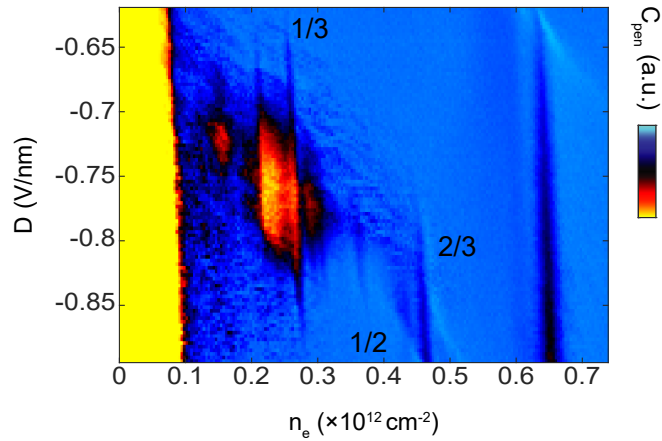


Figure 6.5: Penetration field capacitance data as a function of  $n_e$  and  $D$ . Filling factors of some incompressible states are marked on the top axis.

## 6.4 Charge Density Waves at fractionally filled Moiré Bands

As shown in Figure 6.5d, we also observe a number of features at *fractional* filling of the Moiré superlattice bands. These states are all found to have  $t = 0$  in the low  $B_{\perp}$  limit, and occur at  $\nu = s = 1/3, 1/2, 2/3, \dots$ . The regime where these states are observed corresponds within single particle band structure models to a regime where an unusually flat topologically trivial flat band is partially filled[127]. We interpret them as generalized Wigner crystals, in which electron repulsion leads to commensurate filling of the Moiré potential, breaking the superlattice symmetry. Similar states have been reported in transition metal dichalcogenide heterobilayers[128, 129]

## 6.5 Incompressible States under Magnetic Field

As mentioned in Chapter 4, the anisotropic nature of the valley degree of freedom allows different magnetic phases even when the spin and valley degeneracy is fixed. For



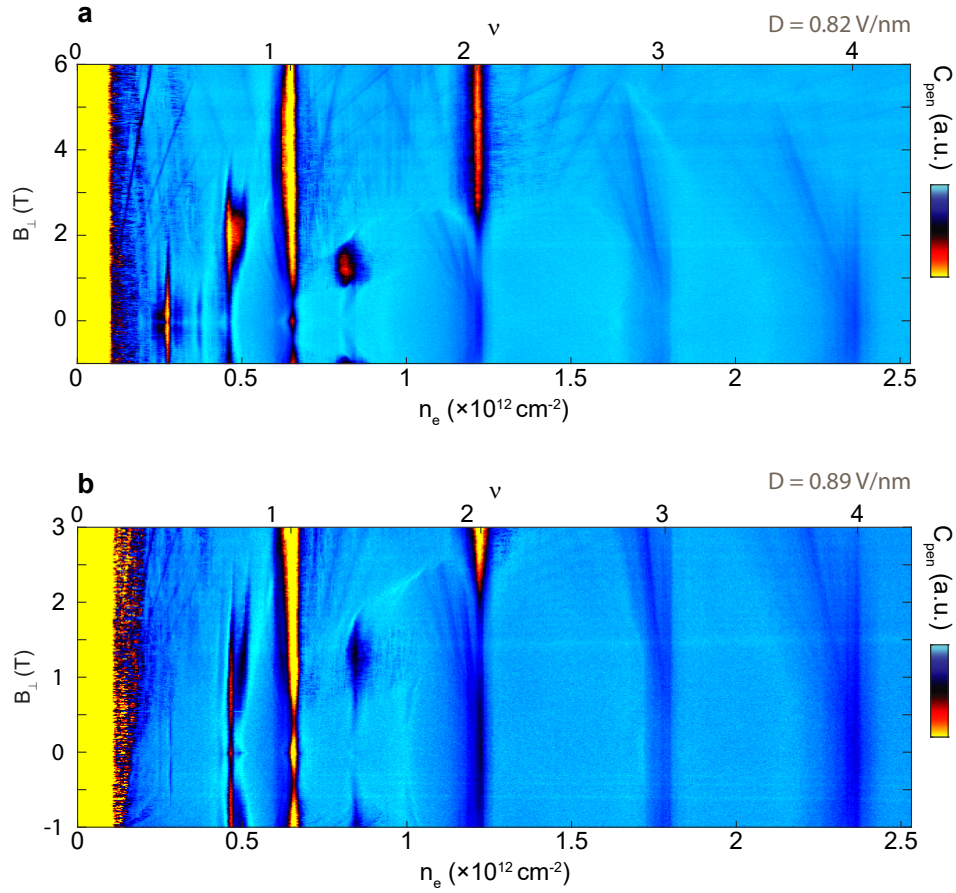


Figure 6.6: Magnetic field induced phase transitions at commensurate fillings. a, Penetration field capacitance as a function of  $n_e$  and  $B_{\perp}$  measured at  $D = 0.82\text{V/nm}$ . The filling factors are marked on the top axis. b, Same as a, measured at  $D = 0.89\text{V/nm}$ .

example, when both spin- and valley-degeneracy is lifted, the ground state could be spin and valley polarized phase, a spin polarized intervalley coherent phase or a spin-valley locked intervalley coherent phase. Phase transitions have been observed in intrinsic RTG.

In presence of a Moiré superlattice, the insulating states at commensurate fillings are likely to inherit the complex magnetic ordering of the spin- and valley- symmetry breaking phases. Transitions between these insulating states are expected under the change of density, displacement field and external magnetic field.

Unlike the intrinsic RTG, where such phase transition are observed at hole-doping. Similar phenomena are not observed in the Moiré potential-induced insulating state at

hole-doping. This is not surprising since these insulating states only span a narrow range of  $D$  in the parameter space. Even if multiple phases exist in the symmetry broken region, the insulating states only belong to a single magnetic ordering.

Instead, with a very large displacement field applied, phase transitions are observed at the insulating states at electron-doping when varying the out-of-plane magnetic field. (Fig. 6.6). At  $\nu = 1$ , the inverse compressibility goes across a minimum as the out-of-plane magnetic field increases from zero, indicating a phase transition. As  $B_{\perp}$  favors phases with large orbital magnetic moment, it is likely the insulator is only spin-valley polarized at finite  $B_{\perp}$ . At zero  $B_{\perp}$ , it is instead a valley-coherent insulator.

Similar features are also observed at other insulating states with integer or fractional filling of the Moiré band. And the phase transitions are sensitive to the electrical displacement field applied.

The carrier density at which the insulating states appear is not sensitive to the magnetic field, this further proves that the nature of these states are charge density waves where the lattice symmetry is broken, instead of fractional Chern insulators. Nevertheless, an insulating state near  $\nu = 2/3$  corresponding to a Chern number of 1 emerges as  $B_{\perp}$  increases from zero, and then disappears above around 3T. The nature of this state is yet fully understood.

These observations indicate that while the Moiré potential only perturbatively couples to the RTG in a global picture, the subtle change of the electronic properties can introduce new physics that is completely different from the intrinsic RTG.

# Chapter 7

## Summary and Outlook

In this work, we studied in detail the electronic properties of RTG. We developed a process to fabricate dual-gated trilayer graphene transistors while maintaining the metal stable ABC-stacking order. The process integrates multiple experiment techniques including Raman spectroscopy, atomic force microscope manipulation and Van der Waals heterostructure fabrication.

With the sample fabricated, we performed electrical measurement including both penetration field capacitance and transport measurement, taking the advantage of both measurement techniques. We observed spontaneous spin- and valley- symmetry breaking which originates from electron-electron interactions. At electron doping, a rigid band model with Stoner type interaction is build and well captures most observed features. At hole doping, the interplay of magnetic phase transition and Lifshitz transition complicated the phase diagram. The Shubnikov de Haas oscillation analysis is applied to probe the Fermiology of these phases.

Near some phase boundaries of magnetic transition, three superconductive phases are observed, with maximal critical temperature of around 100mK. Magnetic field response indicate they have different paring symmetry. Magnetic focusing ex far from

fully understood. The Stoner model captures the major magnetic phase transitions on a phenomenological level, but the mechanism behind the unique Hund's coupling remains unclear. Besides, the detailed spin- and valley-structure within a symmetry-breaking phase is not captured by the Stoner model.

The observation of ferromagnetism and superconductivity shows that the structurally-simple RTG is actually a complex and interesting electronic system. Unlike the moiré system, which is an unstable state and usually contains small domains, RTG's metastable nature makes it possible to be spatially uniform and consistent among different samples. These features reduce the difficulty of modeling and understanding the electronic behavior.

On the other hand, our understanding of the magnetism and superconductivity is far from complete and worth further investigation.

On the theory side, the challenging part of effectively modeling the itinerant electrons in RTG is to take the electronic screening effect into consideration, which is not relevant when the system is an insulator, but become important when the system is metallic and has a Fermi sea. Either the rigid band model or the Hartree-Fock model failed to treat this effect properly. This could explain the always existing 3-fold degenerated phase in Hartree Fock calculations. A proper way to treat electronic screening will hopefully explain the observed phase diagram and the unique Hund's coupling from a more fundamental level and potentially explain the origin of superconductivity.

Apart from potential improvement on theory, several future experiments will also be helpful to understand the superconductivity and magnetism.

One experiment is to control the strength of Coulomb interaction by gate screening. In presence of a gate, the itinerant electron will form dipoles with its image charged induced by the gate. The Coulomb interaction between electrons are actually dipole-

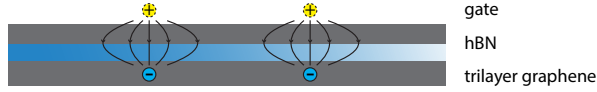


Figure 7.1: Schematic of gate screening. The itinerant electrons in RTG and their image charge generated by the gate form dipoles. The actual Coulomb interaction between electrons are actually dipole-dipole interactions.

dipole interactions. The potential energy of the two dipoles is

$$V(r) = -\frac{2p^2}{4\pi\epsilon_0 r^3} \quad (7.1)$$

where  $p = ed$  is the dipole moment and  $d$  is the distance between the electron and its image charge. By changing the thickness of the hBN layer between the RTG and the gate, we are effectively changing  $d$ , and therefore the interaction strength is modulated. When very thin (less than 5 nm) hBN layers are used, the Coulomb interaction will be effectively screened. This will set a higher bar for the Stoner criterion to be met and therefore enhance the superconductivity phase if it is phonon-mediated. However, if the superconductivity is a purely electronic effect. Effective screening of Coulomb interaction is likely to suppress the superconductivity phase. Therefore, this experiment will provide solid information of the origin of the superconductivity.

As an alternative approach, since the Coulomb interaction can be tuned by not only gate screening but also dielectric screening. By replacing the hBN layer with other materials, such as transition metal dichalcogenide or metal oxide, the effective interaction may also be modulated.

The second possible experiment is to generalize the investigation to a more general rhombohedral stacked multilayer system, such as ABCA-stacked four layer graphene. ABC-trilayer graphene and ABCA-stacked four layer graphene share similar band struc-

ture and density of states, although the trigonal warping effect is more significant in the latter case. On the one hand, a systematic investigation of the relation of magnetic ordering and low energy band structure may reveal how the local orbital magnetization in the  $\mathbf{k}$ -space will affect the magnetic ordering and induce phase transitions (such as the  $\alpha - \beta$ -phase transition discussed in Chapter 4. On the other hand, since superconductive phases tend to appear within a phase with annular Fermi surfaces, an enhanced trigonal warping effect may help to stabilize the superconductivity phase.

As a different system, the simplest chiral generalization of graphene, the bernal-stacked bilayer graphene[130], which has similar band structure but weaker trigonal warping effect, may also be worth investigating. Although bernal bilayer graphene has been widely studied both theoretically[131] and experimentally[132, 133], most of them were focusing on its transport properties under a strong magnetic field – the quantum Hall effect[98, 134, 135]. Low-field properties under large electrical displacement field, where magnetic phase transition and superconductivity may occur, is yet carefully investigated.

The third possible experiment is to build gate-defined lateral junctions. Since both ferromagnetism and superconductivity exist in RTG, and they can be simply induced by altering the gate voltages. If a complex gate structure is built so that the carrier density and displacement field of different parts of RTG can be independently tuned, a gate-defined ferromagnet/superconductor lateral junction can be built, which may be a potential platform to induce Majorana fermions.


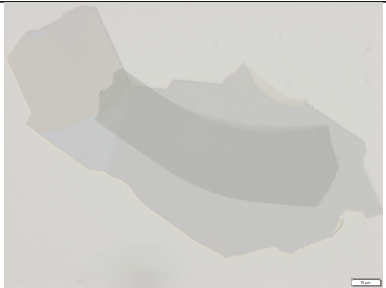
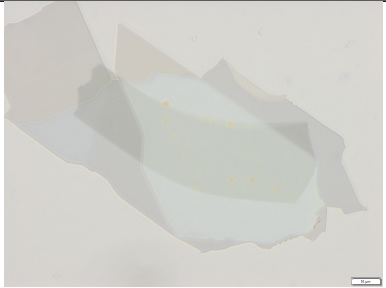
Finally, apart from gating, inducing spin-orbital coupling to the system by making RTG/transition metal dichalcogenide heterostructures[136] may also be interesting. Previous work[137] has shown that the superconductivity in twisted bilayer graphene can be enhanced by introducing spin-orbital coupling effect, a similar effect may also occur in RTG. More fundamentally, the expected observation will provide information whether the superconductivity in intrinsic RTG and that in graphene Moiré systems share the

same origin.


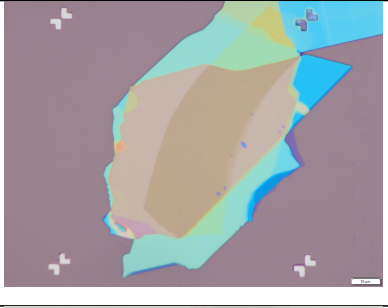
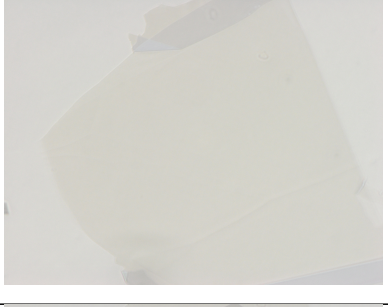


Besides conventional electrical transport measurement, other experimental probes such chemical potential measurement[138], SQUID on tip local probes[139] may reveal more information of the magnetic and superconducting ordering of rhombohedral trilayer graphene.

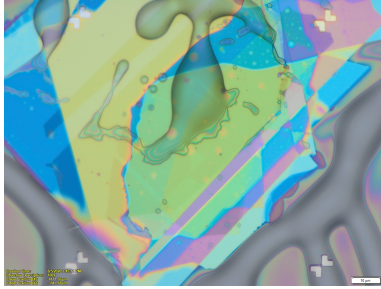
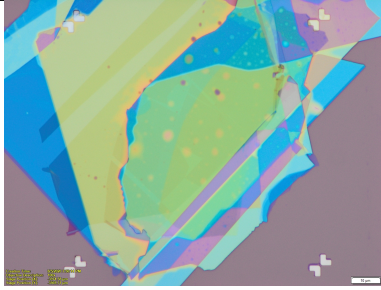
# Appendix A

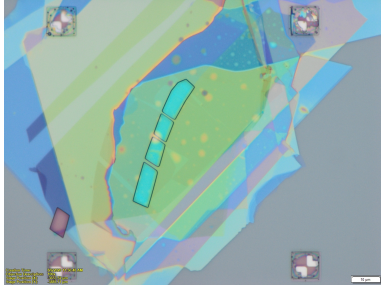
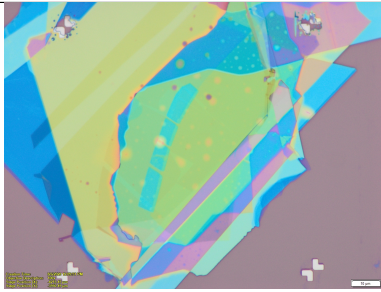
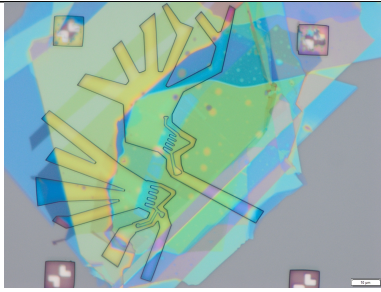
## Procedure of Sample Fabrication

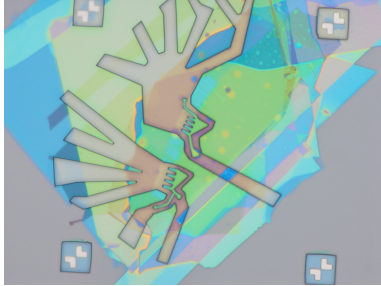
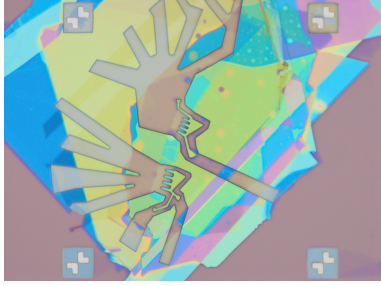
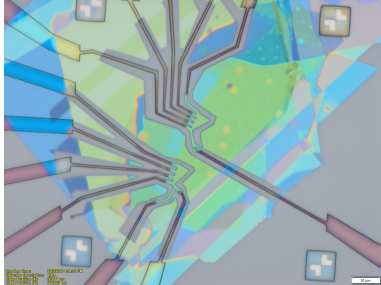
<p>Step1: Assemble the bottom part: pick up first hBN with PPC film at 40 °C</p>	
<p>Step2: Assemble the bottom part: pick up bottom gate at 45 °C</p>	
<p>Step3: Assemble the bottom part: pick up second hBN at 50 °C</p>	

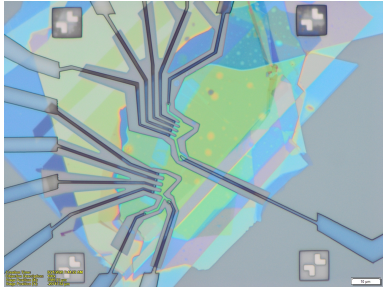
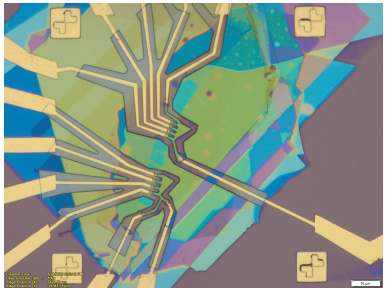
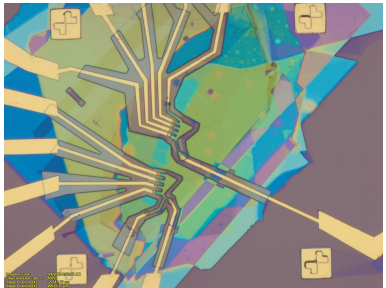


<p>Step4: Flip transfer: align the flipped PPC film to the substrate, engage at 40°C, then heat up to 150 °C to flatten the PPC film.</p>	
<p>Step5: Anneal the sample at 375 °C for two hours under vacuum (<math>&lt; 10^{-4}</math>Torr)</p>	
<p>Step 6: Assemble the top part: pickup first hBN with PPC film at 40 °C</p>	
<p>Step 7: Assemble the top part: pickup top gate at 45 °C</p>	
<p>Step 8: Assemble the top part: pickup second hBN at 50 °C</p>	

<p>Step 9: Assemble the top part: slowly pickup graphene trilayer at 40 °C. Do not move the pickup slide when finished</p>	<p>No picture saved</p>
<p>Step 10: Transfer the top part onto the bottom part: Align the two heterostructure at 40 °C. Increase the temperature by 0.5°C steps before the stack is fully deposited, then by 1.0°C steps until the sample reach 150 °C. Then slowly raise the pickup slide to detach it from the sample.</p>	 A false-color micrograph showing a complex, multi-layered heterostructure. The structure consists of several overlapping, irregularly shaped regions in various colors including blue, green, yellow, and purple. The background is a dark grey. The image shows the intricate details of the stacked layers and their alignment.
<p>Step 11: Rinse the sample in acetone for 1 min then in Isopropanol for 10 sec to remove PPC residue. Blow dry with a 15psi nitrogen gun.</p>	 A false-color micrograph showing the heterostructure after the cleaning process. The structure is similar to the one in the previous step, but the edges are sharper and the overall appearance is cleaner, with less background noise. The colors (blue, green, yellow, purple) are consistent with the previous image, indicating the same material layers are present.

<p>Step 12: Spincoat PMMA 950 A8 at 4000rpm for 60sec. Bake on a hotplate at 180 °C for 90 sec. Expose the etch windows with electron beam at a dose of <math>500\mu\text{C}/\text{cm}^{-2}</math> in an FEI Sirion SEM with NPGS module. Develop the sample in a cold (<math>&lt; 11^\circ\text{C}</math>) mixture of deionized water/isopropanol with the volume ratio of 3:1 for 60 sec. Etch the sample in <math>\text{XeF}_2</math> in a Xetch. (2 Torr in the expansion chamber, 5 cycles, with 20 sec etch time for each circle). Etch the sample with oxygen plasma in a Technics PEII Asher. (Pressure of oxygen: 300mTorr, RF power: 100W, etch time: 180 sec). The sample is then ready to be inspected with the Raman spectrometer.</p>	
<p>Step 13: Soak the sample in acetone for 5 min with the sample mounted vertically to remove PMMA and liftoff the fluorinated polymer residue on the top. Then rinse with isopropanol for 30 sec.</p>	
<p>Step 14: Repeat the spincoat lithography procedure in step 11 with an area dose of <math>300\mu\text{C}/\text{cm}^{-2}</math> to <math>350\mu\text{C}/\text{cm}^{-2}</math>. A smaller than usual dose is used so that the fine feature of the etch mask can be preserved.</p>	

<p>Step 15: Etch to form the device geometry. Etch is done in a Panasonic E640 inductively coupled plasma etcher. Recipe: <math>\text{CHF}_3</math> flow: 40 SCCM. <math>\text{O}_2</math> flow: 4 SCCM. Chamber pressure: 0.5 Pa. Chamber temperature: <math>95^\circ\text{C}</math>. RF source power: 100W. RF bias power: 100W. Etch is stopped when the conductive layer of the devices are completely isolated.</p>	 Scanning electron micrograph (SEM) showing the device structure after etching. The image displays a central region with several radiating, branched structures, likely electrodes or interconnects, surrounded by a smoother, less structured area. The etching process has clearly defined the conductive paths.
<p>Step 16: Repeat step 13 to strip off PMMA and liftoff off the fluorinated polymer coating. Squeezing acetone onto the sample with a squeeze bottom is sometimes necessary to effectively remove the residues.</p>	 Scanning electron micrograph (SEM) showing the device structure after liftoff. The image displays a central region with several radiating, branched structures, likely electrodes or interconnects, surrounded by a smoother, less structured area. The liftoff process has removed the polymer coating, leaving the conductive structures exposed.
<p>Step 17: Repeat step 11 to pattern the electrodes. Fine pattern parameters: spot size 1, <math>600\mu\text{C}/\text{cm}^{-2}</math>. Coarse pattern parameters: spot size 5, <math>500\mu\text{C}/\text{cm}^{-2}</math>. A larger than usual dose is used to improve the result of metal liftoff.</p>	 Scanning electron micrograph (SEM) showing the device structure after electrode patterning. The image displays a central region with several radiating, branched structures, likely electrodes or interconnects, surrounded by a smoother, less structured area. The electrode patterning process has refined the conductive paths.

<p>Step 18: Preparation etch of the metal/sample interface. Etch in step 15 usually generate a vertical profile, which is not ideal for making edge contact. Therefore, a second etch in a Panasonic E640 is applied. Recipe: <math>\text{CHF}_3</math> flow: 40 SCCM. <math>\text{O}_2</math> flow: 4 SCCM. Chamber pressure: 0.5 Pa. Chamber temperature: <math>95^\circ\text{C}</math>. RF source power: 200W. RF bias power: 30W. Etch is stopped when the conductive layers are exposed. This etch generates an edge profile with a slope.</p>	
<p>Step 19: Metal deposition. 3 nm chromium, 15 nm palladium and 150 nm gold is deposited in sequence right after the etch in step 18 in a CHA SEC-600-RAP electron-beam evaporator. A vacuum of <math>&lt; 2 \times 10^{-6}</math> Torr is reached before the deposition. Deposition rate: 1. Chromium: manual control, start from zero and ramp to 3 Å/sec in 5 sec. 2. Palladium: 1 Å/sec. 3. Gold: 2 Å/sec.</p>	
<p>Step 20: Etch to isolate layers that are in electrical contact. The step can be skipped if the heterostructure is properly designed. The etch is done with the same recipe in step 15 and is stopped when the necessary layers are etched through.</p>	

# Bibliography

- [1] E. C. Stoner, *Collective electron ferromagnetism*, Proceedings of the Royal Society of London. Series A. Mathematical and Physical Sciences **165** (Apr., 1938) 372–414. Publisher: Royal Society.
- [2] N. D. M. Ashcroft and N., Solid State Physics. Saunders, 1976.
- [3] L. P. Gor'kov, *Phonon mechanism in the most dilute superconductor n-type SrTiO<sub>3</sub>*, Proceedings of the National Academy of Sciences **113** (Apr., 2016) 4646–4651.
- [4] B. Tanatar and D. M. Ceperley, *Ground state of the two-dimensional electron gas*, Physical Review B **39** (Mar., 1989) 5005–5016. Publisher: American Physical Society.
- [5] V. M. Pudalov, A. Y. Kuntsevich, I. S. Burmistrov, and M. Reznikov, *Thermodynamic Studies of Two-Dimensional Correlated Electron Systems*, Journal of Low Temperature Physics **181** (Nov., 2015) 99–111.
- [6] M. S. Hossain, M. K. Ma, K. A. V. Rosales, Y. J. Chung, L. N. Pfeiffer, K. W. West, K. W. Baldwin, and M. Shayegan, *Observation of Spontaneous Ferromagnetism in a Two-Dimensional Electron System*, arXiv:2011.01335 [cond-mat] (Nov., 2020). arXiv: 2011.01335.
- [7] A. L. Sharpe, E. J. Fox, A. W. Barnard, J. Finney, K. Watanabe, T. Taniguchi, M. A. Kastner, and D. Goldhaber-Gordon, *Emergent ferromagnetism near three-quarters filling in twisted bilayer graphene*, Science **365** (Aug., 2019) 605–608.
- [8] G. Chen, A. L. Sharpe, E. J. Fox, Y.-H. Zhang, S. Wang, L. Jiang, B. Lyu, H. Li, K. Watanabe, T. Taniguchi, Z. Shi, T. Senthil, D. Goldhaber-Gordon, Y. Zhang, and F. Wang, *Tunable correlated Chern insulator and ferromagnetism in a moiré superlattice*, Nature **579** (Mar., 2020) 56–61. Number: 7797 Publisher: Nature Publishing Group.

- [9] K. S. Novoselov, A. K. Geim, S. V. Morozov, D. Jiang, Y. Zhang, S. V. Dubonos, I. V. Grigorieva, and A. A. Firsov, *Electric Field Effect in Atomically Thin Carbon Films*, Science **306** (2004), no. 5696 666–669.
- [10] T. Ando, A. B. Fowler, and F. Stern, *Electronic properties of two-dimensional systems*, Reviews of Modern Physics **54** (Apr., 1982) 437–672.
- [11] K. v. Klitzing and G. Ebert, *Application of the Quantum Hall Effect in Metrology*, Metrologia **21** (Jan., 1985) 11.
- [12] Y. Zhang, Y.-W. Tan, H. L. Stormer, and P. Kim, *Experimental observation of the quantum Hall effect and Berry’s phase in graphene*, Nature **438** (Nov., 2005) 201–204.
- [13] J. Eom, H. Cho, W. Kang, K. L. Campman, A. C. Gossard, M. Bichler, and W. Wegscheider, *Quantum Hall Ferromagnetism in a Two-Dimensional Electron System*, Science **289** (2000), no. 5488 2320–2323.
- [14] A. F. Young, A. F. Young, C. R. Dean, I. Meric, S. Sorgenfrei, H. Ren, K. Watanabe, T. Taniguchi, J. Hone, K. L. Shepard, and P. Kim, Quantum transport in graphene heterostructures. PhD thesis, Columbia University, 2012.
- [15] D. C. Tsui, H. L. Stormer, and A. C. Gossard, *Two-Dimensional Magnetotransport in the Extreme Quantum Limit*, Phys. Rev. Lett. **48** (May, 1982) 1559–1562.
- [16] K. I. Bolotin, F. Ghahari, M. D. Shulman, H. L. Stormer, and P. Kim, *Observation of the fractional quantum Hall effect in graphene*, Nature **462** (Nov., 2009) 196–199.
- [17] C. Nayak, S. H. Simon, A. Stern, M. Freedman, and S. Das Sarma, *Non-Abelian anyons and topological quantum computation*, Reviews of Modern Physics **80** (Oct., 2008) 1083–1159.
- [18] H. Schmidt, T. Lüdtkke, P. Barthold, and R. J. Haug, *Mobilities and scattering times in decoupled graphene monolayers*, Phys. Rev. B **81** (Mar, 2010) 121403.
- [19] G. Dobrik, L. Tapasztó, P. Nemes-Incze, P. Lambin, and L. P. Biró, *Crystallographically oriented high resolution lithography of graphene nanoribbons by stm lithography*, physica status solidi (b) **247** (2010), no. 4 896–902, [<https://onlinelibrary.wiley.com/doi/pdf/10.1002/pssb.200982953>].
- [20] R. Bistritzer and A. H. MacDonald, *Moiré butterflies in twisted bilayer graphene*, Phys. Rev. B **84** (July, 2011).



- [21] Y. Cao, V. Fatemi, A. Demir, S. Fang, S. L. Tomarken, J. Y. Luo, J. D. Sanchez-Yamagishi, K. Watanabe, T. Taniguchi, E. Kaxiras, R. C. Ashoori, and P. Jarillo-Herrero, *Correlated insulator behaviour at half-filling in magic-angle graphene superlattices*, Nature **556** (Apr., 2018) 80–84.
- [22] Y. Cao, D. Rodan-Legrain, O. Rubies-Bigorda, J. M. Park, K. Watanabe, T. Taniguchi, and P. Jarillo-Herrero, *Electric Field Tunable Correlated States and Magnetic Phase Transitions in Twisted Bilayer-Bilayer Graphene*, arXiv:1903.08596 [cond-mat] (Mar., 2019). arXiv: 1903.08596.
- [23] F. Zhang, B. Sahu, H. Min, and A. H. MacDonald, *Band structure of ABC-stacked graphene trilayers*, Physical Review B **82** (July, 2010) 035409. Publisher: American Physical Society.
- [24] G. I. Finch, H. Wilman, and W. A. Bone, *The diffraction of electrons by graphite*, Proceedings of the Royal Society of London. Series A - Mathematical and Physical Sciences **155** (1936), no. 885 345–365.
- [25] A. Taylor and D. Laidler, *Anomalous diffractions in the hull-debye-scherrer spectrum of graphite*, Nature **146** (1940), no. 3691 130–130.
- [26] H. S. Lipson, A. R. Stokes, and W. L. Bragg, *The structure of graphite*, Proceedings of the Royal Society of London. Series A. Mathematical and Physical Sciences **181** (1942), no. 984 101–105.
- [27] H. Jagodzinski, *The diffraction of x-rays by finite and imperfect crystals by a. j. c. wilson*, Acta Crystallographica **2** (1949), no. 5 340–340. <https://doi.org/10.1107/S0365110X49000886>.
- [28] R. R. Haering, *Band structure of rhombohedral graphite*, Canadian Journal of Physics **36** (1958), no. 3 352–362.
- [29] J. W. McClure, *Electron energy band structure and electronic properties of rhombohedral graphite*, Carbon **7** (1969), no. 4 425–432.
- [30] M. Koshino, *Interlayer screening effect in graphene multilayers with ABA and ABC stacking*, Physical Review B **81** (Mar., 2010) 125304.
- [31] M. Otani, M. Koshino, Y. Takagi, and S. Okada, *Intrinsic magnetic moment on (0001) surfaces of rhombohedral graphite*, Physical Review B **81** (2010), no. 16 161403. PRB.
- [32] B. Pamuk, J. Baima, F. Mauri, and M. Calandra, *Magnetic gap opening in rhombohedral-stacked multilayer graphene from first principles*, Physical Review B **95** (Feb., 2017) 075422.



- [33] F. Zhang, H. Min, M. Polini, and A. H. MacDonald, *Spontaneous inversion symmetry breaking in graphene bilayers*, Phys. Rev. B **81** (Jan., 2010).
- [34] D.-H. Xu, J. Yuan, Z.-J. Yao, Y. Zhou, J.-H. Gao, and F.-C. Zhang, *Stacking order, interaction, and weak surface magnetism in layered graphene sheets*, Physical Review B **86** (2012), no. 20 201404. PRB.
- [35] R. Xiao, F. Tasnádi, K. Koepf, J. W. F. Venderbos, M. Richter, and M. Taut, *Density functional investigation of rhombohedral stacks of graphene: Topological surface states, nonlinear dielectric response, and bulk limit*, Physical Review B **84** (2011), no. 16 165404. PRB.
- [36] N. B. Kopnin, T. T. Heikkilä, and G. E. Volovik, *High-temperature surface superconductivity in topological flat-band systems*, Physical Review B **83** (June, 2011) 220503. Publisher: American Physical Society.
- [37] W. A. Muñoz, L. Covaci, and F. M. Peeters, *Tight-binding description of intrinsic superconducting correlations in multilayer graphene*, Physical Review B **87** (2013), no. 13 134509. PRB.
- [38] J. Jung and A. H. MacDonald, *Gapped broken symmetry states in ABC-stacked trilayer graphene*, Physical Review B **88** (Aug., 2013) 075408. Publisher: American Physical Society.
- [39] R. Olsen, R. van Gelderen, and C. M. Smith, *Ferromagnetism in ABC-stacked trilayer graphene*, Physical Review B **87** (Mar., 2013) 115414. Publisher: American Physical Society.
- [40] T. Löthman and A. M. Black-Schaffer, *Universal phase diagrams with superconducting domes for electronic flat bands*, Physical Review B **96** (Aug., 2017) 064505. Publisher: American Physical Society.
- [41] C. H. Lui, Z. Li, Z. Chen, P. V. Klimov, L. E. Brus, and T. F. Heinz, *Imaging Stacking Order in Few-Layer Graphene*, Nano Letters **11** (Jan., 2011) 164–169.
- [42] C. Cong, T. Yu, K. Sato, J. Shang, R. Saito, G. F. Dresselhaus, and M. S. Dresselhaus, *Raman Characterization of ABA- and ABC-Stacked Trilayer Graphene*, ACS Nano **5** (Nov., 2011) 8760–8768.
- [43] T. A. Nguyen, J.-U. Lee, D. Yoon, and H. Cheong, *Excitation Energy Dependent Raman Signatures of ABA- and ABC-stacked Few-layer Graphene*, Scientific Reports **4** (Apr., 2014) 4630.
- [44] C. H. Lui, Z. Ye, C. Keiser, E. B. Barros, and R. He, *Stacking-dependent shear modes in trilayer graphene*, Applied Physics Letters **106** (2015), no. 4 041904.

- [45] N. Anderson, A. Hartschuh, and L. Novotny, *Near-field raman microscopy*, Materials Today **8** (2005), no. 5 50–54.
- [46] L. Ju, Z. Shi, N. Nair, Y. Lv, C. Jin, J. Velasco Jr, C. Ojeda-Aristizabal, H. A. Bechtel, M. C. Martin, A. Zettl, J. Analytis, and F. Wang, *Topological valley transport at bilayer graphene domain walls*, Nature **520** (Apr., 2015) 650–655.
- [47] Asylum, *Distinguishing aba- and abc-stacked trilayer graphene with atomic force microscopy*, 2021.
- [48] H. Zhao, Y.-C. Lin, C.-H. Yeh, H. Tian, Y.-C. Chen, D. Xie, Y. Yang, K. Suenaga, T.-L. Ren, and P.-W. Chiu, *Growth and raman spectra of single-crystal trilayer graphene with different stacking orientations*, ACS Nano **8** (2014), no. 10 10766–10773.
- [49] Y. Que, W. Xiao, H. Chen, D. Wang, S. Du, and H.-J. Gao, *Stacking-dependent electronic property of trilayer graphene epitaxially grown on ru(0001)*, Applied Physics Letters **107** (2015), no. 26 263101.
- [50] D. Pierucci, H. Sediri, M. Hajlaoui, J.-C. Girard, T. Brumme, M. Calandra, E. Velez-Fort, G. Patriarche, M. G. Silly, G. Ferro, V. Soulière, M. Marangolo, F. Sirotti, F. Mauri, and A. Ouerghi, *Evidence for flat bands near the fermi level in epitaxial rhombohedral multilayer graphene*, ACS Nano **9** (2015), no. 5 5432–5439.
- [51] Z. Gao, S. Wang, J. Berry, Q. Zhang, J. Gebhardt, W. M. Parkin, J. Avila, H. Yi, C. Chen, S. Hurtado-Parra, M. Drndić, A. M. Rappe, D. J. Srolovitz, J. M. Kikkawa, Z. Luo, M. C. Asensio, F. Wang, and A. T. C. Johnson, *Large-area epitaxial growth of curvature-stabilized abc trilayer graphene*, Nature Communications **11** (2020), no. 1 546.
- [52] C. F. P. Kastorp, D. A. Duncan, M. Scheffler, J. D. Thrower, A. L. Jørgensen, H. Hussain, T.-L. Lee, L. Hornekær, and R. Balog, *Growth and electronic properties of bi- and trilayer graphene on ir(111)*, Nanoscale **12** (2020), no. 38 19776–19786.
- [53] C. Bouhafs, S. Pezzini, F. R. Geisenhof, N. Mishra, V. Mišeikis, Y. Niu, C. Struzzi, R. T. Weitz, A. A. Zakharov, S. Forti, and C. Coletti, *Synthesis of large-area rhombohedral few-layer graphene by chemical vapor deposition on copper*, Carbon **177** (2021) 282–290.
- [54] A. Kumar, W. Escoffier, J. M. Poumirol, C. Faugeras, D. P. Arovas, M. M. Fogler, F. Guinea, S. Roche, M. Goiran, and B. Raquet, *Integer Quantum Hall Effect in Trilayer Graphene*, Physical Review Letters **107** (Sept., 2011) 126806.

- [55] C. H. Lui, Z. Li, K. F. Mak, E. Cappelluti, and T. F. Heinz, *Observation of an electrically tunable band gap in trilayer graphene*, Nature Physics **7** (Dec., 2011) 944–947.
- [56] L. Zhang, Y. Zhang, J. Camacho, M. Khodas, and I. Zaliznyak, *The experimental observation of quantum Hall effect of  $l=3$  chiral quasiparticles in trilayer graphene*, Nature Physics **7** (Dec., 2011) 953–957.
- [57] K. Zou, F. Zhang, C. Clapp, A. H. MacDonald, and J. Zhu, *Transport Studies of Dual-Gated ABC and ABA Trilayer Graphene: Band Gap Opening and Band Structure Tuning in Very Large Perpendicular Electric Fields*, Nano Letters **13** (Feb., 2013) 369–373.
- [58] Y. Lee, D. Tran, K. Myhro, J. Velasco, N. Gillgren, C. N. Lau, Y. Barlas, J. M. Poumirol, D. Smirnov, and F. Guinea, *Competition between spontaneous symmetry breaking and single-particle gaps in trilayer graphene*, Nature Communications **5** (Dec., 2014) 5656.
- [59] A. Kerelsky, C. Rubio-Verdú, L. Xian, D. M. Kennes, D. Halbertal, N. Finney, L. Song, S. Turkel, L. Wang, K. Watanabe, T. Taniguchi, J. Hone, C. Dean, D. N. Basov, A. Rubio, and A. N. Pasupathy, *Moiréless correlations in ABCA graphene*, Proceedings of the National Academy of Sciences **118** (Jan., 2021). Publisher: National Academy of Sciences Section: Physical Sciences.
- [60] Y. Henni, H. P. Ojeda Collado, K. Nogajewski, M. R. Molas, G. Usaj, C. A. Balseiro, M. Orlita, M. Potemski, and C. Faugeras, *Rhombohedral Multilayer Graphene: A Magneto-Raman Scattering Study*, Nano Letters **16** (June, 2016) 3710–3716.
- [61] Y. Lee, S. Che, J. Velasco Jr., D. Tran, J. Baima, F. Mauri, M. Calandra, M. Bockrath, and C. N. Lau, *Gate Tunable Magnetism and Giant Magnetoresistance in ABC-stacked Few-Layer Graphene*, arXiv:1911.04450 [cond-mat] (Nov., 2019). arXiv: 1911.04450.
- [62] Y. Shi, S. Xu, Y. Yang, S. Slizovskiy, S. V. Morozov, S.-K. Son, S. Ozdemir, C. Mullan, J. Barrier, J. Yin, A. I. Berdyugin, B. A. Piot, T. Taniguchi, K. Watanabe, V. I. Fal’ko, K. S. Novoselov, A. K. Geim, and A. Mishchenko, *Electronic phase separation in multilayer rhombohedral graphite*, Nature **584** (Aug., 2020) 210–214. Number: 7820 Publisher: Nature Publishing Group.
- [63] G. Chen, L. Jiang, S. Wu, B. Lyu, H. Li, B. L. Chittari, K. Watanabe, T. Taniguchi, Z. Shi, J. Jung, Y. Zhang, and F. Wang, *Evidence of a gate-tunable Mott insulator in a trilayer graphene moiré superlattice*, Nature Physics **15** (Mar., 2019) 237.

- [64] G. Chen, A. L. Sharpe, P. Gallagher, I. T. Rosen, E. J. Fox, L. Jiang, B. Lyu, H. Li, K. Watanabe, T. Taniguchi, J. Jung, Z. Shi, D. Goldhaber-Gordon, Y. Zhang, and F. Wang, *Signatures of tunable superconductivity in a trilayer graphene moiré superlattice*, Nature **572** (Aug., 2019) 215–219.
- [65] K. S. Novoselov, D. Jiang, F. Schedin, T. J. Booth, V. V. Khotkevich, S. V. Morozov, and A. K. Geim, *Two-dimensional atomic crystals*, Proceedings of the National Academy of Sciences of the United States of America **102** (July, 2005) 10451–10453.
- [66] A. H. C. Neto, F. Guinea, N. M. R. Peres, K. S. Novoselov, and A. K. Geim, *The electronic properties of graphene*, Reviews of Modern Physics **81** (2009), no. 1.
- [67] M. O. Goerbig, *Electronic properties of graphene in a strong magnetic field*, Reviews of Modern Physics **83** (Nov., 2011) 1193–1243.
- [68] T. O. Wehling, E. Şaşıoğlu, C. Friedrich, A. I. Lichtenstein, M. I. Katsnelson, and S. Blügel, *Strength of effective coulomb interactions in graphene and graphite*, Physical Review Letters **106** (2011), no. 23 236805.
- [69] R. Saito, G. Dresselhaus, and M. S. Dresselhaus, Physical Properties of Carbon Nanotubes. Imperial College Press, 1989.
- [70] A. A. Zibrov, P. Rao, C. Kometter, E. M. Spanton, J. I. A. Li, C. R. Dean, T. Taniguchi, K. Watanabe, M. Serbyn, and A. F. Young, *Emergent Dirac Gullies and Gully-Symmetry-Breaking Quantum Hall States in ABA Trilayer Graphene*, Physical Review Letters **121** (Oct., 2018) 167601.
- [71] S. Ono and K. Sugihara, *Trigonal warping of the bands and hall effect in graphite*, Journal of the Physical Society of Japan **24** (1968), no. 4 818–825.
- [72] M. Koshino and E. McCann, *Trigonal warping and Berry’s phase  $N\pi$  in ABC-stacked multilayer graphene*, Physical Review B **80** (Oct., 2009) 165409. Publisher: American Physical Society.
- [73] L. Van Hove, *The occurrence of singularities in the elastic frequency distribution of a crystal*, Physical Review **89** (1953), no. 6 1189–1193. PR.
- [74] J. Hubbard and B. H. Flowers, *Electron correlations in narrow energy bands*, Proceedings of the Royal Society of London. Series A. Mathematical and Physical Sciences **276** (1963), no. 1365 238–257.
- [75] W. Nolting, Fundamentals of Many-body Physics. Springer, 2009.
- [76] D. A. Abanin, I. Skachko, X. Du, E. Y. Andrei, and L. S. Levitov, *Fractional quantum Hall effect in suspended graphene: Transport coefficients and electron interaction strength*, Phys. Rev. B **81** (2010).

- [77] M. Kharitonov, *Phase diagram for the  $\nu=0$  quantum Hall state in monolayer graphene*, Physical Review B **85** (Apr., 2012) 155439. Publisher: American Physical Society.
- [78] J.-B. Wu, M.-L. Lin, X. Cong, H.-N. Liu, and P.-H. Tan, *Raman spectroscopy of graphene-based materials and its applications in related devices*, Chemical Society Reviews **47** (2018), no. 5 1822–1873.
- [79] A. J. M. Giesbers, U. Zeitler, S. Neubeck, F. Freitag, K. S. Novoselov, and J. C. Maan, *Nanolithography and manipulation of graphene using an atomic force microscope*, Solid State Communications **147** (2008), no. 9 366–369.
- [80] S. Masubuchi, M. Ono, K. Yoshida, K. Hirakawa, and T. Machida, *Fabrication of graphene nanoribbon by local anodic oxidation lithography using atomic force microscope*, Applied Physics Letters **94** (2009), no. 8.
- [81] S. Neubeck, F. Freitag, R. Yang, and K. S. Novoselov, *Scanning probe lithography on graphene*, Physica Status Solidi B-Basic Solid State Physics **247** (2010), no. 11-12 2904–2908.
- [82] K. Kumar, S. Strauf, and E. H. Yang, *A systematic study of graphite local oxidation lithography parameters using an atomic force microscope*, Nanoscience and Nanotechnology Letters **2** (2010), no. 2 185–188. Kumar, Kitu Strauf, Stefan Yang, E. H. Strauf, Stefan/H-1399-2016; Yang, Eui-Hyeok/B-5339-2012 Yang, Eui-Hyeok/0000-0003-4893-1691 Si.
- [83] L. P. Biro and P. Lambin, *Nanopatterning of graphene with crystallographic orientation control*, Carbon **48** (2010), no. 10 2677–2689. Biro, Laszlo P. Lambin, Philippe Biro, Laszlo P/A-3057-2010 Biro, Laszlo Peter/0000-0001-7261-0420; Lambin, Philippe/0000-0001-8051-042X 1873-3891.
- [84] H. Li, Z. Ying, B. Lyu, A. Deng, L. Wang, T. Taniguchi, K. Watanabe, and Z. Shi, *Electrode-Free Anodic Oxidation Nanolithography of Low-Dimensional Materials*, Nano Letters **18** (Dec., 2018) 8011–8015. Publisher: American Chemical Society.
- [85] A. K. Geim and I. V. Grigorieva, *Van der Waals heterostructures*, Nature **499** (2013), no. 7459 419–425.
- [86] C. R. Dean, A. F. Young, I. Meric, C. Lee, L. Wang, S. Sorgenfrei, K. Watanabe, T. Taniguchi, P. Kim, K. L. Shepard, and J. Hone, *Boron nitride substrates for high-quality graphene electronics*, Nature Nanotechnology **5** (2010) 722–726.
- [87] L. Wang, I. Meric, P. Y. Huang, Q. Gao, Y. Gao, H. Tran, T. Taniguchi, K. Watanabe, L. M. Campos, D. A. Muller, J. Guo, P. Kim, J. Hone, K. L.

- Shepard, and C. R. Dean, *One-Dimensional Electrical Contact to a Two-Dimensional Material*, Science **342** (Nov., 2013) 614–617.
- [88] H. Polshyn, H. Zhou, E. M. Spanton, T. Taniguchi, K. Watanabe, and A. F. Young, *Quantitative Transport Measurements of Fractional Quantum Hall Energy Gaps in Edgeless Graphene Devices*, Physical Review Letters **121** (Nov., 2018) 226801.
- [89] Y. Zeng, J. I. A. Li, S. A. Dietrich, O. M. Ghosh, K. Watanabe, T. Taniguchi, J. Hone, and C. R. Dean, *High-Quality Magnetotransport in Graphene Using the Edge-Free Corbino Geometry*, Physical Review Letters **122** (Apr., 2019) 137701.
- [90] Y. Yang, Y.-C. Zou, C. R. Woods, Y. Shi, J. Yin, S. Xu, S. Ozdemir, T. Taniguchi, K. Watanabe, A. K. Geim, K. S. Novoselov, S. J. Haigh, and A. Mishchenko, *Stacking order in graphite films controlled by van der waals technology*, Nano Letters **19** (2019), no. 12 8526–8532.
- [91] M. Serlin, C. L. Tschirhart, H. Polshyn, Y. Zhang, J. Zhu, K. Watanabe, T. Taniguchi, L. Balents, and A. F. Young, *Intrinsic quantized anomalous Hall effect in a moiré heterostructure*, Science **367** (Feb., 2020) 900–903. Publisher: American Association for the Advancement of Science Section: Report.
- [92] A. A. Zibrov, C. Kometter, H. Zhou, E. M. Spanton, T. Taniguchi, K. Watanabe, M. P. Zaletel, and A. F. Young, *Tunable interacting composite fermion phases in a half-filled bilayer-graphene Landau level*, Nature **549** (Sept., 2017) 360–364.
- [93] J. P. Eisenstein, L. N. Pfeiffer, and K. W. West, *Negative compressibility of interacting two-dimensional electron and quasiparticle gases*, Phys. Rev. Lett. **68** (Feb., 1992) 674–677.
- [94] A. Varlet, D. Bischoff, P. Simonet, K. Watanabe, T. Taniguchi, T. Ihn, K. Ensslin, M. Mucha-Kruczyński, and V. I. Fal’ko, *Anomalous Sequence of Quantum Hall Liquids Revealing a Tunable Lifshitz Transition in Bilayer Graphene*, Physical Review Letters **113** (Sept., 2014) 116602.
- [95] J. Alicea and M. P. Fisher, *Interplay between lattice-scale physics and the quantum Hall effect in graphene*, Solid State Communications **143** (Oct., 2007) 504–509.
- [96] D. Xiao, M.-C. Chang, and Q. Niu, *Berry phase effects on electronic properties*, Reviews of Modern Physics **2010** (July, 2010) 1959–2007.
- [97] C. Dean, P. Kim, J. I. A. Li, and A. Young, *Fractional Quantum Hall Effects in Graphene*, in Fractional Quantum Hall Effects: New Developments, pp. 317–375. World Scientific, Singapore, Jan., 2020.

- [98] P. Maher, C. R. Dean, A. F. Young, T. Taniguchi, K. Watanabe, K. L. Shepard, J. Hone, and P. Kim, *Evidence for a spin phase transition at charge neutrality in bilayer graphene*, Nature Physics **9** (2013), no. 3 154–158.
- [99] A. F. Young, J. D. Sanchez-Yamagishi, B. Hunt, S. H. Choi, K. Watanabe, T. Taniguchi, R. C. Ashoori, and P. Jarillo-Herrero, *Tunable symmetry breaking and helical edge transport in a graphene quantum spin Hall state*, Nature **505** (Jan., 2014) 528–532.
- [100] L. N. Cooper, *Bound Electron Pairs in a Degenerate Fermi Gas*, Physical Review **104** (Nov., 1956) 1189–1190.
- [101] J. Bardeen, L. N. Cooper, and J. R. Schrieffer, *Theory of Superconductivity*, Physical Review **108** (Dec., 1957) 1175–1204.
- [102] N. D. Mathur, F. M. Grosche, S. R. Julian, I. R. Walker, D. M. Freye, R. K. W. Haselwimmer, and G. G. Lonzarich, *Magnetically mediated superconductivity in heavy fermion compounds*, Nature **394** (July, 1998) 39–43. Number: 6688  
Publisher: Nature Publishing Group.
- [103] D. J. Scalapino, *A common thread: The pairing interaction for unconventional superconductors*, Reviews of Modern Physics **84** (Oct., 2012) 1383–1417.  
Publisher: American Physical Society.
- [104] H. Zhou, T. Xie, A. Ghazaryan, T. Holder, J. R. Ehrets, E. M. Spanton, T. Taniguchi, K. Watanabe, E. Berg, M. Serbyn, and A. F. Young, *Half and quarter metals in rhombohedral trilayer graphene*, [arXiv:2104.00653 \[cond-mat\]](https://arxiv.org/abs/2104.00653) (Apr., 2021). arXiv: 2104.00653.
- [105] E. V. Castro, N. M. R. Peres, T. Stauber, and N. A. P. Silva, *Low-Density Ferromagnetism in Biased Bilayer Graphene*, Physical Review Letters **100** (May, 2008) 186803.
- [106] V. L. Berezinskii, *Destruction of long-range order in on-dimensional and two-dimensional systems having a continuous symmetry group I: classical systems*, Soviet Physics JETP **32** (1970), no. 3 493.
- [107] J. M. Kosterlitz and D. J. Thouless, *Ordering, metastability and phase transitions in two-dimensional systems*, Journal of Physics C: Solid State Physics **6** (Apr., 1973) 1181–1203. Publisher: IOP Publishing.
- [108] P. W. Anderson, *Theory of dirty superconductors*, Journal of Physics and Chemistry of Solids **11** (Sept., 1959) 26–30.
- [109] A. A. Abrikosov and L. P. Gor'kov, *Contribution to the theory of superconducting alloys with paramagnetic impurities*, Zhur. Eksptl'. i Teoret. Fiz. **Vol: 39** (Dec., 1960). Institution: Inst. of Problems in Physics, Academy of Sciences, USSR.

- [110] M. Tinkham, Introduction to Superconductivity. McGraw-Hill, New York, 2nd ed., 1975.
- [111] T. Taychatanapat, K. Watanabe, T. Taniguchi, and P. Jarillo-Herrero, *Electrically tunable transverse magnetic focusing in graphene*, Nature Physics **9** (Apr., 2013) 225–229.
- [112] M. Lee, J. R. Wallbank, P. Gallagher, K. Watanabe, T. Taniguchi, V. I. Fal’ko, and D. Goldhaber-Gordon, *Ballistic miniband conduction in a graphene superlattice*, Science **353** (Sept., 2016) 1526–1529.
- [113] A. M. Clogston, *Upper Limit for the Critical Field in Hard Superconductors*, Physical Review Letters **9** (Sept., 1962) 266–267. Publisher: American Physical Society.
- [114] B. S. Chandrasekhar, *A note on the maximum critical field of high-field superconductors*, Applied Physics Letters **1** (Sept., 1962) 7–8. Publisher: American Institute of Physics.
- [115] J. Y. Lee, E. Khalaf, S. Liu, X. Liu, Z. Hao, P. Kim, and A. Vishwanath, *Theory of correlated insulating behaviour and spin-triplet superconductivity in twisted double bilayer graphene*, Nature Communications **10** (Nov., 2019) 5333. Number: 1 Publisher: Nature Publishing Group.
- [116] E. Cornfeld, M. S. Rudner, and E. Berg, *Spin-polarized superconductivity: order parameter topology, current dissipation, and multiple-period Josephson effect*, Physical Review Research **3** (Jan., 2021) 013051. arXiv: 2006.10073.
- [117] R. Ojajärvi, T. Hyart, M. A. Silaev, and T. T. Heikkilä, *Competition of electron-phonon mediated superconductivity and Stoner magnetism on a flat band*, Physical Review B **98** (Aug., 2018) 054515. Publisher: American Physical Society.
- [118] N. B. Kopnin, M. Ijäs, A. Harju, and T. T. Heikkilä, *High-temperature surface superconductivity in rhombohedral graphite*, Phys. Rev. B **87** (Apr, 2013) 140503.
- [119] W. L. McMillan, *Transition Temperature of Strong-Coupled Superconductors*, Physical Review **167** (Mar., 1968) 331–344.
- [120] P. B. Allen, *Electron-Phonon Coupling Constants*, in Handbook of Superconductivity (C. P. P. Jr., ed.), pp. 478–489. Academic Press, San Diego, 2000.
- [121] W. Kohn and J. M. Luttinger, *New Mechanism for Superconductivity*, Physical Review Letters **15** (Sept., 1965) 524–526. Publisher: American Physical Society.



- [122] A. V. Chubukov and S. A. Kivelson, *Superconductivity in engineered two-dimensional electron gases*, Physical Review B **96** (Nov., 2017) 174514. Publisher: American Physical Society.
- [123] Y. Cao, V. Fatemi, S. Fang, K. Watanabe, T. Taniguchi, E. Kaxiras, and P. Jarillo-Herrero, *Unconventional superconductivity in magic-angle graphene superlattices*, Nature **556** (Apr., 2018) 43–50.
- [124] J. M. Park, Y. Cao, K. Watanabe, T. Taniguchi, and P. Jarillo-Herrero, *Tunable strongly coupled superconductivity in magic-angle twisted trilayer graphene*, Nature **590** (Feb., 2021) 249–255. Number: 7845 Publisher: Nature Publishing Group.
- [125] Z. Hao, A. M. Zimmerman, P. Ledwith, E. Khalaf, D. H. Najafabadi, K. Watanabe, T. Taniguchi, A. Vishwanath, and P. Kim, *Electric field-tunable superconductivity in alternating-twist magic-angle trilayer graphene*, Science **371** (Mar., 2021) 1133–1138. Publisher: American Association for the Advancement of Science Section: Report.
- [126] H. Polshyn, J. Zhu, M. A. Kumar, Y. Zhang, F. Yang, C. L. Tschirhart, M. Serlin, K. Watanabe, T. Taniguchi, A. H. MacDonald, and A. F. Young, *Electrical switching of magnetic order in an orbital Chern insulator*, Nature **588** (Dec., 2020) 66–70.
- [127] Y.-H. Zhang, D. Mao, Y. Cao, P. Jarillo-Herrero, and T. Senthil, *Nearly flat Chern bands in moiré superlattices*, Physical Review B **99** (Feb., 2019) 075127.
- [128] E. C. Regan, D. Wang, C. Jin, M. I. Bakti Utama, B. Gao, X. Wei, S. Zhao, W. Zhao, Z. Zhang, K. Yumigeta, M. Blei, J. D. Carlström, K. Watanabe, T. Taniguchi, S. Tongay, M. Crommie, A. Zettl, and F. Wang, *Mott and generalized Wigner crystal states in  $WSe_2/WSe_2$  moiré superlattices*, Nature **579** (Mar., 2020) 359–363. Number: 7799 Publisher: Nature Publishing Group.
- [129] Y. Xu, S. Liu, D. A. Rhodes, K. Watanabe, T. Taniguchi, J. Hone, V. Elser, K. F. Mak, and J. Shan, *Correlated insulating states at fractional fillings of moiré superlattices*, Nature **587** (Nov., 2020) 214–218. Number: 7833 Publisher: Nature Publishing Group.
- [130] E. McCann and M. Koshino, *The electronic properties of bilayer graphene*, Reports on Progress in Physics **76** (2013), no. 5 056503.
- [131] J. Jung and A. H. MacDonald, *Accurate tight-binding models for the pi bands of bilayer graphene*, Physical Review B **89** (Jan., 2014) 035405.
- [132] T. Ohta, A. Bostwick, T. Seyller, K. Horn, and E. Rotenberg, *Controlling the Electronic Structure of Bilayer Graphene*, Science **313** (Aug., 2006) 951–954.

- [133] E. V. Castro, K. S. Novoselov, S. V. Morozov, N. M. R. Peres, J. M. B. L. dos Santos, J. Nilsson, F. Guinea, A. K. Geim, and A. H. C. Neto, *Biased Bilayer Graphene: Semiconductor with a Gap Tunable by the Electric Field Effect*, Phys. Rev. Lett. **99** (Nov., 2007).
- [134] A. A. Zibrov, E. M. Spanton, H. Zhou, C. Kometter, T. Taniguchi, K. Watanabe, and A. F. Young, *Even-denominator fractional quantum Hall states at an isospin transition in monolayer graphene*, Nature Physics **14** (Sept., 2018) 930–935.
- [135] J. I. A. Li, C. Tan, S. Chen, Y. Zeng, T. Taniguchi, K. Watanabe, J. Hone, and C. R. Dean, *Even denominator fractional quantum Hall states in bilayer graphene*, Science (Oct., 2017) eaao2521.
- [136] J. O. Island, X. Cui, C. Lewandowski, J. Y. Khoo, E. M. Spanton, H. Zhou, D. Rhodes, J. C. Hone, T. Taniguchi, K. Watanabe, L. S. Levitov, M. P. Zaletel, and A. F. Young, *Spin-orbit-driven band inversion in bilayer graphene by the van der Waals proximity effect*, Nature **571** (July, 2019) 85–89.
- [137] H. S. Arora, R. Polski, Y. Zhang, A. Thomson, Y. Choi, H. Kim, Z. Lin, I. Z. Wilson, X. Xu, J.-H. Chu, K. Watanabe, T. Taniguchi, J. Alicea, and S. Nadj-Perge, *Superconductivity in metallic twisted bilayer graphene stabilized by  $WSe_2$* , Nature **583** (July, 2020) 379–384. Number: 7816 Publisher: Nature Publishing Group.
- [138] F. Yang, A. A. Zibrov, R. Bai, T. Taniguchi, K. Watanabe, M. P. Zaletel, and A. F. Young, *Experimental Determination of the Energy per Particle in Partially Filled Landau Levels*, Physical Review Letters **126** (Apr., 2021) 156802. Publisher: American Physical Society.
- [139] A. Uri, *Fabrication and characterization of multi-junction, multi-terminal superconducting quantum interference device on a tip*, Master’s thesis, WEIZMANN Institute of Science, Rehovot, Israel, Feb., 2015.